New insights into turbidity current structure and behaviour from direct measurements in the deep-sea

NATASHA CHAPPLOW

New insights into turbidity current structure and behaviour from direct measurements in the deep-sea

Natasha Chapplow

This thesis is submitted in partial fulfilment of the requirements for the degree of Doctor of Philosophy

Earth Sciences Department
Durham University

February 2022

ABSTRACT

UNIVERSITY OF DURHAM
DEPARTMENT OF EARTH SCIENCES

Doctor of Philosophy

New insights into turbidity current structure and behaviour from direct measurements in the deep-sea

By Natasha Chapplow

Submarine canyons are important conduits for transporting sediment, organic carbon, nutrients, and pollutants to the deep sea. Oceanic sediment density flows called turbidity currents are the main mechanism responsible for redistributing this material on a global scale. Turbidity currents can be very powerful, and carry exceptionally large sediment volumes at high speeds (<19 m/s). Consequently, turbidity currents damage seabed telecommunications cables that carry > 95% of global data traffic, as well as oil and gas pipelines and other infrastructure for energy transport. Thus, it is crucial to understand how turbidity currents evolve over time and space. Yet, knowledge of how these seafloor flows behave is mostly derived from indirect studies, as the powerful nature of turbidity currents ensures that only a handful of direct measurements exist.

This thesis presents unusually high resolution (sub-minute) direct monitoring datasets for turbidity currents, from two submarine canyons in different locations. The first location is Monterey Canyon, offshore California, where turbidity current evolution is analysed through observations of flow behaviour and mixing processes. In particular, turbidity currents are shown to reverse in buoyancy (termed lofting), and rise vertically from the seafloor, after sufficient sediment had been deposited. The water column then took < 2 days to recover to pre-event conditions. These first deep-sea observations of lofting have important implications for the structure of deposits that can form valuable hydrocarbon reserves. Additionally, the amount of sediment and seawater entrained into turbidity currents is quantified at multiple locations along Monterey Canyon. It is shown that turbidity currents at this site grew in water volume by up to a factor of four, which is significantly smaller than predicted by previous numerical and lab-based models, and this discrepancy has important implications for improving seafloor hazard mitigation strategies. The second field dataset comes from the Congo Canyon off West Africa, and it is used to document how the front structure of turbidity currents evolves. At this site, turbidity currents travelling along the same flow path developed one of two different flow-front shapes. Faster turbidity currents developed a distinct head, while slower flows did not. For the first time, it is demonstrated that a thin lens of seawater can be pushed in front of faster flows, similar to air blasts observed during snow avalanches. Overall, this thesis delivers unique insight into how turbidity flows develop over time and space. Such analysis is timely, given that the spatial extent of seafloor infrastructure is predicted to increase by between 50-70% by 2028.

CONTENTS

DECLARATION OF AUTHORSHIP

I, Natasha Chapplow, declare that the thesis entitled “New insights into turbidity current structure and behaviour from direct measurements in the deep-sea” and the work presented in the thesis are both my own, and have been generated by me as the result of my own original research. I confirm that:

- This work was done wholly or mainly while in candidature for a research degree at Durham University;
- Where any part of this thesis has previously been submitted for a degree or any other qualification at this University or any other institution, this has been clearly stated;
- Where I have consulted the published work of others, this is always clearly attributed;
- Where I have quoted from the work of others, the source is always given. With the exception of such quotations, this thesis is entirely my own work;
- I have acknowledged all main sources of help;
- Where the thesis is based on work done by myself jointly with others, I have made clear exactly what was done by others and what I have contributed myself;

Signed: .....

Date:.....

ACKNOWLEDGEMENTS

First and foremost, I would like to express my deep gratitude to the funding bodies NERC IAPETUS and Exxon Mobil. The support of these bodies not only enabled this research project to take place, but also allowed for many opportunities that greatly enriched my experience throughout.

I would also like to highlight the truly outstanding people that have supported, inspired, and taught me unforgettably meaningful lessons during my PhD. This project has been a one-of-a-kind opportunity that was made possible by the expert supervision of Pete Talling, who is a master of juggling many responsibilities, big picture thinking, and explaining complex ideas with ease. These qualities alone are enough to make a great supervisor. But the time I have spent with Pete has also been filled with empathy, topical humour, generosity, and his love of travel, biscuits, and caving (which is fascinating to hear about!). When trying to work into these acknowledgements that Pete is understatedly cool and adventure is simply his default setting, I googled Pete Talling Caving and discovered that one of the top results is the 'Gates of Hell' (a caving expedition he co-led). Not many people can say that they know someone who in their spare time has explored the Gates of Hell, thanks also for making my PhD the opposite of a hellish experience. Instead, by setting challenging expectations that were balanced with re-assurance, Pete has contributed to half a decade of my life that I am incredibly proud of. Thank you also for being equally supportive of my personal commitments and goals beyond my PhD, it means far more than I could ever convey on this page.

Matthieu Cartigny has also provided superb co-supervision. I am incredibly grateful for the time and effort he has brought to this project. One of my first impressions was his humble, intelligent, and light-hearted approach to science, which is refreshing. A social butterfly by nature, even the pandemic could not bring him down, full of life and positivity even when our meetings were over zoom. Highlights include his comedic commentary on my vaccinating shifts, patience with my terrible screen sharing ability on Teams, and cheerful attitude in the face of MATLAB error messages!

A very special mention and thanks to everyone who made it possible for me to experience science the MBARI way, which is world-class. It has been a real honour to learn from Charlie Paull, who has so generously shared straightforward advice, and always made time to provide

useful and detailed feedback on my work. I have also enjoyed discovering that he has a great self-deprecating sense of humour and admire his personable and well-spoken demeanour. Sincere thanks also to Roberto, who has been a highly supportive collaborator and who I now consider a friend. I have thoroughly enjoyed sharing positive and insightful conversations about science and life. My visits would also not have been possible without Eve and Krystle, both of whom have dispositions sunnier than California itself. I could not have asked for better sherpas during my time at MBARI.

There are also numerous other collaborators who have shared their encouragement and feedback on my work over the years, and I would like to express my sincere gratitude to all of you: Mike Clare, Dan Parsons, Jim Barry, David Hoyal, Juan Fedele, Katie Maier, Mary McGann, and Kurt Rosenberger. Additionally, to those that I have not already mentioned at Durham University, but are also integral to team turbidity: Ed, Meg, Sean, and Gustavo. I wish you all the best in your futures. My PhD examiners Nic De Paola and Neil Mitchell for reviewing this work, providing insightful comments, and their kind and engaged demeanours during my viva.

Outside of academia, there are numerous people to whom I am indebted for their instrumental support during my PhD. Marina and Erik for their kindness and hospitality that was above and beyond what I could have hoped for during my time in California. Renee for keeping me young with her outstanding friendship that is always only a phone call away. Shauna for reading every page of this thesis. My parents also for their enthusiasm and support, which has grown substantially since their initial reaction of “That’s a long time before you’ll graduate”. In fact the time flew by, and it is especially thanks to every person mentioned here.

Chapter 1: Thesis Introduction

1.1. Rationale

Turbidity currents are a type of gravity flow that travel along the seafloor, due to a density excess that is generated by their suspended sediment load. In comparison to terrestrial gravity flows (i.e. debris flows, avalanches and pyroclastic flows), turbidity currents can be many orders of magnitude larger in scale (Middleton, 1993). These flows can run-out for up to hundreds or even thousands of kilometres, from the continental shelf to the deep sea (Pirmez and Imran, 2003; Babonneau et al., 2010). Over their course, turbidity currents shape submarine canyons (Kuenen, 1937), and transport globally significant volumes of sediment to form some of the largest accumulations on the planet (Bouma et al., 2012). Additionally, these flows carry nutrients, heat, fresher water, organic carbon and pollutants to the deep ocean over much shorter timescales than general ocean circulation (Kao et al., 2010). Turbidity currents can therefore impact geochemical cycles and deep-sea ecosystems. Additionally, their deposits can form valuable hydrocarbon reserves, over geological time (Wiemer and Link, 1991; Mulder and Alexander, 2001). The relatively fast speeds of turbidity currents are well documented (Khripounoff et al., 2003; Xu et al., 2010; Talling et al., 2013; Paull et al., 2018; Clare et al., 2020), and sometimes reach speeds of up to 19 m/s (Heezen and Ewing, 1952; Piper and Aksu, 1987). Consequently, these flow events can severely damage seafloor infrastructure, in particular, energy pipelines and telecommunications cables that carry >95% of global data traffic (Carter et al., 2014; Clare et al., 2018). Quantitative descriptions of turbidity current behaviour are needed for seafloor geohazard assessments, to further protect vulnerable seafloor infrastructures. Yet few direct measurements of turbidity currents exist, as their often violent nature leads to equipment loss and/or damage, preventing the success of fieldwork campaigns. Consequently, existing understanding of turbidity currents is predominantly based upon indirect studies, including laboratory experiments and numerical models. However, scaling issues and simplifying assumptions limit the confidence that can be placed in these types of indirect approaches (Middleton, 1966), and they may not capture all aspects of full scale submarine flows. It is therefore crucial that long-standing models are tested, and that numerical models are calibrated against realistic benchmarks. Field observations represent one of the best opportunities to improve both of these aspects, and with

recent advances in technology, a handful of high-resolution data now exists (Xu, 2011; Khripounoff et al., 2012; Fildani et al., 2017; Clare et al., 2020).

1.2. Overarching Aims and Thesis Outline

The overall aim of this thesis is to use direct field measurements of turbidity currents to better understand how these flows behave and evolve over time, and to test (where possible) existing models for their behaviour and evolution. Direct field observations were acquired at multiple mooring stations during two different field projects: one field campaign in Monterey Canyon offshore California, and another project in the Congo Canyon off West Africa. The moorings housed various sensors, and all stations typically included acoustic Doppler current profilers (ADCPs) that measured time series of velocity profiles and acoustic backscatter. The first data set comes from Monterey Canyon, where 7 ADCP-moorings recorded turbidity currents as they ran out for up to 50 km, during an 18-month period from October 2015 to April 2017 (Paull et al., 2018). The second field data set comes from the Congo Canyon, where 11 moorings measured turbidity currents for the first time at water depths >2 km, from September 2019 to January 2020 (Talling et al., 2021). Collectively, these field projects have acquired the only detailed measurements from turbidity currents in the deep (> 500 m) ocean, at multiple sites along their pathway. Thus, new insights into turbidity current behaviour are made possible by these datasets.

The backbone of this thesis is formed by unique field data from Monterey Canyon and Congo Canyon, which are presented as three thesis chapters, each involving data analysis. In addition, an introductory thesis chapter, and a final chapter that brings together the overall conclusions from the whole thesis. The content of this thesis is subdivided into the following chapters (below), and a brief summary is given for each one.

Chapter 1: Introduction to the thesis and data-types.
Chapter 2: Do turbidity currents loft, and how can they affect ocean stratification?
Chapter 3: How much mixing do turbidity currents experience over time?
Chapter 4: Can turbidity currents form different frontal structures?
Chapter 5: Conclusions.

Chapter 1: Introduction to the thesis

The opening chapter outlines the nature of turbidity currents and their importance. A brief historical review of turbidity current research is also given, to highlight why direct measurements of these flows are sought after. Some of the key technologies that have enabled direct measurements are then explained. Finally, field experiments relevant to this thesis are presented, and a justification for why these particular datasets were chosen, is briefly discussed.

Chapter 2: What affect(s) do turbidity currents have on ocean stratification?

Turbidity currents are comprised of mixtures of sediment and seawater that have been transported from shallower water depths. Typically, turbidity currents are denser than the surrounding seawater due to the excess density of the sediment they carry, which causes the flow to travel along the seabed. However, it has been proposed that once enough sediment has settled from a turbidity current, less dense interstitial seawater carried from upslope can overcome the excess density of remaining sediment. These lighter parts of the flow can then reverse their buoyancy to rise vertically from the turbidity current in a process termed lofting. Besides turbidity currents, other types of terrestrial particle laden density flows also loft. In particular, the upper dilute parts (co-ignimbrite cloud) of pyroclastic flows from volcanic eruptions have been observed or inferred to loft (Sparks et al., 1986; Sparks, 1997; Calder et al., 1997). Previous studies of turbidity current lofting are based almost entirely on laboratory experiments and theory (Hurzeler et al., 1996; Sparks et al., 1993; Gladstone and Pritchard, 2010). However, to date there are no direct field observations of lofting in turbidity currents. Chapter 2 presents field data from Monterey Canyon, and includes the first detailed observations of lofting in deep-sea turbidity currents. Two individual flow events passed through three distal moorings, which collected time series measurements of flow velocity, temperature, salinity, and turbidity (a proxy for sediment concentration). Overall, Chapter 2 compares the behaviour of these two turbidity current events, which were both relatively fast moving (> 4 m/s). However, only one flow showed distinct evidence of lofting, and the possible reasons for this are then discussed. In the aftermath of these two turbidity currents, the water column took up to two days to return to normal conditions.

Chapter 3: How much mixing do turbidity currents experience over time?

It has been proposed that mixing processes with surrounding seawater are a strong control on turbidity current evolution and behaviour (Turner and Benton, 1974; Ellison and Turner, 1959; Parker et al., 1986). Laboratory and theoretical models have sought to understand what controls the amount of mixing into a turbidity current, including the depth-averaged bulk Richardson number (Ellison and Turner, 1959; Parker et al., 1987; Bolla Pittaluga et al., 2018). However, models based on such depth-averaged parameters may oversimplify flow dynamics, leading to inaccurate results (Traer et al., 2015). Chapter 3 presents the first detailed measurements of mixing within turbidity currents, based on observed changes in water temperature and salinity within flows in Monterey Canyon. The data presented in Chapter 3 shows that two powerful turbidity currents increased in volume as they travelled through three successive mooring sites; which were distributed over a distance of ~44 km. Temperature data indicate that the bottom layer within the turbidity current is shielded from mixing. Field observations of mixing rates are compared to two previous mixing models. The Parker et al. (1987) model significantly over-predicts the entrainment at all mooring sites; while a similar model that includes a detrainment term (Bolla Pittaluga et al., 2018) strongly under-estimates the flow volume. These conclusions are an important first step towards understanding both how turbidity currents mix with surrounding water, and how to quantify and predict such mixing. In turn, this can lead to more accurate predictions of turbidity current dynamics, improved seafloor hazard assessments, and better understanding of deposit geometries.

Chapter 4: Can turbidity currents form different frontal structures?

The frontal region of a turbidity current may play a key role in driving flows (Azpiroz-Zabala et al., 2017), and/or be a critical feature in influencing how flows mix with surrounding seawater (Allen, 1971; Simpson, 1997; Sher and Woods, 2017). However, the fast and dense nature of turbidity flow fronts ensures that few direct measurements exist, thus this structure remains poorly understood. Chapter 4 provides the first detailed analysis of field observations from the frontal parts of turbidity currents, which occurred in the Congo Canyon in 2019-20. This work shows that turbidity currents may develop one of two different types of front, which are linked to faster or slower front speeds. It is shown that faster and denser flows tend to develop a distinctly thicker head and thinner neck, and both of these are lacking in slower flows.

Additionally, billow structures can form behind the heads of fast flows, due to shearing between the upper flow and the overlying ambient fluid. These billows can modify the structure

of the flow behind the head. Moreover, for the first time, Chapter 4 shows that powerful turbidity flows can push a small amount of sediment-free seawater ahead of a turbidity current; similar to air blast-waves that travel ahead of snow and rock avalanches.

Chapter 5: Conclusions

The main findings from each scientific chapter are summarised, and common themes across these chapters are discussed. Key future research directions for this field are then briefly discussed, by exploring some of the fundamental scientific questions that remain unanswered. Finally, possible strategies to further progress towards solving these crucial questions are outlined.

1.3. Research driver: The need to directly measure turbidity currents, and to find new insights from the first detailed direct measurements from turbidity currents in the deep-sea

There are very few direct measurements of turbidity currents, which is a stark contrast to other major sediment transport processes. This lack of direct turbidity current measurements is mainly due to: their occurrence in the deep-sea, their episodic occurrence, and perhaps most importantly their notorious ability to damage sensors placed in their path. However, recent advances in technology have enabled a handful of direct monitoring studies to successfully capture turbidity currents, in some cases at multiple points along their pathway (Kao et al., 2010; Paull et al., 2018; Talling et al., 2021). Yet, direct observations are still relatively rare, and much of our understanding comes from indirect studies. The following section provides a brief historical review of such insights.

1.3.1. The turbidite revolution

The initial realisation that turbidity currents occurred in the oceans came from their deposits, which are called turbidites (e.g. Kuenen and Migliorini, 1950) (Figure 1.1). Turbidites are characterised by sedimentary sequences that often (but not always) grade vertically from coarser to finer sediment (i.e. normal grading; Figure 1.1; Bouma, 1962). Normal grading is often inferred from a depositional and temporally or spatially decelerating flow (Kneller and

Kneller and Branney, 1995; Mulder et al., 1998; Kneller and McCaffrey, 2003; Amy et al., 2005). Conversely, fine to coarsening sequences (inverse grading) occur when flows accelerate (Mulder et al., 1998; Mulder et al., 2001). More recently, studies have used sediment core data to infer flow dynamics. As one example, it was inferred that flows that were much thinner than originally thought are capable of running-out over long distances (Stevenson et al., 2014). But caution is required when interpreting deposits, as complex hydrodynamic processes are not fully captured by the rock record, and multiple types of dense or dilute flow can lead to the same deposit (Talling et al., 2012). Despite these limitations, turbidites remain the most commonly used evidence for reconstructing flow behaviour, at sites worldwide.

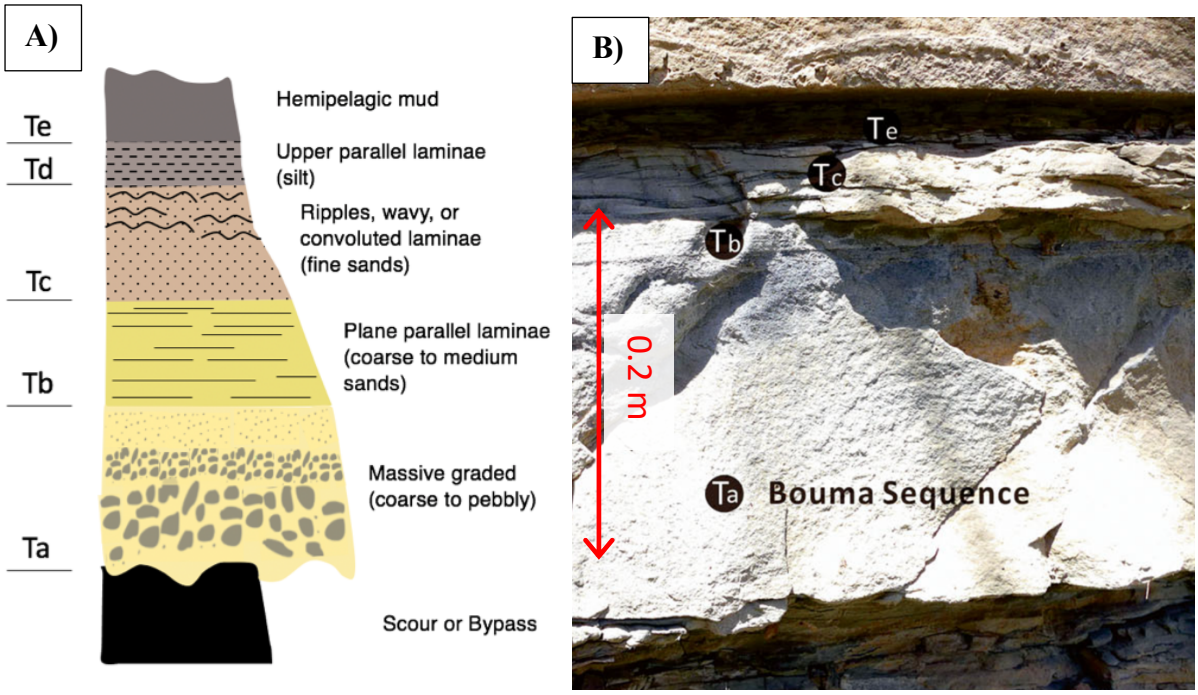

Figure 1.1. Examples of a classic turbidite deposit showing normal grading (coarse-fining) that occurs during decelerating turbidity currents. A) Illustration of a turbidite that is subdivided into 5 sedimentary units (Ta, Tb, Tc, Td, Te; Bouma, 1962). B) Field photograph of a turbidite sequence in the Yanchang Formation, Ordos Basin (China; modified from Zhang and Dong, 2020). Note that Td is absent.

1.3.2. Experimental and theoretical studies that followed

Experimental and theoretical studies then enabled more complex insights into turbidity current dynamics. These dynamics include: flow initiation (Parsons et al., 2001; Davarpanah, Jazi and Wells, 2020), erosion and deposition (Middleton and Hampton, 1973; Parker et al., 1987; Akiyama and Stefan, 1985; Altinakar et al., 1990; Garcia, 1994; De Rooji and Dalziel,

2001; Mohrig and Marr, 2003), flow structure (Ellison and Turner, 1959; Middleton, 1966; Allen, 1971), and sediment dynamics (Garcia, 1994; Kneller & Buckee, 2000; Baas et al., 2005).

Notably, past laboratory experiments led to a classical description of turbidity current structure that includes 3 distinct regions, as shown in Figure 1.2: 1) a thick and fast head region (Britter and Simpson, 1978; Simpson and Britter, 1979; Huppert and Simpson, 1980; Kneller and McCaffrey, 1999; Marino et al., 2005), 2) a thinner and slower trailing body (Garcia, 1993; Buckee et al., 2001; Sequeiros et al., 2009), and 3) a tail that tapers as the flow wanes (Baas et al., 2005; Sequeiros et al., 2018).

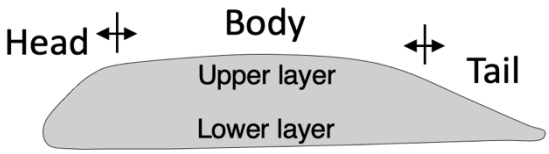

Figure 1.2. Generalised model showing the classic structure of a turbidity current, developed from observations during pioneering indirect studies (Ellison and Turner, 1959; Allen, 1971; Britter and Simpson 1978; Garcia, 1993; Buckee et al., 2001; Baas et al., 2005; Sequeiros et al., 2009). The flow is divided laterally into 3 regions (i.e. head, body, and tail) and vertically into two separate layers (i.e. upper and lower).

Flows are also considered to be vertically stratified, such as into an upper-layer that predominantly entrains ambient seawater, and a lower flow layer where seafloor sediment becomes entrained (Ellison and Turner, 1959). Based on this structure, flows can become self-sustaining when traveling with sufficient speeds, as sediment grains within the flow can provide more energy than they consume to suspend. This self-sustaining mechanism is known as 'ignition' (Pantin, 1979; Parker, 1982), and offers one explanation for such long run-out distances, across relatively flat slopes. In contrast, flows have been shown to dissipate once they deposit sediment. However, flows in the field are known to be much faster than experimental flows (Baas et al., 2005; Azpiroz et al., 2017), and thus are likely to suspend sediment or erode more effectively than slower moving laboratory flows.

Analytical and numerical models are commonly used as an alternative method to bridge the gap between the much smaller scale of laboratory experiments, and the limited number of direct observations. First, box models were used to reproduce flow behaviour from lock-

exchange experiments (Huppert and Simpson, 1980). But such models produced flows with unrealistically short run-out distances, since ambient fluid entrainment is neglected. A better alternative is to simplify turbidity flows into depth-averaged parameters (Ellison and Turner, 1959; Pantin, 1979; Parker, 1982). Most notably, Parker et al. (1987) developed a four-equation entrainment model that includes sediment exchange between the seafloor and the lower flow layer. Without this exchange, flows will infinitely grow in volume (Ellison and Turner, 1959). The accuracy of depth-averaged models is limited largely by the absence of vertical changes in the flow (i.e. velocity and sediment concentration), and by the assumption that flow grain sizes are uniform. These aspects are fundamentally at odds with the dynamic and vertically stratified character of turbidity currents. A promising numerical approach is to use methods that resolve vertical flow structure, with model inputs that have been calibrated against deposit records and laboratory experiments. These methods include: direct numerical simulations (DNS; Hartel et al., 2000; Cantero et al., 2012; Luchi et al., 2018), large eddy simulations (LES; Piomelli and Balaras, 2002; Meneveau and Katz, 2000; Stevenson et al., 2014) and Reynolds-averaged Navier Stokes (RANS; Garcia et al., 2008; Sequeiros et al., 2009). DNS is regarded as the most accurate of the three approaches (Meiburg et al., 2015), but requires high computing power that is only feasible for modelling over short distances. Currently, all of these types of models are poorly validated against full-scale field observations, which hinders our understanding of these dynamics flows. The acquisition of field data is essential to address long-standing knowledge gaps, and to validate existing models.

1.4. Turbidity current monitoring: A transition to high resolution direct observations

The acquisition of direct turbidity current data has been catalysed by advancing technology and improved deployment methods. This new generation of field data is essential for further step changes in our understanding of these remarkable submarine flows.

1.4.1. Low resolution field monitoring

The presence of active turbidity currents in the oceans was first signalled by seafloor cable breaks (Heezen and Ewing, 1952, 1955; Shepard, 1954; Heezen and Drake, 1964; Ryan and Heezen, 1965; Piper and Aksu, 1987). From these cable breaks, it then became possible to

quantitatively describe the flow run-out distance and trajectory; additionally, the time elapsed between breaks constrained frontal flow speeds (Heezen and Ewing, 1952; Piper and Aksu, 1987). But observations from cable breaks can be uncertain; for example, when determining front speeds, it is assumed that cables are broken by the flow front. Nevertheless, cable breaks provide valuable direct information on the frequency, speed, and timing of flows at sites worldwide (e.g. Canada, USA, Taiwan, and Congo Canyon; Talling et al., 2015; Clare et al et., 2020).

Following cable break evidence, the first turbidity current field experiments mostly relied on current meters that recorded flow velocities at just one height above the bed. Current meter measurements tended to be widely spaced in time, such as every 10 minutes, and with only one current meter deployed along the flow path (Inman et al., 1976; Shepard et al., 1977). However, later work by IFREMER (Institut Français de Recherche pour l'Exploitation de la Mer) and others captured current meter measurements at multiple sites (Xu et al., 2004; Khripounoff et al., 2009; Vangreisheim et al., 2009). Notably, this early work captured flows that reached speeds of up to 3.5 m/s (Prior et al., 1987; Vangreisheim et al., 2009). However, the results from these pioneering works emphasised the need for a vertical profile of measurements. But such progress depended upon a technological breakthrough that would enable more frequent measurements, at multiple heights above the seafloor.

1.4.2. High resolution monitoring

The development of lithium-ion batteries and advancements in computing led to the invention of the ADCP (Acoustic Doppler Current Profilers), which revolutionised in-situ flow monitoring. ADCPs use the Doppler shift of acoustic sound waves as they reflect off moving particles to measure flow speeds at multiple heights in the water column (Teledyne RD Instruments, 2011). The intensity of acoustic echoes from suspended particles (i.e. backscatter) can be used as a proxy for sediment concentration (see following section for more detailed explanation; Gartner, 2004; Ha et al., 2011; Lintern et al., 2016).

In an effort to capture a wide range of information, turbidity current experiments also used measurement instruments other than ADCPs. These additional instruments include: Acoustic Monitoring Transponders (AMT) that measure seafloor displacement in the

horizontal and vertical components (Speiss, 1985), where changes in pressure are used to resolve the vertical component (Polster et al., 2009). In the horizonal direction, distance measurements are derived from the acoustic travel time between two or more transponders (i.e. direct-path acoustic ranging; for a detailed review see Petersen et al., 2019). Sediment traps and backscatter sensors (OBS) are also used to acquire measurements of grain size and suspended particle concentration, respectively. To summarise, sediment traps have been deployed to collect sediment directly from within turbidity currents (Xu et al., 2010, 2014; Liu et al., 2016; Paull et al., 2018), and this data provides a broad indication of the grain size distribution carried by turbidity currents. But sediment traps are unable to capture more detailed flow behaviour, as grain size data from traps poorly correlates with flow velocity (Maier et al., 2019). OBS sensors offer a slightly better alternative, by measuring the amount of light (i.e. visible or infrared) that becomes backscattered from particles suspended in the water column. However, the accuracy of OBS sensors is greatly affected by variations in grain size, and sensors also become quickly saturated at high particle concentrations (Black and Rosenberg, 1994; Wren et al., 2000).

Consequently, progress in turbidity current field monitoring has historically been limited by a lack of both detailed velocity measurements (at multiple heights above the seafloor), and direct measurements of sediment concentration. These challenges are in part solved by the use of acoustic technology such as ADCPs, which are discussed in detail in the following section.

1.4.3. Acoustic Doppler Current Profiler velocity and backscatter measurements

Acoustic Doppler Current Profilers (ADCPs; Figure 1.3) used in turbidity current field experiments typically have four transducers, that each emit separate acoustic beams. These beams are divided into vertical segments termed bins or cells. Sound waves travel along these beams at a set frequency and become scattered in the form of echoes when encountering small particles (i.e. sediment, zooplankton) in the water column. The frequency offset (i.e. Doppler shift) between the originally emitted wave and the returning frequencies of each echo, indicates the water speed. For each ADCP beam, these velocities are averaged over equal depth intervals (termed bins), for a defined vertical range of the water column (i.e. profiles). An individual beam corresponds to a single velocity component, which is expressed in terms of earth

coordinates (i.e. East, North and Vertical). A fourth error component is also necessary to ensure the accuracy of the three main beams, as each beam is oriented in a different direction, thus they do not typically measure the same parcel of water. Thus, velocity measurements can be very different between pairs of beams (i.e. beam 1 and beam 2, or beam 3 and beam 4; Figure 1.3), and this is known as the error velocity. To improve data accuracy, the user can define an error velocity threshold, which ensures that any velocities outside this criteria are discarded. These unresolved data points lead to blank patches of data (see Chapter 4). Additionally, water parcels smaller than the footprint of all 4 beams can go unseen by the ADCP (Figure 1.3B), due to a combination of the error velocity threshold and the acoustic beam angle. Thus, relatively small-scale changes in flow velocity are more likely to fall outside the velocity threshold, remaining unresolved (Teledyne RD Instruments, 2011).

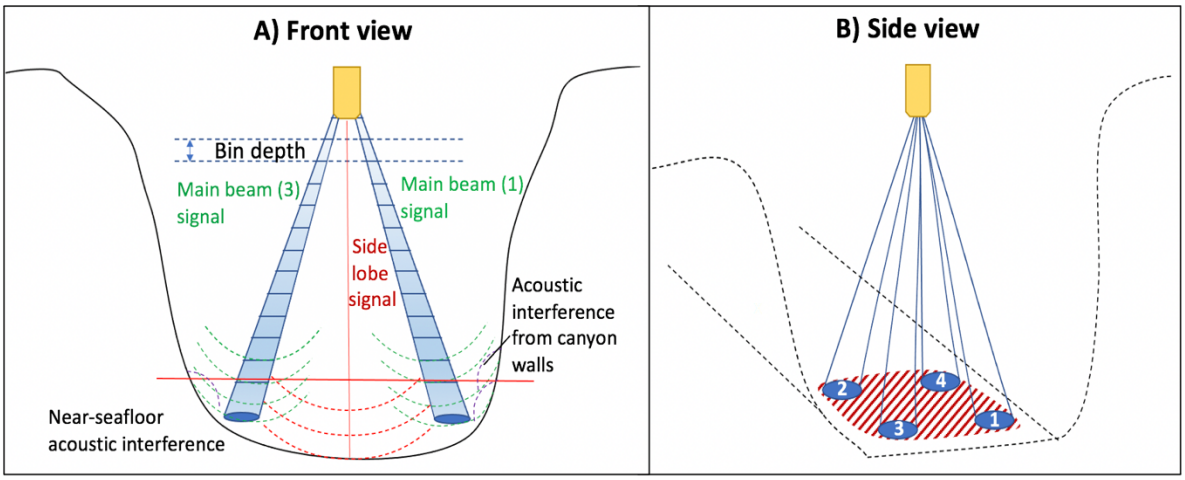

Figure 1.3. Illustration of an ADCP (not to scale) measuring profile data while suspended in a canyon channel. Measurements are recorded along four acoustic beams (in blue) which are shown from two different perspectives. **A)** front view where only the forefront beams are visible. Each beam is angled at 20 degrees, and emits an acoustic signal (in green) that records data over identical depth intervals (i.e. bins). However, significant acoustic interference can occur in the near seafloor region (below red line) from two main sources. 1) Acoustic energy that leaks to the side of the main beams (i.e. side lobe signal; in red) and reaches the seafloor first. 2) Canyon topography that reflects the acoustic signal before it reaches its target. **B)** Side view shows all four ADCPs are grouped into pairs (white numbers). ADCPs can encounter difficulty resolving velocity data when fluid is narrower than the ADCP beam footprint (red hatched square).

ADCPs also record the strength of acoustic backscatter, as well as the Doppler frequency shift. Thus backscatter provides insights into the concentration of particles suspended in the water column, together with their grain size (Thorne and Hanes, 2002). The strength of the returning (backscattered) signal is recorded as Echo Intensity Counts (EIC), which are broadly equivalent to decibels (Teledyne RD Instruments, 2011). Backscatter is used

with caution as a proxy for sediment concentration, since the strength of the return echo depends on both the size of the target particles and their concentration. Thus, two unknown parameters control the measured echo strength. A more robust approach is to use multiple ADCPs that operate on at least two different frequency systems. Based on this approach, a novel method by Simmons et al. (2020) is capable of deriving sediment concentrations; using an explicit method that extends earlier work by Lee and Hanes (1996). Sediment concentration profiles are estimated iteratively in this approach, by testing a number of different grain size distributions until a given concentration profile produces similar amounts of acoustic backscattering (bed echo attenuation) as those measured by the ADCP. Although this method contains a number of assumptions, the most notable is that sediment grain size does not vary with height above the seabed (Simmons et al., 2020).

1.4.3. ADCP Configuration

To acquire meaningful measurements of turbidity current velocity and backscatter, the ADCP settings and configuration must be defined by the user. Key considerations include orientation, sound wave frequency, bin size, and sampling rate. First, ADCP orientation refers to whether the instrument is deployed facing upwards, such that it is positioned towards the base or underneath a turbidity flow, or facing downwards; and also suspended either within, or above the flow. Most fieldwork experiments have deployed downward facing ADCPs at a significant height above the seabed, to ensure protection from the most violent flow regions (that commonly occur within close proximity to the seafloor). The temporal and vertical (bin) resolution of data collected during these experiments is largely determined by frequency of sound packages emitted, (‘pings’) and the number of pings per measurement. Specifically, higher frequencies enable smaller scale bins, with the caveat that higher frequency sound waves penetrate shorter vertical distances. Thus, the entire vertical measurement range is spatially shorter than lower frequency measurements. In conjunction with ADCP frequency, the bin size also determines the spatial resolution of the measurements in the vertical direction. The sampling (ping) rate determines the time interval between measurements, and thus the temporal frequency of data. In this thesis, ADCPs were configured with frequencies of 75 kHz and 300 kHz, bin sizes ranging from 0.75-4 m, sampling rates between 9-30 s, and heights ranging between 44-152 m above the seafloor.

1.4.4. ADCP Limitations

ADCPs can encounter difficulty in recording accurate velocity or sediment concentration data, mainly due to: the dense nature of turbidity currents, the seafloor bathymetry, the instrument design and the mooring configuration. First, ADCPs generally do not capture the near-bed layer of turbidity flows, as sediment concentrations are highest in this region, inhibiting much of the acoustic energy from penetrating into the lower flow. For downward facing ADCPs (the most common configuration), this dense near-bed layer also exacerbates the fact that the acoustic signal is pre-disposed to become weaker towards the seafloor, due to spreading-attenuation. A lack of near-seafloor data is a considerable disadvantage, as the near-bed layer of a turbidity current is thought to play a key role in driving the flow forward (Luchi et al., 2018). Second, the acoustic signal from an ADCP becomes distorted from direct and indirect forms of signal interference. Some direct interference occurs when sound waves reflect off the seafloor. But the largest source of interference is generated from acoustic energy that leaks beyond the 4 main beams. This excess energy is emitted directly underneath the ADCP, facilitating a shorter travel distance to the seafloor in comparison to the angled main beams. Additionally, V-shaped canyon walls and undulating seafloor bathymetry can accentuate this problem. Despite that the side lobe energy is lower than the energy from the main beams, the seafloor reflections are stronger than reflections from particles in the water column. Consequently, side lobe interference can affect the bottom ~10% of measurements (Teledyne RD Instruments, 2011). Overall, a careful balance between mooring design and ADCP configuration is needed to ensure that the data is of sufficient quality and quantity.

1.4.5. Key successes in field-based monitoring

Ground-breaking insights into turbidity current behaviour have resulted from a number of successful recent field campaigns, which have used moored ADCPs (Figure 1.4). These field projects include submarine canyon systems offshore from California (Xu et al., 2004, 2010; Paull et al., 2018), West Africa (Cooper et al., 2013, 2016; Azpiroz- Zabala et al., 2017), Taiwan (Liu et al., 2012; Zhang et al., 2018), and the Mediterranean (Khripounoff et al., 2012; Puig et al., 2012; Martín et al., 2014; Ribó et al., 2015). Firstly, Paull et al., (2018) recorded detailed direct measurements of turbidity currents in Monterey Canyon, with flows reaching front speeds of up to ~ 7 m/s. Experiments in the Congo Canyon showed turbidity events are

some of the longest sediment flows recorded on Earth, as single flows were observed to persist for up to 10 days (Cooper et al., 2013; Azpiroz et al., 2017). Additionally, monitoring efforts in the Var Canyon and Gaoping Canyon (Taiwan) demonstrate that river flooding can trigger turbidity currents. In the case of Goaping Canyon, typhoons can contribute to hyperpycnal river-mouth flow conditions, which also trigger erosive turbidity currents (Zhang et al., 2018). Beyond submarine canyons, a number of high-resolution studies have been conducted in Canadian fjords (Hughes-Clarke et al., 2016; Stacey et al., 2019) where shallower depths (between 50–250 m) allow for easier instrument deployment, and events are often relatively frequent. Seminal work by Hughes Clarke et al., (2012; 2014) in the Squamish River Delta in Howe Sound, British Columbia included ~90 multibeam surveys, and the capture of 95 turbidity current events offshore three river channels. These data provided the first field scale observations to support the link between dense near-bed layers and active migration of crescent shape bedforms (Hughes Clarke, 2016).

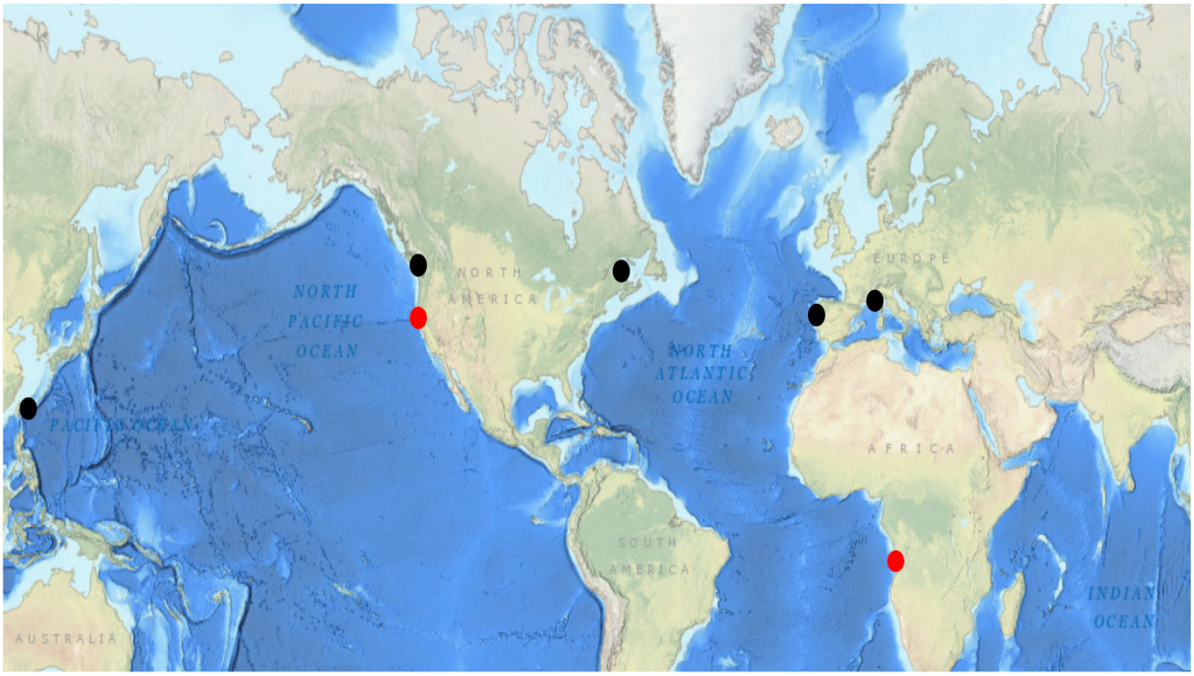

Figure 1.4. Bathymetry map of seven field locations where turbidity currents have been monitored using ADCPs (coloured dots; see Clare et al., 2020 for further details). Red dots indicate field studies relevant to this thesis. Map obtained from the National Oceanographic and Atmospheric Administration (NOAA) bathymetric data repository https://www.ncei.noaa.gov/maps/bathymetry/.

1.5. Field monitoring studies relevant to this thesis

The backbone of this thesis is formed by sub-minute data acquired from turbidity currents in Monterey Canyon, offshore California (USA), and the Congo Canyon, offshore

West Africa. At each field site, mooring arrays were fitted with a comprehensive range of equipment and sensors, which were suspended at various heights above the canyon floor. In the following section, these mooring arrays and field experiments are described in detail.

1.5.1. Monterey Canyon, offshore California (USA)

During an 18-month period (October 2015-April 2017), seven moorings were distributed over 50 km in Monterey Canyon (Figure 1.5; Paull et al., 2018), which is one of the largest submarine canyons on the West Coast of the USA. The canyon head lies only ~50 m offshore, and longshore drift primarily feeds sand to the canyon head. Sediment is then flushed through the canyon by turbidity currents (Paull et al., 2010). From the upper to mid-canyon, four moorings (MS1-MS4) were placed in numerically ascending order downstream, at water depths between ~300-1450 m (Figure 1.5C; Paull et al., 2018). At the MS4 mooring site, the canyon channel abruptly narrows from >250 m to <45 m, due to a constriction known as the Navy Slump (Figure 1.5A). The remaining three moorings (MS5-MS7) were deployed from the mid-canyon to a water depth of ~1850 m and a distance of ~20 km (Figure 1.5A). Each mooring was fitted with either one or two ADCPs that were suspended ~65 m above the seafloor. Each ADCP typically had vertical bin spacing of 1 m, with a sampling rate of one measurement every 30 seconds. An exception was site MS6 (Figure 1.5B), where a McLane Profiler autonomously traversed its mooring line, over a 500 m range above the seafloor (Figure 1.5C). Six moorings also contained sediment traps at heights of either 10, 75 or 300 m above seabed. A few moorings were also equipped with conductivity, temperature and depth (CTD) sensors that measured seawater temperature and salinity at 10 or 11 m above the seafloor (Figure 1.5C).

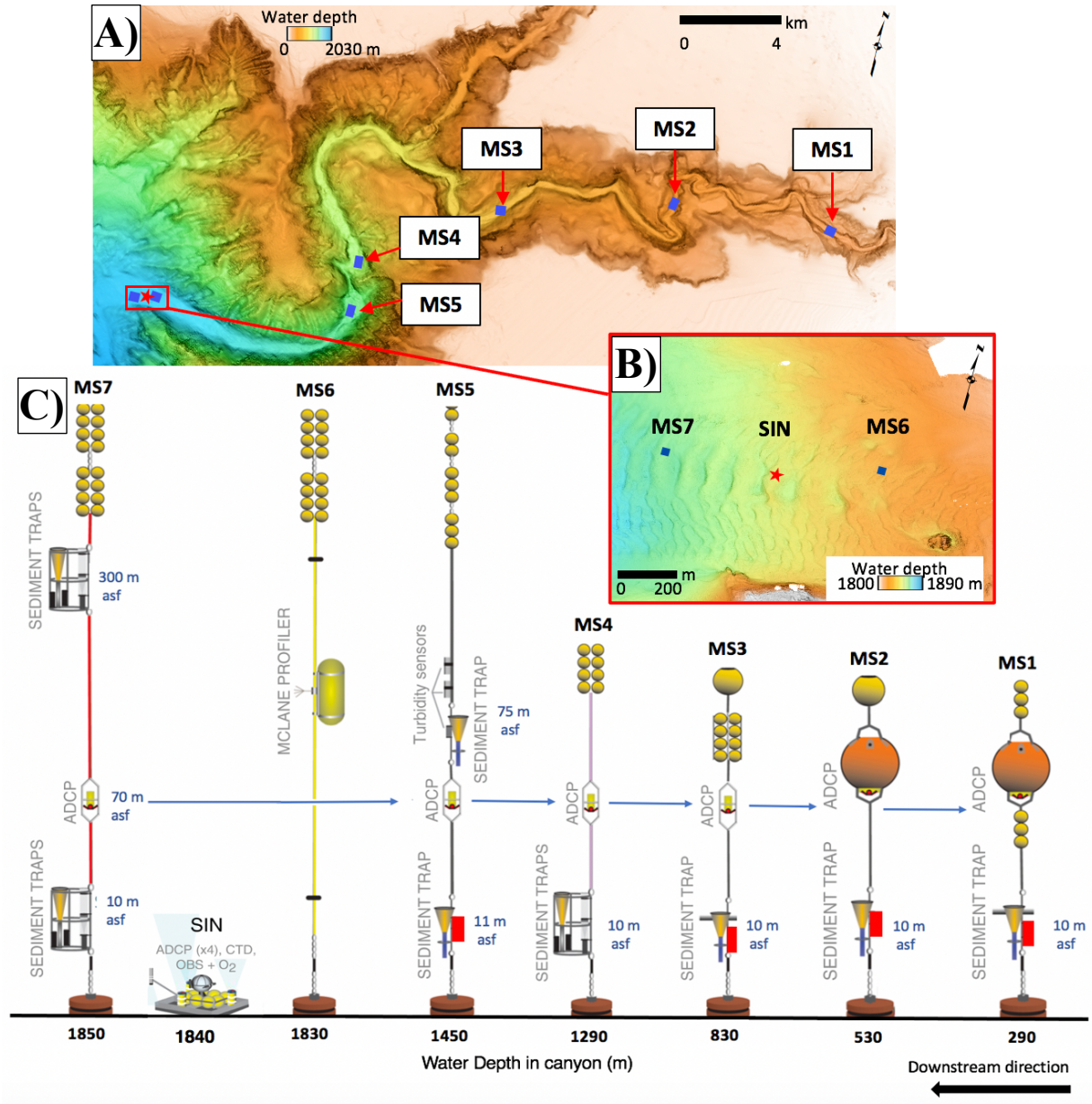

Figure 1.5. Location map and equipment used during the Monterey Canyon experiment from Oct 2015 to April 2017. **A)** Bathymetry map showing the locations of seven moorings (blue squares; labelled MS1-to-7) deployed within Monterey Canyon, offshore California. **B)** Inset map (red border) shows locations of deepwater moorings (>1800 m; Seafloor Instrument Node is abbreviated to SIN). **C)** Schematic illustration (not to scale) of the mooring array (MS1-MS7) deployed in the Canyon. Mooring stations were suspended at varying heights above the seafloor (asf; in blue), using flotation packs (yellow circles) and anchor weights (brown circles). Six mooring stations were fitted with a 300 kHz ADCP that was suspended 70 m above the seafloor (asf; blue arrows). Profile data was measured over 1 m vertical intervals (i.e. from the instrument to the seafloor), every 30 seconds. Conductivity temperature and depth sensors (CTD; red box) were fitted to some moorings (MS1, MS2, MS3, MS5). MS6 was fitted with a McLane profiler (yellow capsule) that collected CTD measurements for 500 m between two bumper snubs (in black), which were positioned 3 m and 503 m asf. With the exception of MS6, each mooring also contained at least one sediment trap, suspended at heights of 10, 11 or 300 m asf. Modified from Paull et al., (2018).

1.5.2. The Congo Canyon, offshore West Africa

The Congo Submarine Canyon starts in the Congo River estuary on the Atlantic Coast of Africa, between Angola and the Democratic Republic of Congo. The canyon-head is connected directly to the Congo River-mouth, the second largest river by water discharge in the world (Shepherd and Emery, 1973). From September 2019 to January 2020, eleven moorings were distributed from the upper canyon to the abyssal fan, a distance of ~800 km (Figure 1.6A-B; Talling et al., 2021). This Congo Canyon project is the first to monitor turbidity currents at depths >2 km. The first seven moorings were located at depths between 1575–2,200 m in the upper canyon (Figure 1.6B), with an additional four lower canyon moorings deployed at a water depth between 4,000–4,730 m (Figure 1.6A; Talling et al., 2021). Similar to the Monterey Canyon experiment, the Congo Canyon moorings were fitted with either one or two downward pointing ADCPs, but in the Congo Canyon these ADCP were suspended at heights ranging from 35 to 250 m above the seafloor (Figure 1.6C). Velocity and backscatter (a proxy for sediment concentration) profiles were measured over vertical intervals of 0.75 m or 4 m, where the time between measurements ranged from 9 to 45 seconds. ADCPs were also fitted with CTD sensors that recorded seawater temperature and salinity. Three upper canyon moorings and one distal mooring were also fitted with sediment traps at 22 or 40 m above the seafloor.

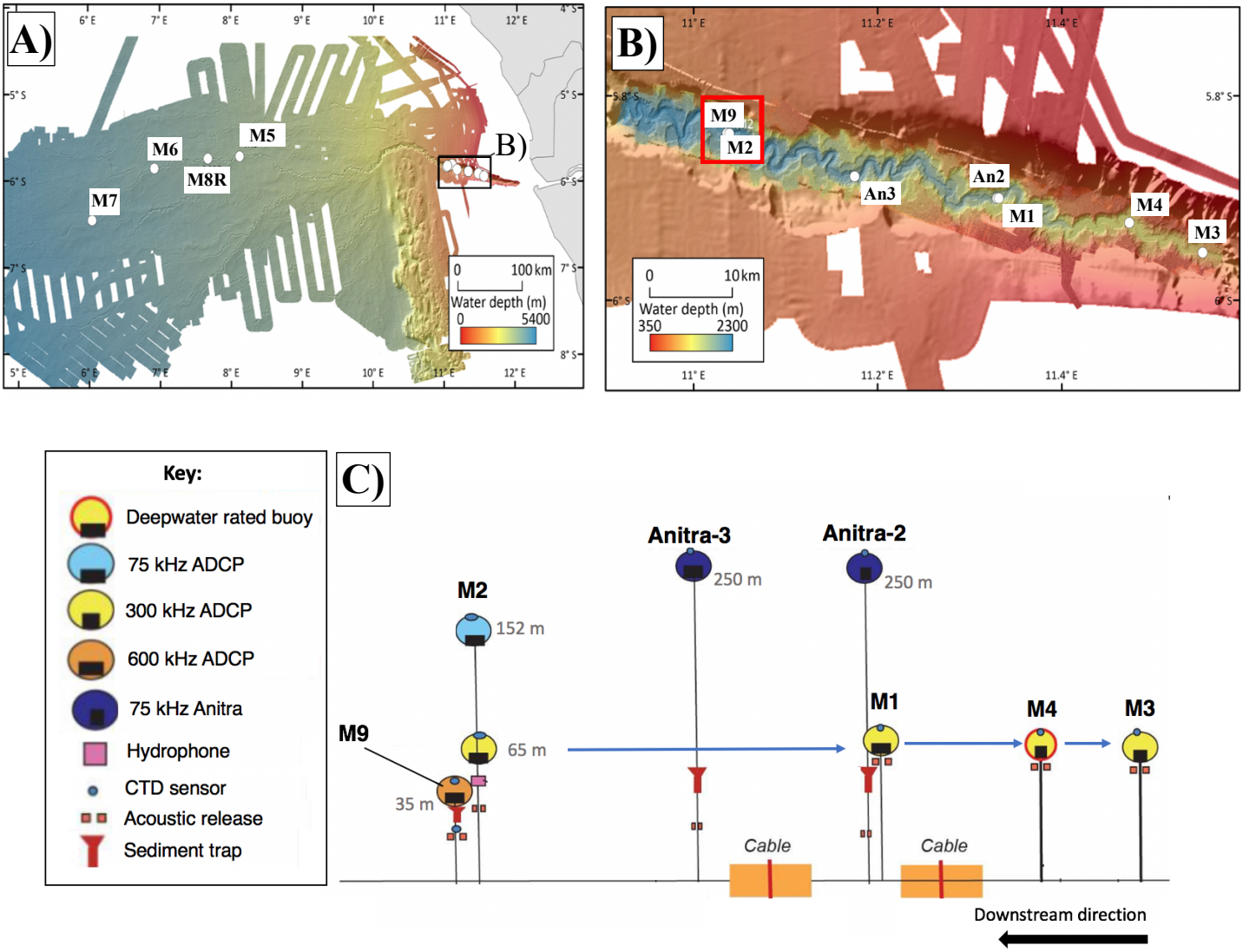

Figure 1.6. Location map and equipment used for the field measurements in the 2019-20 study of the Congo Canyon. **A)** Location of all mooring stations deployed during the Congo Canyon 2019 field study. **B)** Location of upper mooring stations, with the location of moorings M9 and M2 used in this study outlined by a red box. **C)** Schematic illustration (not to scale) of only the upper Congo Canyon moorings, which were deployed from Oct 2019 to Jan 2020. Each mooring (M) was fitted with different frequency ADCP instruments (blue, yellow, and orange circles) that were suspended at varying heights above the seafloor (asf; in grey). M3 was located closest to the canyon head, while the most distal mooring M9 was located ~ 90 km downstream (black arrow). Over this upper stretch of the canyon, two seafloor cables horizontally transect the seabed (orange rectangle). Moorings 1 to 4 each contained a 300 kHz ADCP that was suspended 65 m asf (blue arrows), and recorded measurements every 11 seconds, over 1.5 m vertical bins. In addition, M2 also contained a 75 kHz ADCP that was suspended 152 m asf, and recorded measurements every 9 seconds over 4 m bins. The Anitra moorings (2 and 3) were also fitted with 75 kHz ADCPs that were configured identically to the 75 kHz mooring on M2. Distally, at M9 a 600 kHz ADCP was suspended 35 m asf, and recorded measurements every 11 s over 0.75 m bins.

1.6. Justification of the choice of datasets used in this thesis

This thesis seeks to understand how turbidity currents evolve as they travel from the continental shelf to the deep sea, resulting in three chapters presented in the following sections. The data that forms these chapters were carefully chosen from mooring sites and/or measuring equipment that could offer new perspectives on turbidity current behaviour over time.

For instance, in Monterey Canyon, a novel McLane Profiler vertically traversed its mooring line, in either an upward or downward direction, measuring seawater temperature, salinity, and conductivity. These datasets provide the first opportunity to observe vertical changes in turbidity current seawater density over time (Chapter 2). Additionally, data was successfully captured across the largest spatial extent of a turbidity current's path to date, allowing unprecedented observations of changes in flow volume. This data can then be used to test existing lab-based entrainment models (Chapter 3). However, fieldwork in the Congo Canyon was disrupted by a number of exceptionally powerful events, which caused some moorings to break and surface on the 10th October and 27th December 2019, while the remaining few surfaced on the 16th January 2020. Thus, similar continuous observations across more than one location is not possible. Despite this setback, valuable ADCP data were recorded by two moorings in the upper canyon, at sites that were located unusually close together (~ 300 m). For the first time, this mooring configuration enables observations of a turbidity current flow front, with higher spatial resolution than any field experiments to date (Chapter 4).

Chapter 2: What affect(s) do turbidity currents have on ocean stratification?

Abstract

Submarine turbidity currents form the deepest canyons and largest sediment accumulations on Earth. However, due to the destructive nature of turbidity currents, few direct observations of these submarine gravity flows exist, and consequently they remain poorly understood. Much of our insight into turbidity currents instead comes from laboratory and theoretical modelling, and studies of their deposits. Previous theory and experiments have suggested that once sufficient sediment settles from a turbidity current, the remaining sediment-water mixture might become positively buoyant and rise vertically (termed 'lofting'). In nature, this process is observed during volcanic eruptions, where hot pyroclastic flows can reverse their density, and rise as buoyant plumes of ash. Lofting is important because it profoundly affects flow runout distance and deposit structure. This chapter presents the first detailed field measurements of lofting within submarine turbidity currents. Data were acquired in Monterey Canyon by a profiler that traversed vertically for 500 m, every 4.5 hours. These data indicate that lofting occurs with water temperature and density anomalies persisting for 0.75 days. Long after these anomalies dissipated and flows stopped moving, turbid water lingered for 2 further days. Thus, lofting is prolonged and generates persistent near-static clouds of fine sediment, an observation that is absent from past models.

2.1. Introduction

Seafloor sediment flows called turbidity currents are driven down-slope by density differences between the sediment and water they carry, and that of the surrounding seawater. It is important to understand turbidity current behaviour, as these flows form many of the deepest canyons, longest channels, and largest sediment accumulations on our planet (Bouma et al., 2012). Turbidity currents also play an important role in: the transfer and burial efficiency of organic carbon in the deep-sea (Galy et al., 2007; Schlünz and Schneider, 2000), nutrient supply to seabed ecosystems (Canals et al., 2006), and in ocean ventilation; as these flows also carry fresher water into the deep sea (Kao et al., 2010). Some turbidity currents are very

powerful, and they can break seafloor cable networks that underpin the global internet (Carter et al., 2014), or damage valuable oil and gas pipelines (Clare et al., 2017). Turbidity current deposits formed over geological timescales can host valuable oil and gas reserves, which occur in locations worldwide (Wiemer and Link, 1991). However, submarine turbidity currents are challenging to measure due to their deep-sea locations, unpredictable occurrences, and most importantly, their ability to damage sensors placed in their path. Consequently, there are very few direct observations of these flows in action, which ensures that they remain poorly understood.

This chapter presents some of the most detailed direct measurements of turbidity currents yet, to determine whether these flows can reverse in buoyancy and rise vertically, during a process that has been termed 'lofting' (Sparks et al., 1993). Whether a turbidity current lofts largely depends on its sediment load, and on the composition of seawater that the flow transports. In general, turbidity currents initially travel along the seafloor, as their sediment load provides excess density. However, interstitial water carried by a turbidity current is typically warmer than the ambient seawater, as these flows inherently move from shallower to deeper water depths (Quadfasel et al., 1990). Thus, once sufficient sediment has settled out of suspension, a turbidity current that contains warmer and less-dense water can reverse in buoyancy, and these positively buoyant sediment-water mixtures will loft. The occurrence of lofting in the ocean would be important, because it may affect how warmer and more-oxygenated surface waters are dispersed into the deeper ocean (Quadfasel et al., 1990). Additionally, lofting may profoundly affect the geometry and character of turbidity current deposits (Sparks et al., 1993; Gladstone and Pritchard, 2010), which form major hydrocarbon reservoirs worldwide (Wiemer and Link, 1991). These seabed deposits (called turbidites) are predicted to pinch-out abruptly where the flow lofts (Sparks et al., 1993; Gladstone and Pritchard, 2010). This study initially tests whether full-scale oceanic turbidity currents loft, and if so, seeks to understand the nature and timescales of lofting.

Previous understanding of lofting is based almost exclusively on laboratory experiments and theory. For example, Sparks et al. (1993) conducted experiments based on releasing a finite-volume mixture of particles and less-dense interstitial water, into a denser body of water. They then developed a theory that predicts how lofting affects the flow's spreading rate, as well as the point and time at which the front of a lofting flow detaches from the seabed (the lift-off point). Similarly, Hurzeler et al. (1996) predicted the spreading rate

generated by constant-volume releases of heavy particles, and applied a two-dimensional numerical model to predict the time evolution of a lofting flow. Hogg et al., (1999) then used the observations of Sparks et al. (1993) to develop a theory, which predicted the dependence of lift-off distance on the initial characteristics of the released fluid and suspended particles. Additionally, Gladstone and Pritchard (2010) described how lofting influenced the character of deposited sediment in laboratory experiments.

Although laboratory experiments form a significant proportion of our understanding of turbidity currents, they are limited by important scaling issues (Middleton, 1966). For example, laboratory flows tend to be much slower moving than their oceanic cousins, favouring relatively rapid sediment settling. The differences in scale and velocity between laboratory and oceanic turbidity currents also affects the time scales over which lofting occurs. Both laboratory experiments and theory may also omit key processes that are common in the oceans, such as internal tides in submarine canyons that help to suspend sediment (as will later be shown).

It is therefore important that the results of these indirect studies are compared and tested against full-scale oceanic measurements, to avoid a closed loop between experiment and theory. However, there are very few studies that have directly measured how temperature, salinity or turbidity (a proxy for sediment concentration) varies within full-scale oceanic turbidity currents. Thus, how lofting occurs in the field remains relatively unexplored. Previous field work was based on temperature and salinity measurements at either single heights above the seabed (Khripounoff et al., 2009), or profiles at a single location (Hughes Clarke, 2016). In an exceptional case, conductivity-temperature-depth (CTD) sensors measured profiles at two locations, however, they were spread 80 km apart (Kao et al., 2010). Yet, none of these previous field studies analysed the implications of their field measurements of water temperature and salinity in turbidity currents for lofting, due to limited resolution (temporal and spatial).

The proportion of shallow (warmer) water retained by a lofting turbidity current over time, might play a key role in buoyancy reversal (Quadfasel et al., 1990; Kao et al., 2010). Entrainment of ambient seawater is one of the main mechanisms that determines the temperature structure of turbidity currents (Akiyama and Stefan, 1985). Additional indirect works suggest that faster flows entrain greater volumes of ambient water (Ellison and Turner, 1959; Middleton, 1993). Ellison and Turner (1959) first presented a theory in which

entrainment is proportional to both the velocity of a turbidity current and to the bulk Richardson number. But there are few studies of entrainment and mixing in full-scale oceanic flows, particularly with respect to how mixing rates are linked to flow velocity. For example, a study in Scripps Canyon (offshore California) observed a correlation between greater entrainment and faster turbidity current velocities in the canyon axis (Inman et al., 1978). Then, in Bute Inlet (British Columbia, Canada), Prior et al. (1987) observed that faster turbidity currents had lower internal temperatures. The velocity at which these flows travel can relate to both mixing and the resulting temperature structure of water within turbidity currents. These processes also remain poorly understood, despite having important implications for lofting patterns and flow behaviour.

In this study, detailed observations are presented from two separate turbidity current events, which both travelled through the Monterey Canyon for over 50 km, into the deep ocean (>1900 m water depth). The fastest (up to 7.8 m/s) flow occurred on the 15th January 2016, while a somewhat slower flow (up to 4 m/s) occurred on 1st September 2016. These flows were observed at multiple locations along their pathway (Figure 2.1B-C), and at one of these locations, unusually detailed vertical transects of water-mass properties were collected (Figure 2.1D)

2.1.1. Aims

Herein, observations of velocity and seawater density are analysed, within a faster (7.8 m/s) and slower (4.8 m/s) turbidity current, to answer the following questions. First: does lofting occur? Second, as these data indicate that lofting does occur, this study then seeks to document and understand how lofting works. In particular, the temperature structure and evolution of faster and slower turbidity currents are compared, to understand how flow-velocity influences lofting. Finally, this chapter shows how the evolution of oceanic flows differs from past lofting models, and thus a new general model is presented, according to these field observations.

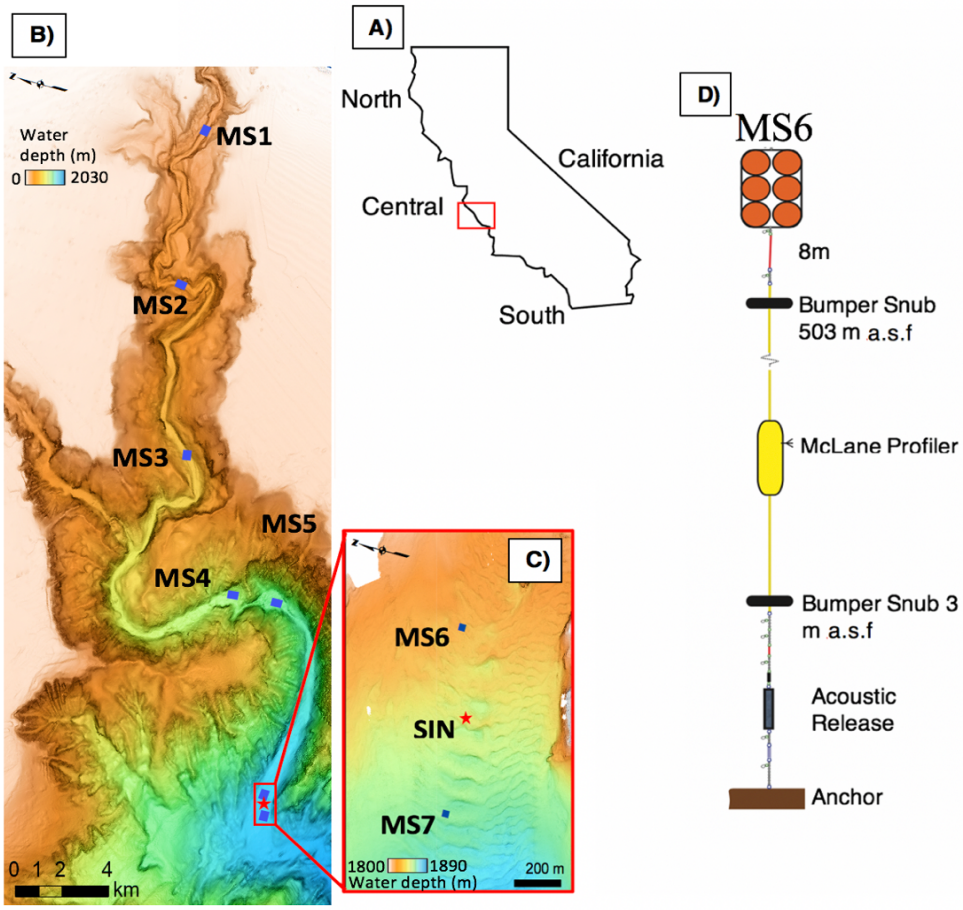

Figure 2.1. Location map and equipment used for the field measurements in Monterey Canyon **A-D**). **B**) Bathymetry map showing the location of moorings (blue squares; labelled MS1-to-7) deployed within Monterey Canyon, offshore California (inset map a). **C**) inset map (red border) shows locations of the McLane Profiler at MS6, Seafloor Instrument Node (red star; labelled SIN), and ADCP at MS7. **D**) Schematic diagram, not to scale, showing MS6, anchored at 1,827 m water depth. The McLane Profiler fitted to MS6 sampled at a rate of one measurement every 30 seconds. Additionally, the McLane traversed 500 m vertically through the water column, between 2 bumper snubs (located 3 m and 503 m above sea floor). The McLane Profiler thereby recorded measurements at water depths from 1,327– to 1,827 m. See section 1.5.1 for a detailed explanation of the entire mooring array and equipment used.

2.2. Methods

Data were acquired from Monterey Canyon where seven moorings were distributed from water depths of ~300 m to 1850 m; with Mooring 1 located closer to shore, and Mooring 7 located distally (Figure 2.1). Mooring stations are referred to by the letters MS, followed by the corresponding number (i.e. MS1 through to MS7). These moorings were deployed over an 18-month period, from October 2015 to April 2017 (Figure 2.1A-C; Paull et al., 2018; See Chapter 1 for a detailed overview). Acoustic Doppler Current Profiler (ADCP) velocity profile data were acquired from MS5 and MS7 (Figure 2.1B-C). These distal moorings were located ~ 50 km from the canyon head at water depths of between 1450-1850 m (Figure 2.1B-). At

these locations, the ADCPs were configured to measure profiles of velocity over 1 m intervals, from the seafloor to the instrument (65 m above the seafloor), with one measurement every 30 seconds. Additionally, a temperature sensor was fitted to these ADCPs, and recorded water temperature at a single height (65 m) above the seafloor. Downstream from MS5 (~ 9 km), a Seafloor Instrument Node (SIN; Figures 1.4C and 2.1C) was fitted with an upward-looking ADCP. At the SIN, velocity profiles were measured every 10 seconds at 1 m vertical intervals, over a 70 m range from the seafloor upwards. In between MS5 and the SIN (Figure 2.1C), an autonomous McLane Moored Profiler (referred to as "McLane Profiler" herein) was fitted to MS6 (~1830 m water depth; Figure 2.1D).

2.2.1. McLane Profiler measurements

The McLane Profiler alternated between upward and downward measurement cycles, and during each cycle it travelled 500 m along a fixed mooring line. This profile range was determined by bumper snubs placed between 3 m to 503 m above the seafloor (abbreviated to asf henceforth), which is equivalent to water depths of 1327–1827 m (Figure 2.1D). For clarity throughout the rest of this chapter, profile depths will be presented according to their relative height above the seafloor (i.e. 3-503 m asf). The McLane Profiler recorded seawater temperature, salinity, and turbidity (via strength of optical backscatter measured in NTU units). The water depth of the McLane Profiler was calculated as a function of pressure using a Seabird 52MP CTD and Teledyne RDI Micro CTD. Profiles were repeated every 4.5 hours during the first deployment (October 2015–April 2016) and every 6 hours during the second deployment (April 2016–October 2016).

2.2.2. Deriving sediment concentration from turbidity sensors

Ideally, direct measurements of sediment concentration would be used to support this study. However, there are currently few, if any, detailed measurements of sediment concentration from submarine turbidity currents (Wang et al., 2020). This lack of sediment concentration data partly reflects the destructive nature of turbidity currents. However, most available methods for measuring sediment concentration (e.g. optical light transmission and backscatter) become saturated at relatively low sediment concentrations. In particular, the difficulties in using proxy measurements (units of NTU) from optical light transmission

instruments to derive absolute sediment concentrations are well-documented (Sutherland et al., 2000; Xu et al., 2014). These turbidity sensors become saturated when sediment concentrations exceed a threshold value of < 100 kg/m^3 (Black and Rosenberg, 1994; Ochiai and Kashiwaya, 2010; Xu et al., 2014; Simmons et al., 2017). In this study, optical light transmission ('turbidity') data are therefore used to indicate simply whether significant sediment (above background concentrations) is present within the water column.

2.3. Results

In the following section, two individual flow events are analysed using ADCP-measured velocity data from MS5 and MS7, as well as the Seafloor Instrument Node. These velocity data are then compared to vertical changes in water-mass properties, which were measured every 4 or 6 hours, by a McLane profiler at MS6 (Figure 2.1D). Prior to describing these flow events, it is important to first determine the ambient conditions in the water column.

2.3.1. Ambient conditions

The field measurements capture ambient conditions that occur in between turbidity current events. The ambient temperature and salinity (T-S) ranges are given by the McLane Profiler, which collected measurements over a 1.5 year period from Oct 2015 to Apr 2017 (3 deployments of 6-months each). At MS6, temperatures ranged from ~2.9 to 3.3ºC (at 503 m asf); ~2.4 to 2.9ºC (at 250 m asf); and ~2.1 to 2.5ºC (at 3 m asf). Salinity (psu) ranged between ~34.49 to 34.54 psu, ~34.52 to 34.58 psu, and ~34.52 to 34.6 psu at these depths respectively. Using these ambient temperature and salinity ranges, the local seawater density was calculated using Millero's equation (Millero and Poisson, 1981). Thus, the ambient seawater has a minimum density of 1027.45 kg/m^3 at 500 asf, 1027.53 kg/m^3 at 250 m asf, and 1027.56 kg/m^3 at 3 m asf. It is also important to note that during normal conditions, transport of sediment and water in the canyon is dominated by a semidiurnal tide, which has peak velocities of ~ 0.6 m/s (Figures 2.3 and 2.5).

2.3.2. The January 15-16th flow event

The faster of the two turbidity current events arrived at ~ 21:43 UTC (MS1; Table 2.1) on the 15th January, and had maximum frontal (transit) speeds of ~7 m/s between MS2 and MS3 in the upper canyon (Paull et al., 2018). The flow then decelerated to speeds of 3-4 m/s between MS5 and the SIN (Figure 2.2A-B). By the most distal mooring (MS7), flow speeds were <2.6 m/s (Figure 2.2C). This January 15th event was also captured by the McLane profiler, when the flow reached MS6 early on January 16th. Thus, for clarity, this event will be referred to as the January event henceforth.

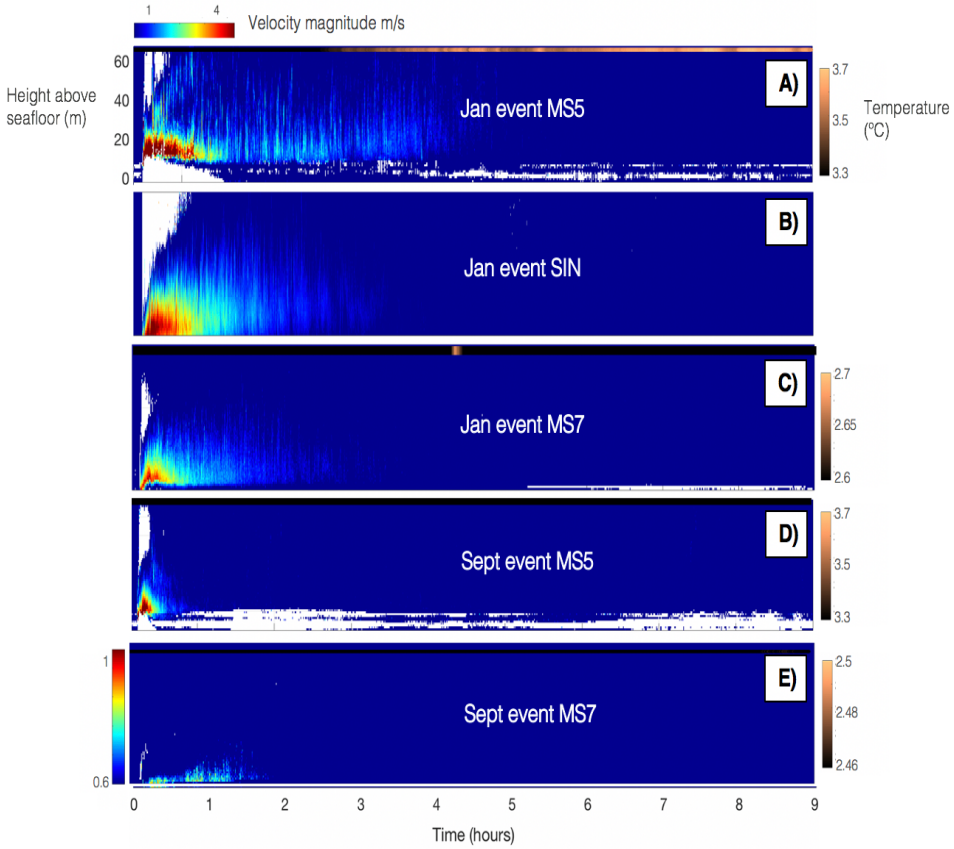

Figure 2.2. Time-series of ADCP-measured-velocity magnitude and seawater temperature during two separate turbidity current events, where ambient water speeds (<0.6 m/s) have been excluded (i.e. ambient speeds represented by dark blue shading). Both turbidity currents travelled through three lower canyon mooring stations (MS5, SIN, and MS7). **A-E**) Velocity profile data was recorded at each location every 30 s (MS5 and MS7) or 10 s (SIN). Each profile was vertically subdivided into measurements spaced at 1 m intervals, over the first 60 m of the water column (from the seafloor upwards). Note, that the September event had waned to speeds of <1m/s at MS7, and for this data to be visible from the ambient velocities, the upper threshold of the velocity scale was decreased to ~1 m/s. Seawater temperature (ºC; grading from black to brown) was recorded at a single height (65 m asf) above the seafloor, for most moorings (except the SIN during the Sept event). This time series of temperature is shown above each synchronous ADCP-velocity plot. The upper and lower thresholds of the temperature colour-bar has been set to the maximum and minimum ambient temperature measured at each mooring over a 48-hour period at this location. There are no SIN data available from the September event, as the instrument was damaged by the flow.

Table 2.1. Mooring locations and flow arrival times (UTC) during the 15th January and 1st September events

January 15th 2016 event	Mooring station number							
	MS1	MS2	MS3	MS4	MS5	MS6	SIN	MS7
Location along thalweg (km)	6.84	15.76	25.98	40.03	42.80	51.48	51.79	52.10
Flow arrival time at mooring (HH:mm:ss)	21:43:25	22:08:57	22:32:28	23:08:00	23:20:33	N/A	00:01:07	00:03:07
Sept 1 st 2016 event	**Mooring station number**							
	MS1	MS2	MS3	MS4	MS5	MS6	SIN	MS7
Location along thalweg (km)	6.65	15.82	25.98	N/A	42.74	51.37	51.79	52.19
Flow arrival time at mooring (HH:mm:ss)	01:30:54	02:07:21	02:46:13	N/A	03:44:32	N/A	04:28:14	04:32:40

Figure 2.3A shows time-series measurements of turbidity made by the McLane Profiler, as it ascends and descends every 4 hours. Additionally, ADCP-measured flow velocity (in grey scale) was recorded at a similar location (SIN; Figure 2.1B-C). Detailed time series temperature and conductivity (converted to salinity) measurements from the McLane profiler are also shown in Figure 2.3A, for sub-sets of the measurement period. These plots capture how water-mass properties vary through time, and the relative timing of anomalous water masses due to down-canyon flowing turbidity currents.

The first McLane profile occurred 0.6 hours after the January turbidity current arrived (at 00:01 UTC; Table 2.1) at the SIN location (Figure 2.3A). The time (t) of each profile is defined in hours, and is given relative to the flow arrival time at the SIN (~ 300 m upstream; Table 2.1); because the McLane profiler did not have sufficient temporal resolution to capture the flow arrival. During this first profile, within 45 m asf, the seawater was noticeably warmer (2.31ºC to 2.47ºC; Figure 2.3A) and of lower salinity. However, all measurements within this first McLane profile were within the ambient range (Figure 2.4). The second McLane profile was recorded at t = 5.2hrs (Figure 2.3A), when anomalously warm (3.2ºC maximum) and fresh (34.46 psu minimum) seawater occurred between 29-81 m asf. These anomalies were the largest detected for the entire January turbidity current event. Maximum temperatures (3.2ºC) occurred at ~80 m asf, and were >0.5ºC warmer than the ambient temperatures at this depth. Additionally, seawater density reached a minimum of 1027.43 kg/m^3 (Figures 2.3A and 2.4), while turbidity remained high (> 3500 NTU) throughout this warmer and lighter region of the water column (Figure 2.3A). At t = 14 hrs, a second ~20 m thick density anomaly occurred (284–302 asf; Figures 2.3A and 2.4), with a maximum temperature of 2.9ºC and salinity minimum of 34.53 psu. In particular, the maximum temperature anomaly is observed at ~278 m asf, which also corresponds with the highest turbidity (1300–2600 NTU; Figure 3A) and the lowest densities (1027.50 kg/m3; Figure 2.4). No additional anomalies were observed from the profiles collected from t = 17.5 hrs onwards. McLane Profiler turbidity measurements,

however, remained above-background concentrations (>250 NTU) for ~42 hrs after the flow arrived (Figure 2.5).

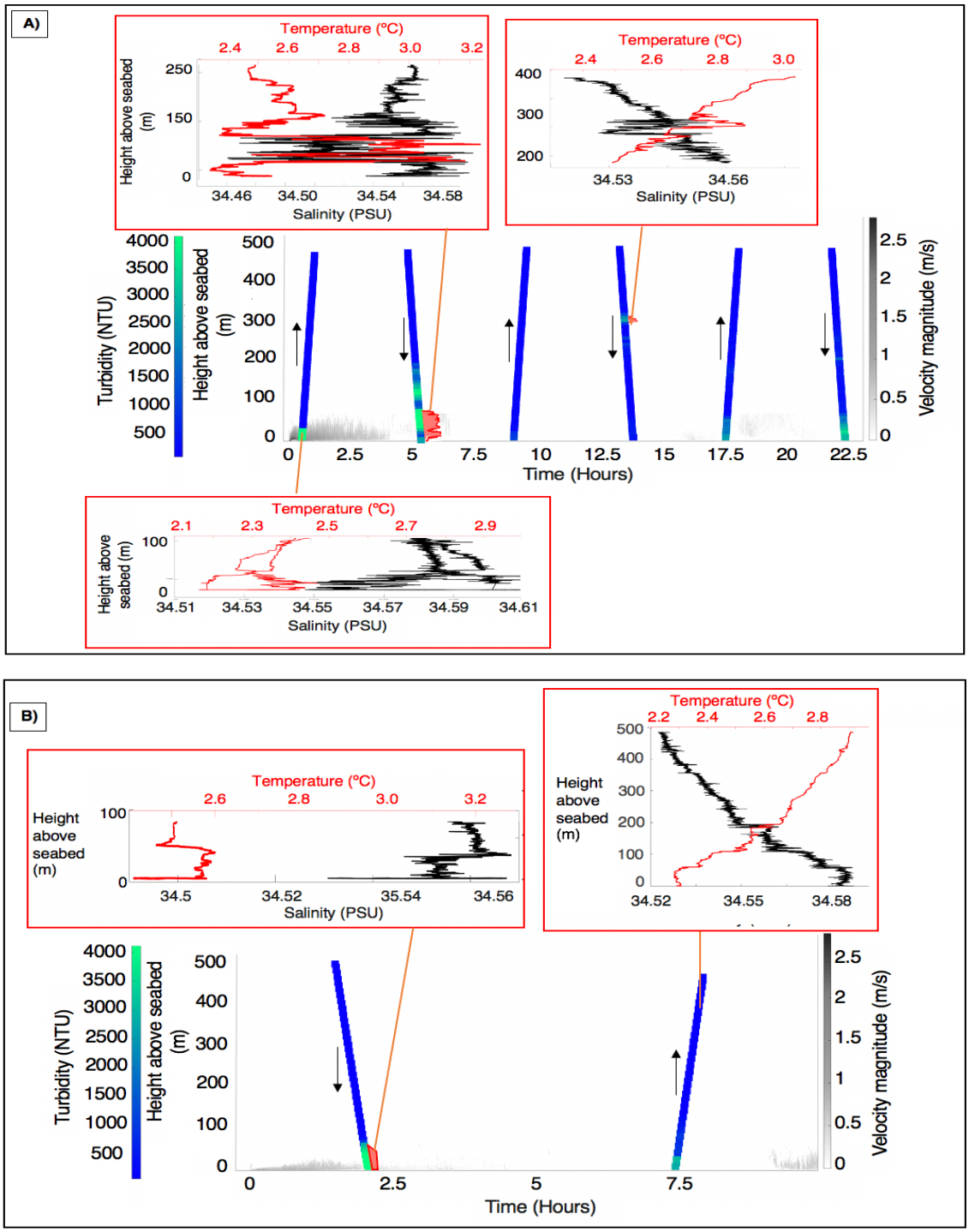

Figure 2.3. Changes in water-column turbidity, salinity and temperature through time as two separate down-canyon turbidity currents occurred. **A**) Data from the faster 15th January event. **B**) Data from the slower 1st September event. In both (A) and (B), ADCP measurements of flow-velocities (m/s) are shown in greyscale. Turbidity profiles (in NTU) are shown as inclined blue and green lines, measured by the McLane profiler as it ascended or descended through time (black arrows indicate direction of travel). A series of red inset panels show anomalous temperature (ºC; red) and salinity (psu; black) measurements, for a subset of water depths and times (shown by red arrows to the main figure). Anomalies were defined by values that fall outside the background conditions, (red shaded regions on main figure), as defined in Section 2.3.1.

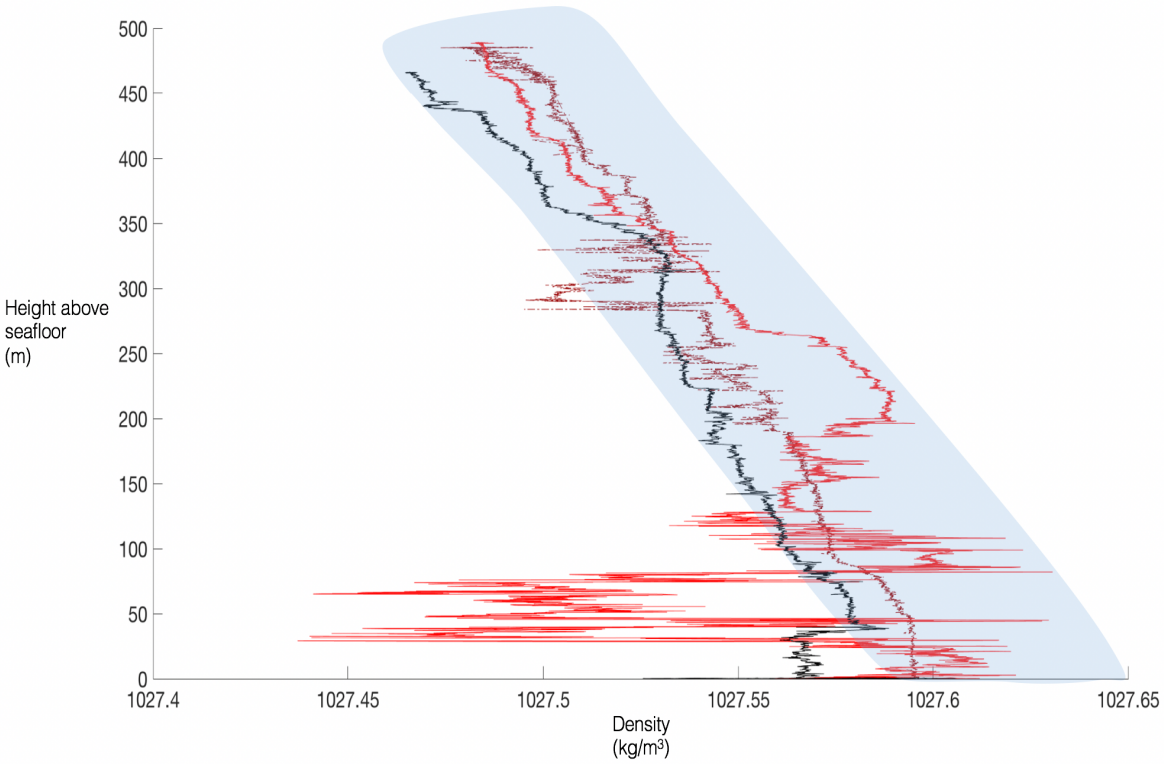

Figure 2.4. Changes in density are shown over 500 m of the water column from the seafloor upwards, during both the January 15th event (in red) and the 1st September event (in black). Seawater density profiles were derived from temperature and salinity profiles recorded by a McLane Profiler, according to Millero's equation (Millero and Poisson, 1981). The ambient seawater density (blue shaded band) was determined from McLane measurements collected over a 1.5-year period (Oct 2015-April 2017), excluding any turbidity current events. Low-density water anomalies are therefore defined as values that fall outside the ambient density threshold, represented by blue shading.

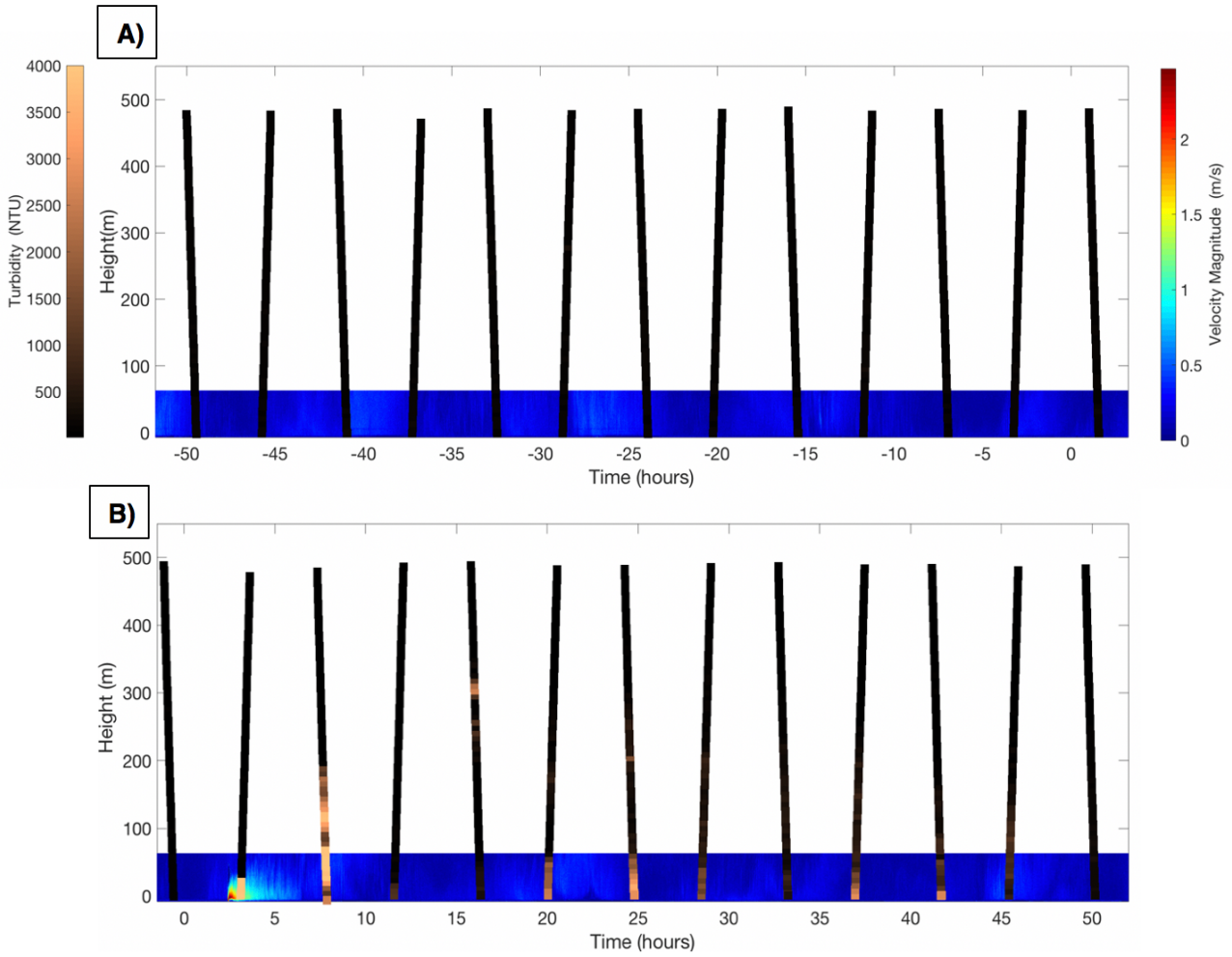

Figure 2.5. Vertical changes in water-column turbidity were detected every 4 hours at MS6 (inclined black and brown lines), over the lowermost 500 m of the water column. Approximately 300 m downstream from MS6, the SIN recorded ADCP measurements of seawater-velocities (m/s) every 30 seconds, over a 65 m range from the seafloor to the instrument (shown in blue grading to red). **A**) 50 hours prior to the January 15th event, background conditions consisted of low turbidity <500 NTU. **B**) The onset of the 15th January event (t=0) is associated with significantly turbid water (a peak of ~ 4080 NTU), which then remains above background for ~42 hours.

2.3.3. September 1st flow event

The second flow occurred at 1:31 UTC (MS1; Table 2.1) on the 1st September 2016 (referred to as the September event hereon) and had somewhat slower velocities. Flow transit speeds were >4 m/s in the upper canyon (at MS1; Paull et al., 2018), and then the flow decelerated to <1 m/s at MS7 (Figure 2.2E). For the September event, the flow arrival (t=0) is based on data from MS7 (~ 4.33 UTC; Table 2.1) which was located ~800 m downstream, since the SIN sustained damage during the flow. At t = ~2 hrs, a subtle (~0.05ºC; Figure 2.3B) temperature anomaly occurred over the first 42 m asf, as the seawater density reached a minimum of 1027.57 kg/m^3 (Figure 2.4). Turbidity values measured during this profile were high (~3800 NTU) over ~ 60 m from the seafloor upwards (Figure 2.3B: top-left inset). After

2 hours, no further profiles showed any abrupt changes in seawater density changes, although, turbidity remained above background conditions for 17.5 hrs.

2.4. Discussion

2.4.1. Does lofting occur?

Lofting is defined in previous work (Sparks et al., 1993; Hurzeler et al., 1995; Hogg et al., 1999; Gladstone and Pritchard, 2010) as the vertical, upward movement of a water-mass within a turbidity current. This rising movement is due to a reduction in bulk density of the turbidity current below that of the ambient seawater, leading to positive buoyancy (Figure 2.3A). The turbidity current contained warmer and fresher (i.e. less dense) water than the surrounding seawater, and sufficient sediment settles from the turbidity current; such that the positive excess density due to the turbidity current's water exceeds the negative excess density of the sediment it carries. As the September event waned, anomalously less-dense (warmer and lower salinity) seawater was observed at heights of more than ~40 m asf (Figure 2.3B). However, ADCP velocity data shows that the (moving) turbidity current was <20 m asf when it arrived at the McLane Profiler. Thus, the density anomaly was at least 20 m thicker than the velocity-anomaly caused by the turbidity current (Figure 2.3B). This suggests that a coherent water mass with lower density than the surrounding seawater lofted above the moving turbidity current. In the January event, anomalously less dense water masses were observed, ~ 1hr after the flow had completely dissipated, and occurred at heights significantly greater than the turbidity current thickness. According to SIN velocity data (Figure 2.2B) the January turbidity current extended for up to 40 m a.s.f, as it passed through the McLane Profiler. The first density anomaly measured ~50 m thick (Figure 2.4) and was detected for up to ~ 80 m a.s.f., while a second density anomaly measured ~20 m thick and was observed up to ~300 m a.s.f. This second water-mass anomaly took a further 8 hours to ascend to >285 m a.s.f. (Figure 2.3A), which could explain why the second anomaly is significantly thinner than the first anomaly. For instance, over such time-scales, density anomalies are likely to become further stirred by internal tides in the canyon, which can reach up to 0.6 m/s. Additionally, internal tides may also explain why no anomaly was detected during the profile measured ~ 9 hours after the flow arrived (2.3A). Although the lack of a density anomaly in between profiles where anomalies were detected, may alternatively suggest that these are two separate lofting events.

2.4.2. How does observed lofting compare to previous models?

Observations of lofting in Monterey Canyon are now compared to existing models for lofting based mainly on laboratory experiments (Figure 2.6); noting that these laboratory studies have only shown how lofting occurred in flows lasting minutes and extending for less than a few metres (Figure 2.6B; Sparks et al., 1993; Hurzeler et al., 1995; Hogg et al., 1999; Gladstone and Pritchard, 2010. It is important to note that the relevance of laboratory results to real world systems relies on similarity theory, whereby artificial flows are characterised using a series of dimensionless parameters (e.g. Froude and Reynolds numbers). In a perfect scenario, all variables in laboratory models would scale exactly to full-scale observations, yet this cannot occur since Froude and Reynolds numbers vary inversely over distance (Eggenhuisen and McCaffrey, 2013). Lab flows, as a consequence will always differ hydrodynamically from full-scale flows (Graf, 1971; Yalin, 1971; Peakall et al., 1996). Flow observations from Monterey Canyon are therefore used with caution, by comparing these results to laboratory models in a qualitative sense. Another difference is that much of this past experimental work analysed lofting at the flow front, and after the flow front had come to a standstill (Figure 2.6B: Stage 2). Additionally, these observations were typically made in the form of spatial snapshots that documented the whole flow length at a single point in time (Figure 2.6B: Stages 1-3), rather than a time series from a single spatial position as measured in this study. Field data from Monterey Canyon differ in two key regards to this previous experimental data. First, a fast (m/s) through-going flow was observed, as a time-series at a single location, not a spatial snapshot at an instant in time (Figure 2.6B-C). Second, these oceanic flows terminated well beyond each measurement site (Figure 2.6C), and the furthest down-canyon position of the flow front was not observed (Figure 2.6C: Stage 3). However, as in previous work (e.g. Sparks et al., 1993), lofting is inferred once the bulk density of the turbidity current decreased, presumably due to sediment settling (Figure 2.6C). Temperature data (MS5; Figure 2.2A) indicates that warm interstitial water lofted above the flow at least ~2.5 hours after its arrival. This lofting water was 0.5ºC warmer than the ambient temperatures (detected over a 48-hour pre-event period) at that location. Thus, in keeping with previous observations (Quadfasel et

al., 1990; Kao et al., 2010), these field data also show that warm seawater carried within the turbidity current plays an important role in driving lofting.

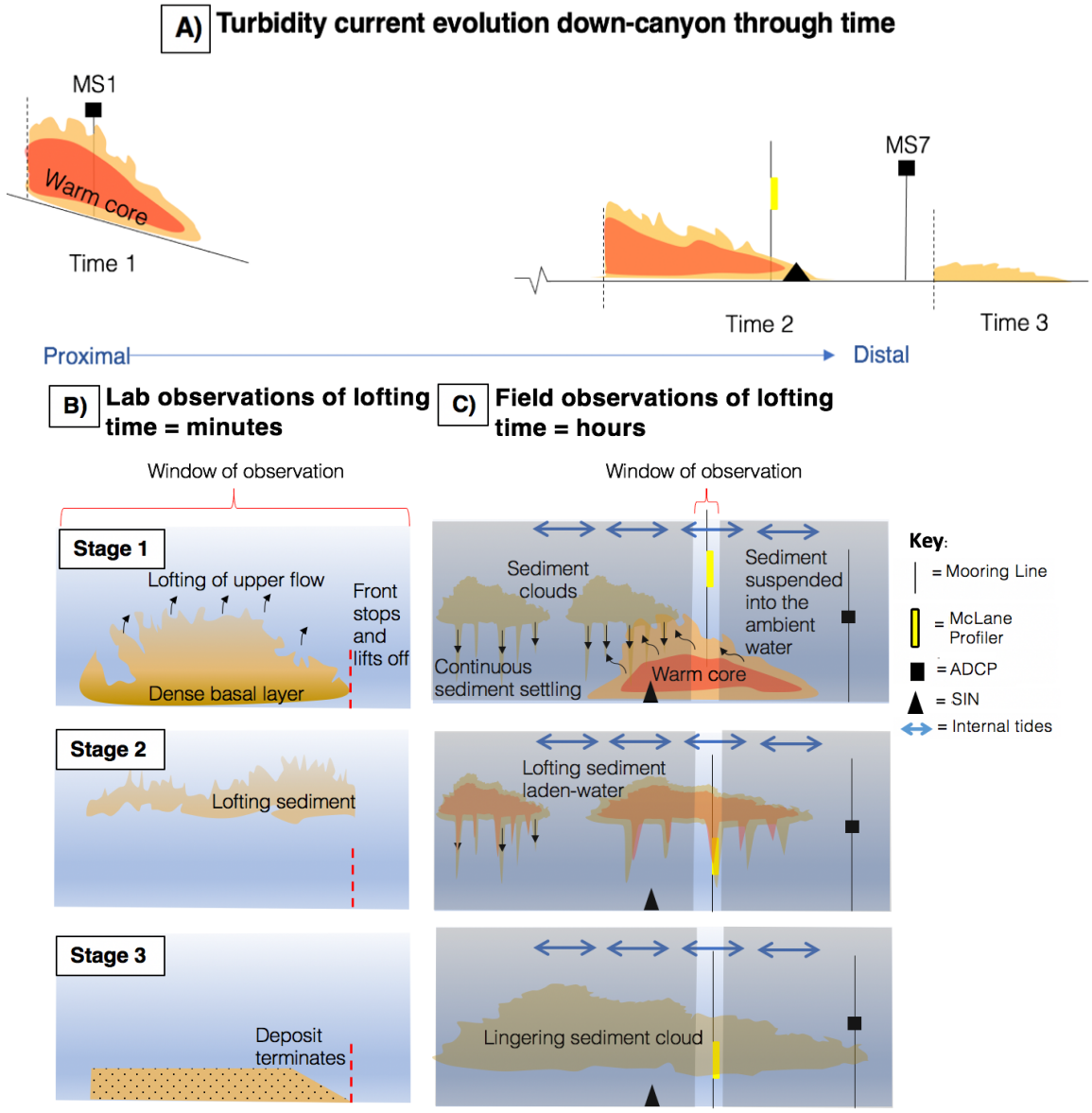

Figure 2.6. Generalised models (not to scale) showing how (**A**) turbidity currents lose heat (red–orange–yellow) when travelling through different locations over time. Eventually flows can rise vertically into the water column (lofting), and models B-C show how lofting proceeds in the lab compared to the field. **B (Stages 1-3)** Lofting seen in laboratory experiments. In these experiments, the entire turbidity current is captured in the window of observation (unshaded region), lasting over periods of minutes. **B (Stage 1)** During the initial lofting stages, the flow front stops and begins to lift off. **B (Stage 2)** Sufficient sediment has been lost at this stage for light interstitial water to ascend with the remaining suspended sediment. **B (Stage 3)** All remaining lofted sediment has settled out of suspension, and deposits terminate sharply due to lofting. **C (Stages 1-3)** Lofting observed in submarine turbidity currents in Monterey Canyon, where the flow comprises a core of warm upper canyon water. The flow front travels through the window of observation (unshaded region), and unlike the laboratory experiments, does not stop within this window. **C (Stage 1)** Initially, the upper part of the moving flow begins to loft, producing a trail of sediment clouds. **C (Stage 2)** The flow has dissipated, and the warmest parts have now lofted, carrying sediment suspended within it. **C (Stage 3)** Sediment clouds linger, and these can persist long after the turbidity current and density anomalies have dissipated.

2.4.3. How does lofting differ between the faster and slower event?

It is thought that the proportion of shallow (warmer) water retained by a lofting turbidity current might play a key role in buoyancy reversal (Quadfasel et al., 1990; Kao et al., 2010). Previous experimental works have shown that the internal temperature of a turbidity current can be determined by the amount of mixing that occurs between a flow and its surroundings (Akiyama and Stefan, 1985). In particular, faster flows entrain greater volumes of ambient seawater due to turbulence, and shear generated along the upper flow layer (Ellison and Turner, 1959; Middleton, 1993). Meanwhile, slower turbidity flows typically generate less turbulence, which can increase the likelihood that interstitial water becomes detrained from the flow into the ambient (De Rooij and Dalziel, 2001). Thus, to understand how flow velocity may affect lofting processes, the evolution of the faster January event is compared to the slower September event. Figure 2.3 indicates that the January event lofted to heights of up to ~300 m asf, for time periods of up to 14 hrs after the flow arrival. However, the September event lofted for up to 40 m asf, less than 2.5 hours after the flow arrival. One explanation for these different lofting patterns is that the January event carried a greater initial volume of less-dense seawater, which was derived from shallower sites upslope. The faster January turbidity current then somehow shielded this warmer water from mixing, despite its higher velocities. Such shielding might occur because the total volume of water within the January event exceeded that within the September event. For the January event, a larger seawater volume was evident, as all mooring stations captured greater flow thicknesses, compared to the September event (Figure 2.2; Paull et al., 2018). A second possible explanation may be that the slower September flow detrained significantly more seawater than the January event, prior to reaching the McLane profiler. In particular, the flow thickness of the September event decreased from 28 m to <10 m from MS5 to MS7, while flow speeds decelerated to <1 m/s (Figure 2.2E). In contrast, the January event retained a thickness of ~ 30 m, and speeds of up to ~2.6 m/s beyond MS7.

Overall, these results indicate a broad link between turbidity current speed, and the strength of associated lofting patterns. In particular, turbidity currents that attain sufficiently fast speeds in the upper canyon (>4 m/s; Figure 2.2A and 2.2D), seem to generate a greater density contrast relative to their lower canyon surroundings over time. Additionally, significant deceleration in the lower canyon can lead to more rapid detrainment (Figure 2.2E), thereby weakening the density contrast between a flow's interstitial water and its surroundings. Thus,

it would be reasonable to expect faster flows to loft higher into the water column, and persist for longer durations than slower events.

2.4.4. Lingering static-clouds of fine sediment

A notable feature of these Monterey Canyon flows is that clouds of static (i.e. no significant velocity above ambient values) but turbid water remained, long after temperature and salinity anomalies ceased to be recorded (Figures 2.5B, 2.6C: Stages 2-3). These persistent sediment clouds contain seawater with ambient temperatures and salinities. This type of lingering static cloud is not part of previous lofting models (Figure 2.6B), although turbid water has previously been shown to persist after turbidity currents have stopped moving down-slope (Hughes Clarke, 2016). This study is the first to correlate this type of lingering static cloud with lofting. The total durations of these lingering clouds of sediment are ~40 hours (January event; Figure 2.5B) and 12 hours (September event) following lofting. These observations initially suggest that these clouds might slowly sink due to the excess density of their sediment. Yet, they remain in suspension, suggesting that other factors likely contribute to their presence over such durations. The prolonged nature of these static sediment clouds may therefore be due to continued stirring by internal tides (0.6 m/s; Figure 2.5). Additionally, these clouds may also persist due to fine-grain sizes, which will have very slow settling velocities.

2.5. Conclusions

Previous understanding of lofting was based on theoretical models and laboratory experiments. These past studies suggested that once sufficient sediment settles from a submarine turbidity current, the remaining water might become positively buoyant and loft. Lofting is important due to the profound affect it could have on flow run-out distance and deposit shape (Gladstone and Pritchard, 2010). A number of preliminary conclusions may be drawn from analyses of this unique Monterey Canyon dataset. First, these data indicate that lofting does occur in the oceans, with seawater density anomalies persisting for up to 14 hours. Second, faster turbidity currents seemed to retain a core of warmer seawater, compared to slower flows. Flow velocity may therefore be important in determining lofting patterns. Finally, unlike past models, turbid water may then linger for 2 more days in the water column, long after temperature and salinity anomalies have dissipated, and flows have stopped moving down

canyon. These persistent static clouds may be due to stirring of fine-sediment by relatively strong (up to 80 cm/s) internal tides within the canyon, and slow settling of very fine particles. Thus, lofting in submarine turbidity currents can be very prolonged, and it can generate even more persistent near-static clouds of fine sediment.

Chapter 3: How much mixing do turbidity currents experience over time?

Abstract

Turbidity currents rival rivers in their global capacity to transport sediment. Yet, unlike rivers, there are very few direct measurements to test how turbidity currents evolve spatially. An important limitation of previous models is the uncertainty in how turbidity currents mix and entrain surrounding seawater. For instance, the earliest turbidity current models typically adopted either a one-layer or two-layer approach. The one-layer model neglects friction between the flow and the overlying fluid (Huppert and Simpson, 1980), which results in a flow that does not entrainment seawater. Consequently, turbidity currents do not become diluted over time and therefore maintain a relatively constant thickness and velocity, resulting in flows with unrealistically short run-out distances (Traer et al., 2012). Alternatively, two-layer flows entrain overlying fluid, but typically grow to unrealistic thicknesses, relative to field-scale observations (Parker et al., 1986). In particular, many previous numerical models predict that turbidity currents grow to unrealistic thicknesses. In this chapter, uniquely detailed field observations are presented, which enable the first quantitative description of seawater entrainment fluxes into full-scale oceanic turbidity currents, as they evolve down a submarine canyon. By estimating water entrainment into full-scale flows, it is then possible to test existing theoretical models for water entrainment, which are found to significantly overpredict or underpredict water entrainment. Temperature measurements are used as a proxy for mixing in these full-scale flows, and these data show that colder ambient water is entrained mainly through the nose of the flow, producing a cold flow front. Within the body of the flow, warmer temperatures occur below the height of the velocity maximum, which may indicate that the velocity maximum is a barrier to vigorous vertical mixing, as previously theorised. Overall, this chapter shows that full-scale turbidity currents are mainly entraining water through the nose of the flow, while detraining along most of the top interface. Such field observations contrast with long-standing models that emphasise water entrainment along the flow's top interface.

3.1. Introduction

Turbidity currents are capable of travelling for hundreds of kilometres. They transport globally significant volumes of sediment, organic carbon, fresh water and pollutants into the deep sea (Canals et al., 2006; Galy et al., 2007; Talling et al., 2007). Past theoretical and numerical models of turbidity currents typically diverge in behaviour after only a few hundred meters, depending on the laws used to define the entrainment of seawater and seafloor sediment (Traer et al., 2015). But flow parameters that underpin these entrainment equations are poorly known and hence need calibrating. To better predict how full-scale turbidity currents behave, this chapter seeks to improve our understanding of water entrainment into turbidity currents; by quantifying the amount of ambient seawater entrained by two flows travelling down the Monterey Canyon for tens of kilometres. Previous water entrainment models are based on small-scale laboratory flows that emphasize entrainment processes at the very front of the flow (referred to as the 'nose' herein; Sher and Woods, 2017) and along the flow's top interface (Ellison and Turner, 1959; Parker et al., 1986). When these water entrainment models are applied to full-scale conditions, they often appear to strongly over-predict the amount of water entrainment. This is because the turbidity currents rapidly reach unrealistic thicknesses that no longer fit into their submarine channels, and then quickly decelerate due to the loss of momentum that is caused by the entrainment of stationary ambient water (Traer et al., 2015; Bolla Pittaluga et al., 2018). Full-scale oceanic turbidity currents are notoriously difficult to measure in the field, although a handful of recent studies have made some advances (Paull et al., 2018; Talling et al., 2021). Previously there were no detailed measurements of water entrainment within full-scale turbidity currents to validate the existing entrainment models. Hence, predicting turbidity current transport-capacity of sediment, organic carbon, fresh water and pollutants to the deep sea is currently challenging.

Most previous studies on water entrainment into turbidity currents focussed on the top interface of flows, as it shears with the overlying ambient seawater. The vertical structure of this top interface is typically defined as a function of the bulk Richardson number (Ellison and Turner, 1959; Parker et al., 1986; Sher and Woods, 2017), which represents the ratio of the restoring buoyancy force over the velocity-induced shear force. The bulk Richardson number (Ri) is defined as:

$$Ri = \frac{RgCh}{U^2} \qquad \text{Equation 1}$$

with R being the submerged specific gravity of sediment (1.65 for quartz), g the gravitational acceleration (9.81 m/s^2), C is the depth-average volumetric sediment concentration (dimensionless), h the flow depth (m), and U the depth-averaged flow velocity (m/s). Bulk Richardson numbers can be computed for experiments, while real flows can be compared with a critical value of 0.25, where Ri < 0.25 represents an unstable flow that mixes vigorously at its upper interface.

However, it is well-known from a number of studies (Traer et al., 2015; Bolla Pittaluga et al., 2018) that the bulk Richardson number-based entrainment model of Parker et al. (1986) produces flows that entrain unrealistic amounts of seawater. Excess entrainment of ambient seawater would lead to rapid flow thickening, and in turn, abrupt deceleration, causing flows to dissipate after travelling only short distances (<500 m; Traer et al., 2015). These results are at odds with the significant lengths (10s to 100s kms) of seafloor channel systems that these flows are observed to shape (Kuenen, 1937), and the large sandy deposits found at the downstream end of these channels (Griggs and Klum, 1970; Stacey et al., 2019). Additionally, evidence from cable breaks shows turbidity currents can run out for >100s km (Heezen et al., 1962; Gavey et al., 2017; Talling et al., 2021).

Two theoretical explanations have been proposed to limit the amount of water entrainment, and thereby to extend the run-out distance of modelled turbidity currents to more realistic values. First, Bolla Pittaluga et al. (2018) proposed that at the same time as entrainment of seawater occurs into a turbidity current, seawater within the flow will also be lost (detrained) from the turbidity current, as sediment settles along the upper boundary of the flow, causing that upper boundary to move downwards. Second, Luchi et al. (2018) proposed that while mixing occurs along the top of the turbidity current, the lower part of the flow is shielded from this vigorous mixing by the velocity maximum. Shielding occurs beneath the velocity maximum, due to a decreasing velocity gradient and an increasing density gradient; resulting in suppressed turbulence. Consequently, the lower layer of turbidity currents remains dense and fast, enabling flows to run out over long distances. A new turbidity current structure emerges from this second model, where flows consist of a near-seafloor “driving layer”, which is overlain by an upper “driven layer”. Recent observations of non-sedimentary saline underflows (Dorrell et al., 2019) in the Black Sea appear to confirm such a stable stratified

layer approach, as inferred by Luchi et al. (2018). However, these saline Black Sea flows lack particles that can settle and cause detrainment of water. Such processes of water detrainment (Bolla Pittaluga et al., 2018), or shielding of the lower flow (Luchi et al., 2018), might allow turbidity currents to achieve their observed long run-out distances. But previously there were no suitable field measurements from full-scale submarine turbidity currents to test these (or other) water entrainment models.

Although past work tended to focus on mixing along the top of the turbidity current (Ellison and Turner, 1959), a small number of laboratory experiments have also shown the importance of entrainment of water at the nose of the flow (Allen, 1971; Sher and Woods, 2017). Especially in shorter surge-like flows, entrainment at the nose might dominate over the entrainment that occurs along the top interface. At the nose of turbidity currents, water entrainment can occur at two primary sites: through large billows at the top of the nose (Sher and Woods, 2015), and water entrainment from beneath the overhanging nose due to hydroplaning of the flow (Allen, 1971; Mohrig et al., 1998). In some laboratory flows, entrainment at the nose is estimated to be ~75% of the total amount of water that the nose of the flow displaces (Sher and Woods, 2015). Yet, the relative importance of entrainment at the nose of full-scale and more sustained submarine turbidity currents also remains untested.

In this chapter, rates of water entrainment into oceanic turbidity currents are calculated, using some of the most detailed measurements along the pathway of an oceanic turbidity current to date. Flows were directly measured at multiple locations along ~50 km of Monterey Canyon, offshore California (Figure 3.1A-B), during an 18-month period from October 2015 to April 2017 (See section 1.5.1 for a detailed description; Paull et al., 2018). The dataset presented in this chapter was collected during two turbidity currents on January 15th 2016, and February 3rd 2017. Both flows were relatively powerful and had velocities that exceeded 4.5 m/s, as they travelled through three moorings (called MS2, MS3 and MS5; Figure 3.1B-C). Changes in total flow volume are calculated as each event flowed down Monterey Canyon, and these different flow volumes are then used to test a number of existing water entrainment models.

3.1.1. Aims

The overall aim of this contribution is to use these novel field data from Monterey Canyon to test existing water entrainment models. First, we quantify rates of water entrainment between two pairs of moorings (MS2 to MS3, and MS3 to MS5). These field-scale entrainment estimates then allow for the testing of previous water entrainment models, which are based on the bulk Richardson number. These models consider water entrainment at the top of the flows, with (Bolla Pittaluga et al., 2018) or without (Parker et al., 1987) a detrainment correction due to settling particles. Second, temperature data recorded at each mooring is used to understand where cold ambient seawater is mixed into flows. Additionally, temperature observations can be used to provide evidence for whether a stably stratified density layer exists around the velocity maximum (Luchi et al., 2018). It is important to understand whether such a layer exists, as it would prevent colder ambient water from becoming entrained into the lower layer of the flow. Third, flow temperatures at the nose and the body are used to estimate the relative importance of water entrainment at the nose of the flow versus the body. Finally, a conceptual model is presented for the different water entrainment and detrainment fluxes, based on these full-scale turbidity current data.

3.2. Instrumentation and Data Overview

The Monterey Coordinated Canyon Experiment deployed several moorings over a 50 km stretch of the canyon axis (Figure 3.1A-C), during an 18-month period from October 2015 to April 2017. The data presented in this study were obtained from moorings MS2, MS3, and MS5 (Figure 3.1D), as these were the only locations where consecutive measurements of velocity, backscatter and temperature data were successfully recorded, during two strong flow events. At each mooring, a 300 kHz downward-looking ADCP was located 65 or 75 m above the seafloor (Figure 3.1D). These ADCPs sampled velocity and acoustic backscatter profiles at a rate of 7 ping ensembles, every 30 s. Conductivity, temperature, and depth (CTD) sensors were also fitted 9 m above the seafloor at MS2 and MS3 (Figure 3.1D). These CTDs measured seawater temperature, conductivity, and pressure, at a rate of one measurement per minute. At mooring MS5, temperature and conductivity were measured by a CT (RBRduoCT) mounted 11 m above the seafloor, with a sampling rate of one measurement every 30 seconds. Depth data has been generated from these CTD and ADCP measurements using a standard pressure conversion (UNESCO, 1983). Suspended sediment was also collected at each mooring by

Anderson-style sediment traps (Anderson, 1977), which were suspended at a height of ~10 m above the seafloor (Paull et al., 2018; Maier et al., 2019).

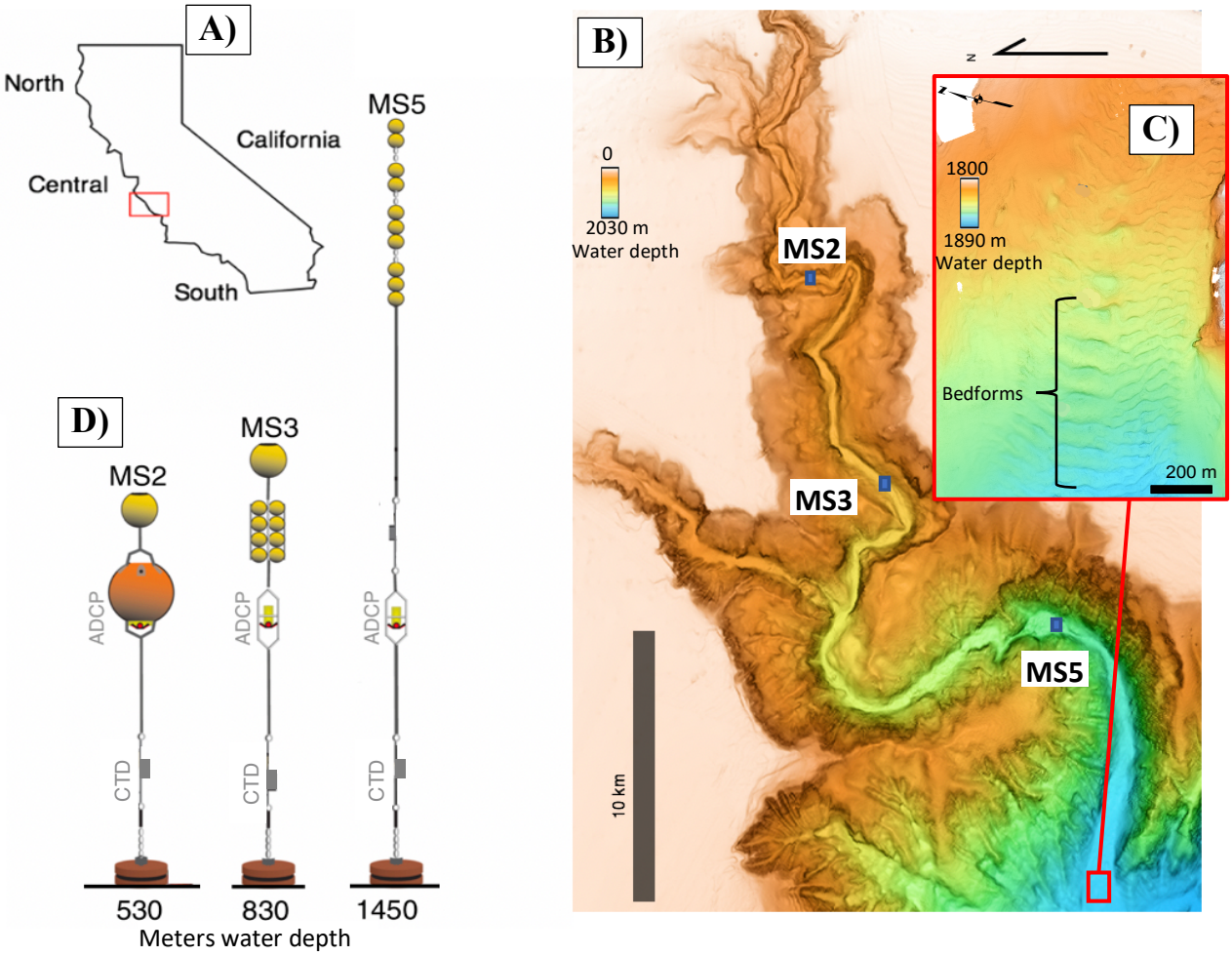

Figure 3.1. Location map and equipment used to capture field measurements within Monterey Canyon, offshore California. **A**) Map shows general location of Monterey Canyon. **B**) Bathymetry map of Monterey Canyon showing the location of moorings used in this study (blue squares; labelled MS2, MS3, MS5). Note, an abundance of bedforms (ie. undulations on the seafloor created by a combination of deposition and erosion) were present along the canyon thalweg, and these features were observed over the entire mooring array from MS1 (Paull et al., 2018) to **C**) the site of the most distal deepwater moorings. **D**) Schematic illustration (not to scale) showing the equipment used to measure flow properties at each mooring. In particular, Acoustic Doppler Current Profiler (ADCP) measured profiles of velocity and backscatter at 1 m vertical intervals, over a 65 m range from the seafloor up to the height of the instrument. Temperature data was also measured by Conductivity-temperature-and-depth sensors (CTD; grey boxes) at single heights above the seafloor of either 9 or 11 m. These instruments recorded data every 30 s.

3.3. Method

In this study, ADCP velocity and backscatter data (Figure 3.2A-L) was used to calculate water entrainment. To perform this calculation, first the volume fluxes of each flow event was calculated as the flow passed individual mooring sites. Specifically, the flow velocities measured at various heights above the seabed, were multiplied with the canyon cross sectional width at these same heights (see Figure 3.4). Second, the bulk Richardson number is estimated using the depth averages of the flow velocity, thickness, and sediment concentration. Sediment concentration estimates can be derived using ADCP-backscatter data (following Simmons et al., 2020), but this acoustic backscatter method is less reliable in the densest flow regions where acoustic signals become attenuated. To overcome this issue, both an acoustic inversion method as well as a Modified Chezy approach are used to obtain sediment concentration estimates, as outlined below. Finally, estimates of the bulk Richardson number are used to predict changes in flow volume, according to different previously proposed water entrainment models. The flow volumes predicted by these previous models are then compared to the flow volumes observed at different mooring sites along Monterey Canyon. Additionally, temperature sensors that were fitted to ADCPs and CTDs are used to trace the input of colder ambient water into the warmer turbidity currents.

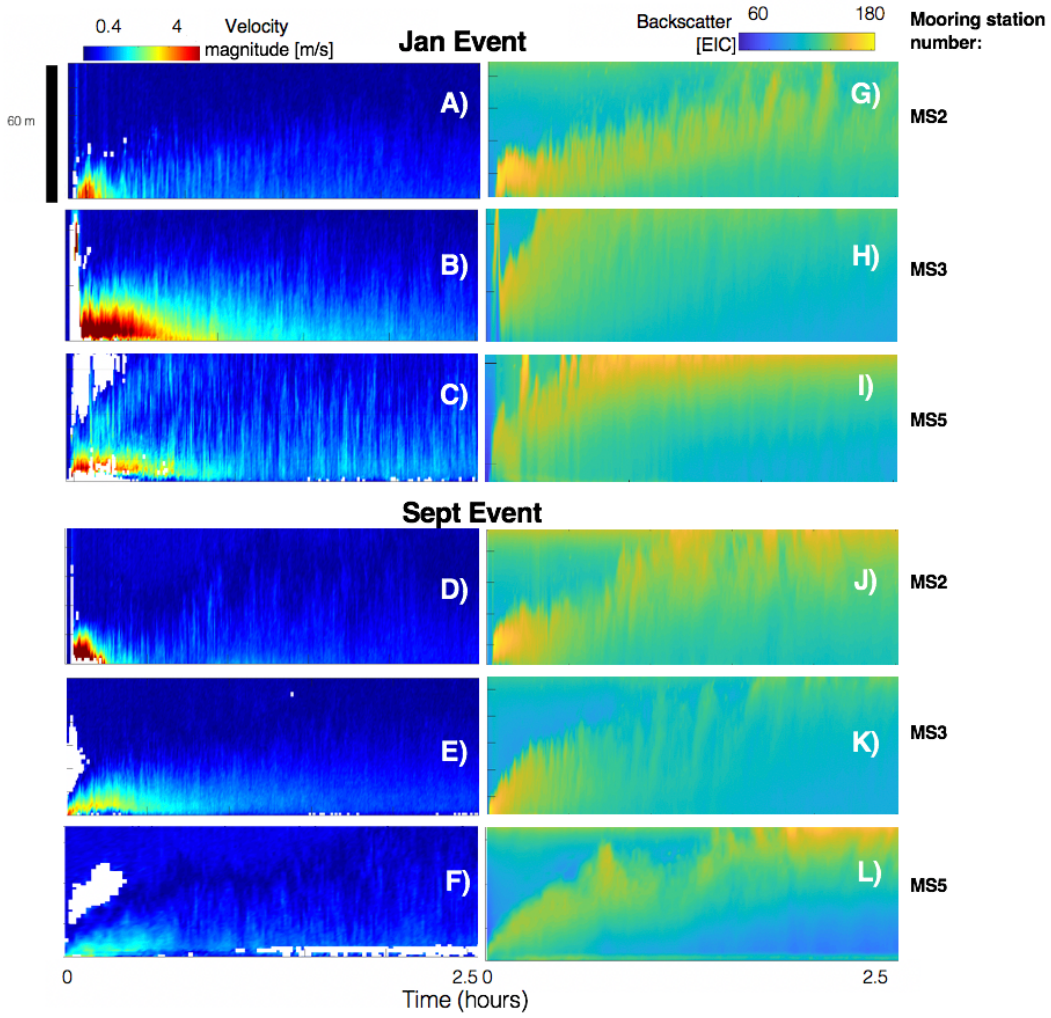

Figure 3.2. Changes in ADCP measured profiles of velocity (m/s; A-F) and backscatter (Echo Intensity Counts; G-L) through time (first 2.5 hours), as two separate turbidity current events occurred on January 15th 2016 and February 3rd 2017.

3.3.1. Definition of turbidity current events

In order to be able to model water entrainment into oceanic turbidity currents, a clear definition of the physical dimensions (i.e. size) of the flow needs to be set. In particular, it is necessary to identify the start and end of the flow over time (Figure 3.3), as well as where the top of the flow is located.

Determining the exact time when a turbidity current arrived at a mooring is relatively straightforward, as there is a sudden increase in ADCP-velocity. However, identifying the time when a turbidity current has dissipated is less clear, as strong internal tides (up to 0.6 m/s;

Figure 3.3) in Monterey Canyon make it difficult to determine the end of a turbidity current in a velocity time-series. For the purpose of this study, a turbidity current is considered to have ended when the flow velocity decreases to within two standard deviations of the background velocity. The background velocity is defined as a 31-day average of velocities measured by ADCPs prior to the arrival of each event on January 15th and February 3rd. This 31-day period excludes any other turbidity current events.

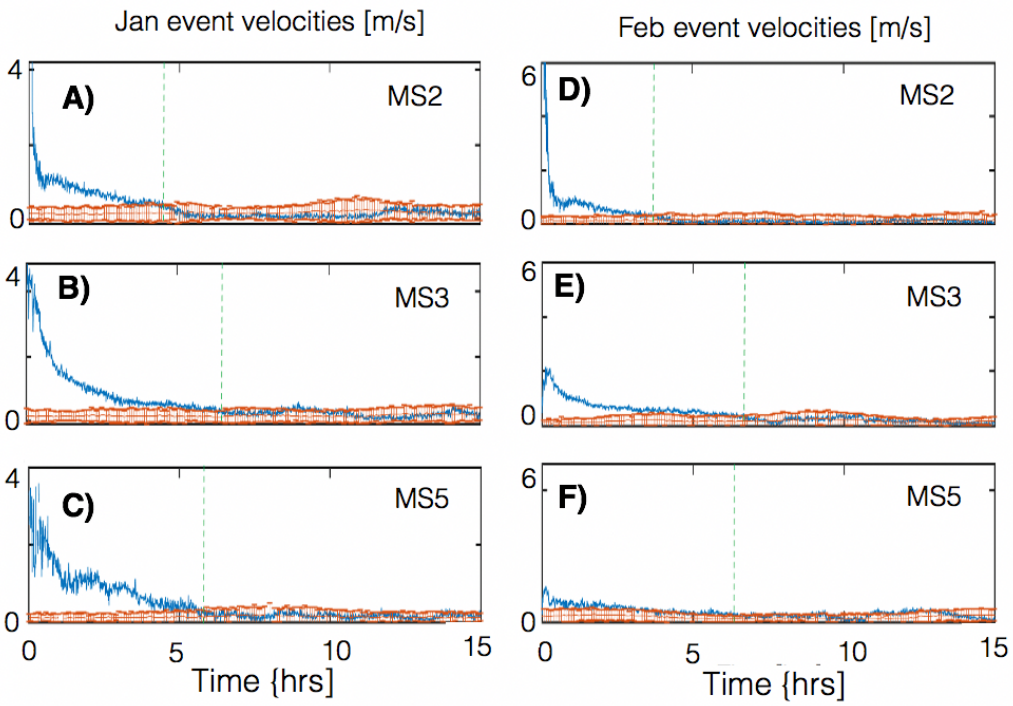

Figure 3.3. Depth-averaged velocity through time during two separate turbidity current events on 15th January 2016 and 3rd February 2017, which travelled through three mooring locations (MS2, MS3 and MS5). The onset of an event is signalled by an abrupt increase in velocity, shown at t_0. The end of each event (green dashed bars) is complicated by significant internal tidal velocities (<0.65 m/s). In this study, the end of both events is defined by the point where water speeds return to within 2 standard deviations (based on a 31-day average) of the background tidal velocities (red bars). **A-C**) 15th January 2016 event. **D-F**) 3rd February 2017 event.

The flow depth was determined following the method of Ellison and Turner (1959). This method involves integrating the velocity (u and u^2) from the seafloor up to the ADCP (Ellison and Turner, 1959), to determine the flow depth (h) as well as the depth-averaged flow velocity (U):

$$U = \frac{\int u^2\, dz}{\int u\, dz}, \quad h = \frac{\int u\, dz}{U} \qquad \text{Equation 2}$$

3.3.2. Data preparation prior to calculating water entrainment

To quantify the amount of water entrainment into a turbidity current, the data must first be prepared by:

(1) Calculating the volume of the flows as they travelled past each mooring using velocity profile data, and bathymetry data that constrain flow widths at each height in the profile.

(2) Deriving the depth-averaged flow sediment concentration using the Chezy equation.

3.3.2.1. Step 1: Quantifying flow volume

Once the physical dimensions of each flow event have been determined (as discussed previously in Section 3.3.1), it is possible to estimate the total volume of seawater that passed through each mooring station, by integrating the volume fluxes. This calculation is based on ADCP velocity profiles that were measured every 30 seconds. Each velocity profile consists of a series of vertical intervals for which there is a velocity measurement (termed bins; Figure 3.4), which are spaced 1-m apart, from the canyon floor up to the height of the ADCP (65-70 m above the canyon floor). First, gridded bathymetry data (15 m horizontal grid resolution) is used to find the width and cross-sectional area at each mooring location along the canyon. The cross-sectional area of the canyon is derived using the heights of each ADCP bin, and then multiplying the vertical dimension of each bin (1 m) by the canyon width at that corresponding height. Hence, this method considers a turbidity flow to be uniform across the width of the canyon. But in reality, turbidity flows are confined at these mooring sites and flows encounter added friction when coming into contact with the canyon sidewall. It is reasonable to expect this interaction to result in slowing and possibly thinning of a turbidity current (Akiyama and Stefan, 1988). However, it is unclear how the sediment concentration of a turbidity current would be affected from contact with the canyon wall. Nevertheless, the calculations detailed above will tend to overestimate the volumes of seawater carried by turbidity currents in Monterey Canyon. However, based on the results presented later in this chapter, this overprediction is shown to have no detrimental impact on the final conclusions made.

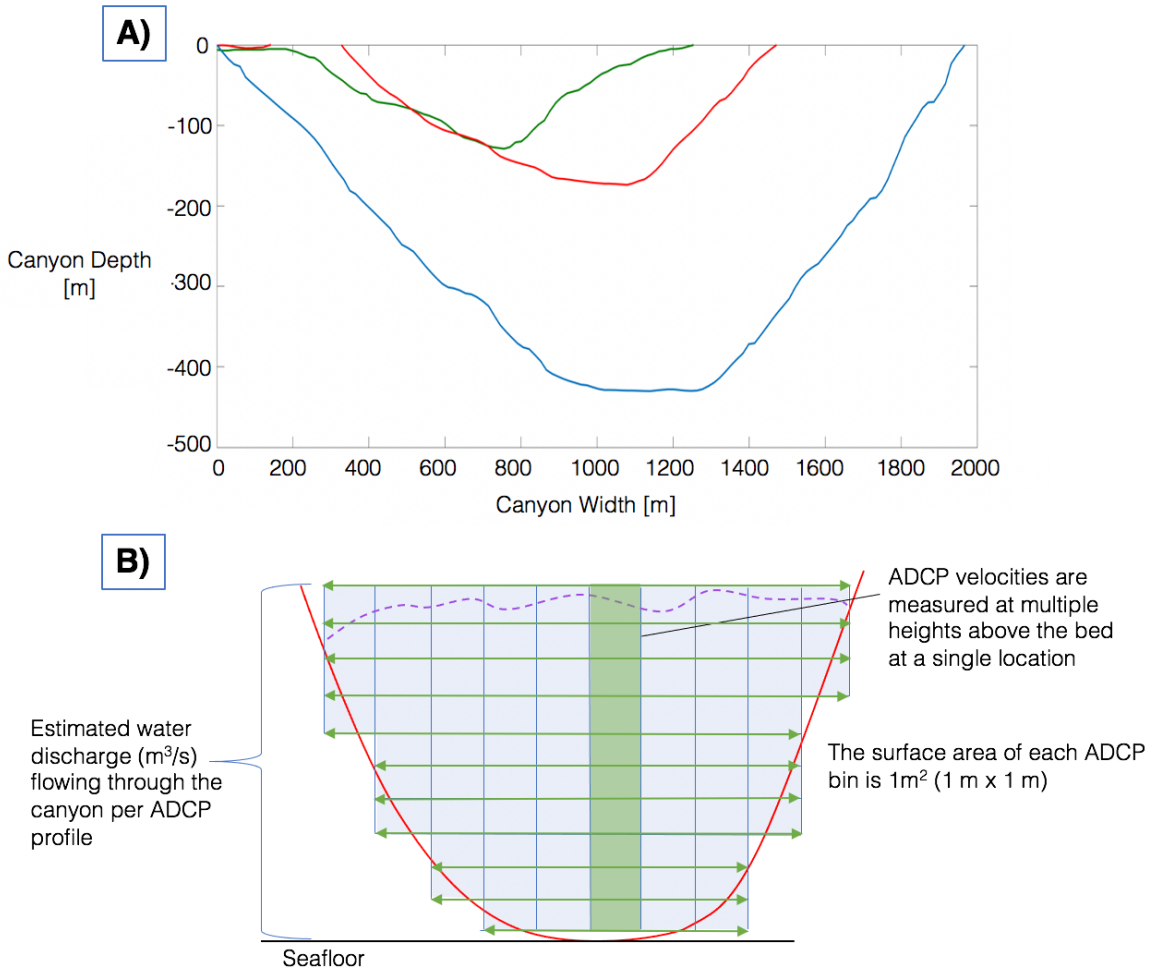

Figure 3.4. To calculate the flow discharge for oceanic turbidity currents **A)** Bathymetric survey data is first used to find the canyon cross-section at three mooring sites in Monterey Canyon (MS2 in green, MS3 in red, and MS5 in blue). At a given mooring, **B)** ADCP velocity profiles (shaded in green) are used to subdivide the canyon cross-section into a series of equally spaced measurements (bins: shaded in blue). The water discharge for each bin is given by multiplying the water speed with the surface area of the bin ($1m^2$). Thus, the total discharge in the canyon is given by the width of each row of ADCP bins (green arrows), which is equal to the canyon cross-section at a given mooring (red line). Meanwhile, the total height of each column is determined from the seabed to the top of the turbidity current (purple dashed line). Results from all bins are then summed to calculate the total water discharge within the turbidity current at this location in Monterey Canyon. Although, these water discharge values will represent an overestimate or underestimate due to the rectangular shape of the ADCP bins. For instance, when integrating close to the canyon walls (in red) or the top of the turbidity current (purple dashed line). This method then assumes that flow velocity does not vary laterally across the canyon cross-section.

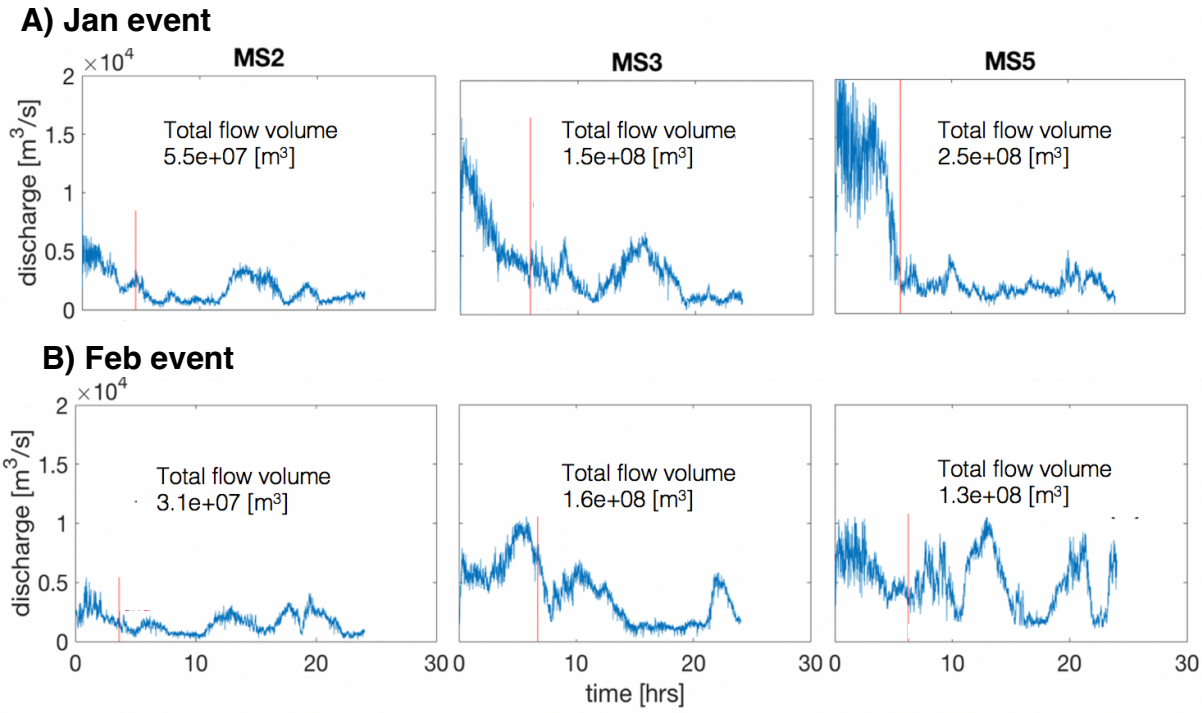

Figure 3.5. Graphs showing changes in water discharge (m^3/s) through time, for two turbidity currents on **(A)** 15th January 2016 and **(B)** 3rd February 2017, which travelled through three mooring locations (MS2, MS3, MS5). Water discharges (blue lines) are shown over a 24-hour time period. Zero hours marks the start of each turbidity current event at that mooring site. The water discharge of each event is defined according to the time period that water speeds remain above 2 standard deviations (based on a 31-day average) of the background tidal velocities (red line; see Figure 3.3 for further explanation).

3.3.2.2. Step 2: Estimating sediment concentration

To date there are very few direct measurements of sediment concentrations in turbidity currents (e.g. Xu et al., 2004; Xu et al., 2010; Xu et al., 2011; Hughes Clarke et al., 2012; Cooper et al., 2013; Wang et al., 2020), as their high sediment loads typically impede signals from sensors designed to record such measurements. To overcome this lack of data, a modified Chezy equation is used to estimate sediment concentrations. The Chezy approach was originally used to describe rivers, and assumes that for a given amount of friction generated at the bed, the ratio between the flow velocity and its driving force is constant. But turbidity currents do not typically occur under steady and uniform conditions that characterise rivers. For instance, unlike rivers, turbidity currents experience friction along their upper flow interface (Ellison and Turner, 1959; Parker et al., 1986; Konsoer, 2013). Thus, a modified Chezy approach has been adopted for turbidity currents (Ippen and Harleman, 1952; Komar, 1969; Konsoer et al., 2013), and here this modified Chezy approach is used estimate the depth-

averaged sediment concentrations (C), based on the following equations (Parker et al., 1987; Konsoer et al., 2013):

$$U^2 = \frac{1}{C_{fi}+C_{fb}} RCgHS \qquad \text{Equation 3}$$

Where U= depth averaged velocity, R is submerged density of the sediment (1.65 for quartz), g is the gravitational acceleration (9.81m/s^2), S is the seafloor gradient (~1.6º), and H is the depth averaged flow thickness, C_{fb} is the bottom friction coefficient, and the friction along the top interface (C_{fi}) of the fluid is calculated using:

$$C_{fi} = \frac{0.0075}{\sqrt{1+718Ri^{2.4}}}(1 + 0.5Ri) \qquad \text{Equation 3.1}$$

Where $Ri = \frac{RgCH}{U^2}$ and is based on the work of Parker et al., (1987; Equation 1). U and H were taken from field observations (Equation 2; Section 3.3.1). An initial bottom friction coefficient was assumed, and was later calibrated (see below). Sediment concentration (C) was then determined iteratively (Equations 1 and 3-3.1) for each 30 second measurement, to produce timeseries estimates.

It is then important to note that sediment concentration estimates generated by the Chezy approach depend on the bottom friction (Cf_b), which is unknown. To determine the bottom friction, Chezy sediment concentration estimates are compared with sediment concentrations derived from the ADCP backscatter in the dilute regions of the flow (Simmons et al., 2020; C<0.05%; Figure 3.6). Since ADCP backscatter data is less reliable in the dense flow regions, where the acoustic energy typically does not penetrate the entire flow, down to the seafloor; a bottom friction coefficient of 0.004 represents the best fit of the Chezy sediment concentration estimates with the acoustic inversion sediment concentration estimates (Figure 3.6). This friction value also agrees with previous work, which estimates that the bottom friction coefficient is between 0.002-0.005 for turbidity currents within submarine canyons (Konsoer et al., 2013).

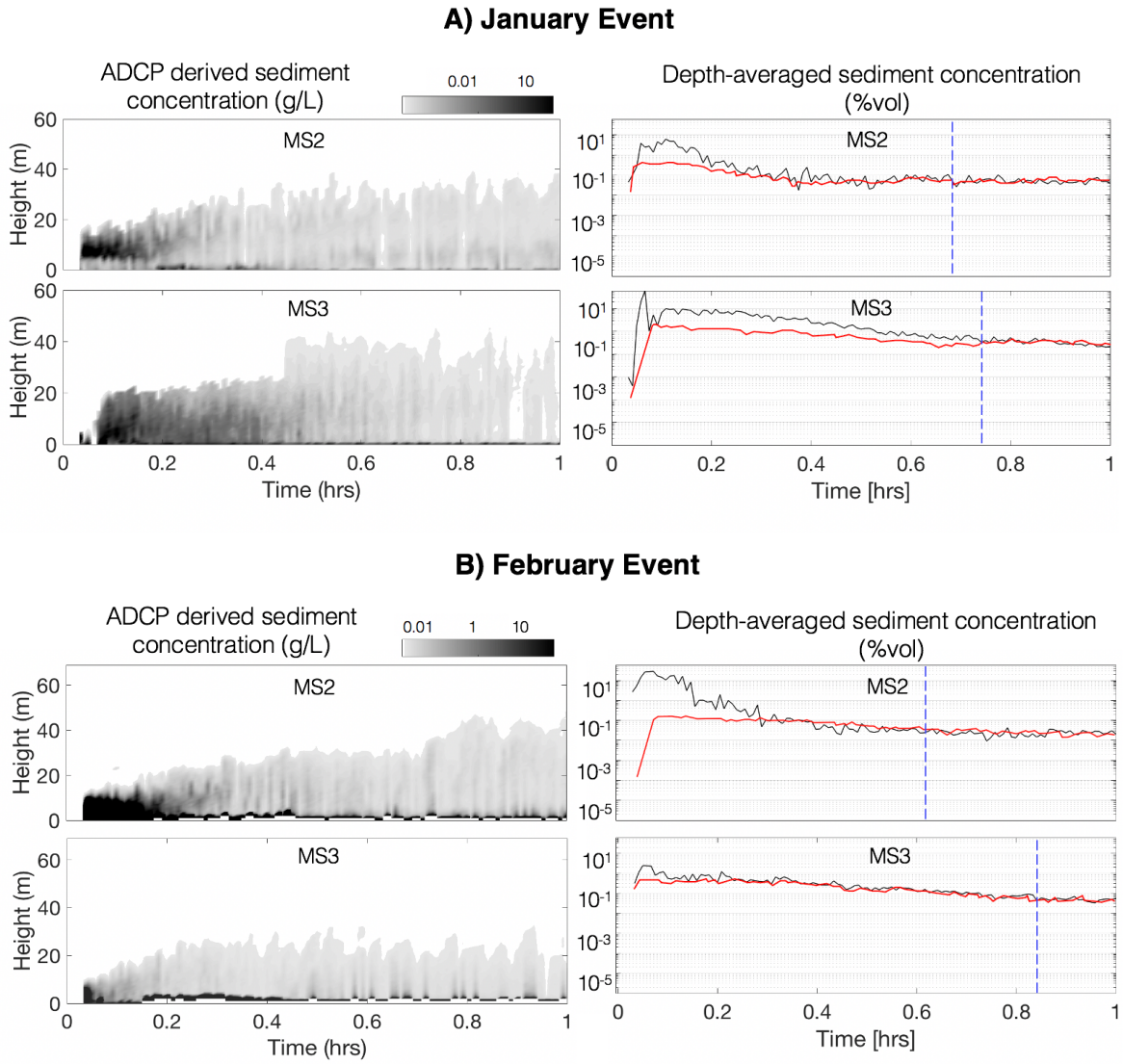

Figure 3.6. Chezy sediment concentrations estimates (right panel: black lines) are compared with sediment concentrations derived from timeseries ADCP backscatter (right panel: red lines; left panel: in greyscale; Simmon et al., 2020). This was during the first hour of two individual turbidity current events, on **A)** the 15th January 2016 and **B)** the 3rd February 2017. Since the Chezy approach (Equation 3) depends on the seafloor roughness (Cf_b), which is unknown. ADCP derived sediment data (left panels: greyscale) is instead used to calculate the roughness parameter (Cf_b), for the dilute parts of the flow (<0.05%). A value for bottom friction (0.004) is found when the Chezy sediment concentration estimates (right panels: black lines) match the sediment concentrations derived from ADCP backscatter (right panels: blue dashed lines), in these less dense regions where the acoustic signal successfully penetrates the entire flow.

However, this modified Chezy approach does not take into account the erosion from turbidity currents, which can also alter the seafloor roughness. Additionally, the head of a turbidity current is thought to be more erosive, in comparison to the trailing body and tail regions (Allen, 1971; Azpiroz-Zabala et al., 2017). Consequently, the body and tail regions that follow behind the head may experience increased seafloor roughness, compared to the flow front. To calculate depth-averaged estimates for sediment concentration using the Chezy

approach; the roughness of the canyon floor is assumed to remain constant over the entire duration of the flow. Support for this assumption is based upon evidence of bedforms, a key element of canyon floor roughness (Sequeiros et al., 2010). Repeat mapping surveys show that bedforms are present in the canyon on a sub-annual basis (Figure 3.1C; Xu et al., 2008; Paull et al., 2010). Recent analyses of mobile canyon floor sensors (Benthic Event Detectors) indicate that bedforms remained present during the passage of turbidity flows (Gwiazda et al., 2022). Additional uncertainty is introduced when using acoustically derived sediment concentrations. It is important to note that the multi-frequency (75 kHz and 300 kHz) technique of Simmons et al., (2020) uses acoustic wavelengths of sufficient size to measure fine particles suspended in the water column. But, such estimates rely on the fundamental principle that acoustic energy in the water column is backscattered by suspended sediment, which is a known function of the grain size and the sediment concentration. In this study, suspended sediment is assumed to have a grain size of 4.23 μm, and the grainsize does not vary at different heights within the flow. It is acknowledged that variations in grain size with height, or from front to back in the flow, will introduce uncertainties to such sediment concentration estimates (see Simmons et al., 2020 for the origin and full discussion of these assumptions).

3.3.3. Water entrainment calculation

The previously calculated bulk Richardson numbers are then input into two different equations, used to predict water entrainment rates. These entrainment models are differentiated by whether detrainment is present or neglected.

3.3.3.1. Quantifying water entrainment into a turbidity current (excludes detrainment)

One of the most widely used models for predicting turbidity current entrainment is the Parker et al. (1987) model:

$$v_{we\ P} = \frac{U*0.0075}{\sqrt{1+718Ri^{2.4}}} \qquad \text{Equation 4}$$

where v_{we} is the water entrainment rate per square meter at the top flow surface per second. The rate that a turbidity current entrains ambient seawater is given per unit of surface area, which can also be thought of as the velocity with which the top interface moves upwards as a result of water entrainment.

To estimate the surface area of the upper flow, the mooring-averaged canyon width at the top of the flow is multiplied with the average velocity between moorings and the time span between measurements (30 seconds). For simplicity, the upper surface area of the turbidity current, which was calculated for each profile, will be referred to as a slice herein. The entrainment volume is then estimated per profile measurement, by multiplying the top surface area of each slice along the upper surface of the turbidity current with the predicted water entrainment rate per unit of surface area. Thus, the total amount of water entrained by an event between two moorings is equal to the sum of the seawater volume entrained per slice of the flow, multiplied by the time that each slice took to travel between the two moorings. The travel time is equal to the distance between the moorings, divided by the average velocity between moorings, per slice of the flow. Overall, the total amount of seawater entrained represents a theoretical estimate, according to the model of Parker et al. (1987). To evaluate this theoretical model, these entrainment estimates are then compared with the observed increases in flow volume between each mooring (Figure 3.7).

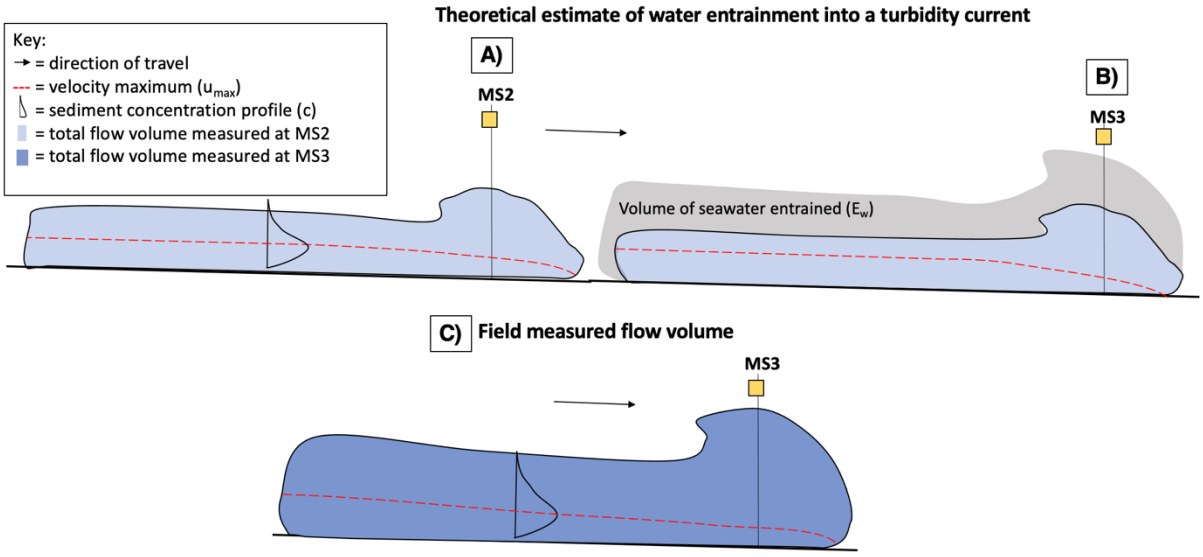

Figure 3.7. Concept illustration (not to scale) showing how theoretical predictions of water entrainment into a turbidity current compare to field-measurements. **A)** Total flow volume is quantified at mooring MS2 (See section 3.3.2.1). The total amount of water entrained (or detrained) between moorings MS2 and MS3 (i.e. E_w) is then calculated using theoretical equations 4 and 5. Input values for equations 4 and 5 come from measurements at MS2, which also utilise the distance and time travelled by the turbidity current between moorings MS2 and MS3. **B)** The total amount of water entrained and detrained between moorings MS2 and MS3 (i.e. E_w) is then added to the observed total flow volume at MS2, to predict the total flow volume at MS3. **C)** At MS3, ADCP field-data is used to calculate the total flow volume (dark blue), which is then compared to the discharge predicted (light blue area + grey area in part B).

3.3.3.2. Quantifying water entrainment into a turbidity current (includes detrainment)

Following a similar method as explained above, a second entrainment model is tested that is based upon a modified equation by Bolla Pittaluga et al. (2018):

$$v_{we\ B} = \frac{U*0.0075}{\sqrt{1+718Ri^{2.4}}} - v_s \qquad \text{Equation 5}$$

Where v_s is the terminal velocity of the d_{50} grain size within that 30-second slice of the flow.

The approach of Bolla Pittaluga et al. (2018) requires a representative sediment settling velocity (v_s). The grain size distribution within these flows is inferred from sediment trap samples. At MS1 and MS2 locations, sediment traps were positioned ~10 m above the seafloor. These trap samples indicate that the flow front had a modal grain size (d_{50}) of ~300 μm. However, it is likely that these traps were dragged towards the seabed upon arrival of the flow. At the distal MS5 location, a sediment trap was suspended ~74 m above the seabed. This trap suggests that the first sediments carried by the January event had a d_{50} of ~200 μm. The sediment size of the background sedimentation in between the flows is well constrained at ~30 μm (Maier et al., 2019). For these calculations, it is assumed that the grain size within the thin (10-20 m) frontal parts of the turbidity currents is comparable to the coarse fraction in the sediment traps. The initial terminal settling velocity is then set to 0.08 m/s, which is equivalent to a d_{50} ~300 μm grains (Maier et al., 2019). For the later parts of the flow, the terminal settling velocity is set to 0.0008 m/s, which represents a d_{50} of 30 μm. Thus, this method assumes that the grain size at the top of the flow quickly decreases from the nose to the tail of the flow. However, the rate at which grain size decreases from 300 μm to 30 μm is unknown.

Here, three different scenarios are tested to estimate the impact of the grain size variation along the top of the flow. First, an exponential trend in sediment settling velocity was modelled to rapidly decay, from coarse sediment at the nose to fine sediment over most of the flow that followed:

$$v_s = 0.0792C_1e^{-18T} + C_2 0.0008 \qquad \text{Equation 6}$$

Where T represents normalised time that varies from 0 being the start of the flow to 1 being the end of the flow (Figure 3.8). C_1 and C_2 are set to 0.0792 and 0.0008 to match the settling velocity of 0.08 m/s at the start of the flow, and a settling velocity of 0.0008 m/s at the end of the flow.

Second, an exponential settling velocity trend was modelled that decayed more slowly from coarse sediment in the nose to fine sediment in the tail:

$$v_s = C_1 e^{-3T} + C_2 \qquad \text{Equation 7}$$

Where C_1 and C_2 are set to 0.0833 and -0.0033.

Finally, a linearly decaying settling velocity trend was modelled:

$$v_s = C_1 T + C_2 \qquad \text{Equation 8}$$

Where C_1 and C_2 are set to -0.0792 and 0.0840. The three scenarios all led to broadly similar entrainment rates.

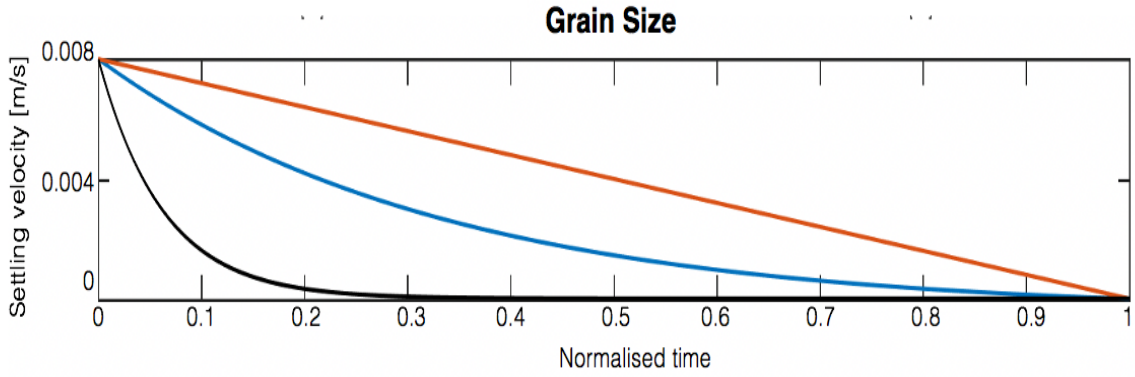

Figure 3.8. Changes in sediment grain-size and consequent settling velocity for the three different scenarios that were modelled herein. The horizontal time scale is normalised time, with 0 being the start of the turbidity current, and 1 being the end of the turbidity current. A rapid exponential decline in settling velocities (in black; Equation 6) was modelled, with settling velocities of 0.08 m/s to 0.0008 m/s being equivalent to a modal grain size (d_{50}) between 30-300 µm. A slower exponential decay in settling velocity (in blue; Equation 7) was also modelled, with settling velocities declining from 0.0833 to 0.0033 m/s. Finally, a linearly decay of settling velocity (red line; Equation 8) between 0.0792 and 0.0840 m/s was modelled, equivalent to d_{50} between 30-300 µm.

3.4. Results

3.4.1. General overview of the turbidity currents

Overall, the results from two powerful turbidity currents that occurred in January 2016 and February 2017 show that both flows ran out over 50 km (Paull et al., 2018), with peak velocities of > 4 m/s (Figures 3.2A-F; 3.9A-B) and lasted for <7 hrs (Figure 3.3). The nose of both flows was generally thin (~15 m thick; Figure 3.9C-D), dense (<0.05% sediment volume, Figure 3.9E-F) and fast (~4.5 m/s; Figures 3.2A-F and 3.9A-B; Paull et al., 2018; Wang et al., 2020). Behind these fast noses, flow thickness steadily increased to ~60 m and 50 m for the January and February events respectively (Figure 3.9C-D). The January flow accelerated to peak speeds of <5.3 m/s (Figures 3.2A-C and 3.9A) and increased in sediment volume (Figures 3.9E and 3.10C) as it flowed from MS2 to MS3. Further downstream, between the moorings MS3 and M5, the flow retained relatively fast maximum velocities (>4 m/s; Figure 3.9A), while the sediment volume decreased (Figure 3.10C).

In contrast, the February event had faster maximum velocities of 4.9 m/s during its initial stages at MS2 (Figures 3.2D-F and 3.9B), and also slightly higher sediment volume (0.43 Mt; Figure 3.10D) than the January event (0.22 Mt; Figure 3.10C). The February flow then rapidly decelerated as it travelled towards MS3, where peak velocities were <2.8 m/s (Figures 3.2E and 3.9B), and the sediment volume was significantly less (0.17 Mt; Figure 3.9D) than that of the January event (3.34 Mt; Figure 3.9C). At the furthest downstream mooring MS5, the January event retained speeds > 1 m/s (Figures 3.2C and 3.9A), while the February event waned with speeds <1 m/s (Figure 3.9B). Sediment concentration data indicates that both flows were significantly diluted by MS5, as sediment volumes were estimated to be 0.82 Mt for the January event (Figure 3.10C), and 0.02 Mt (Figure 3.10D) for the February event.

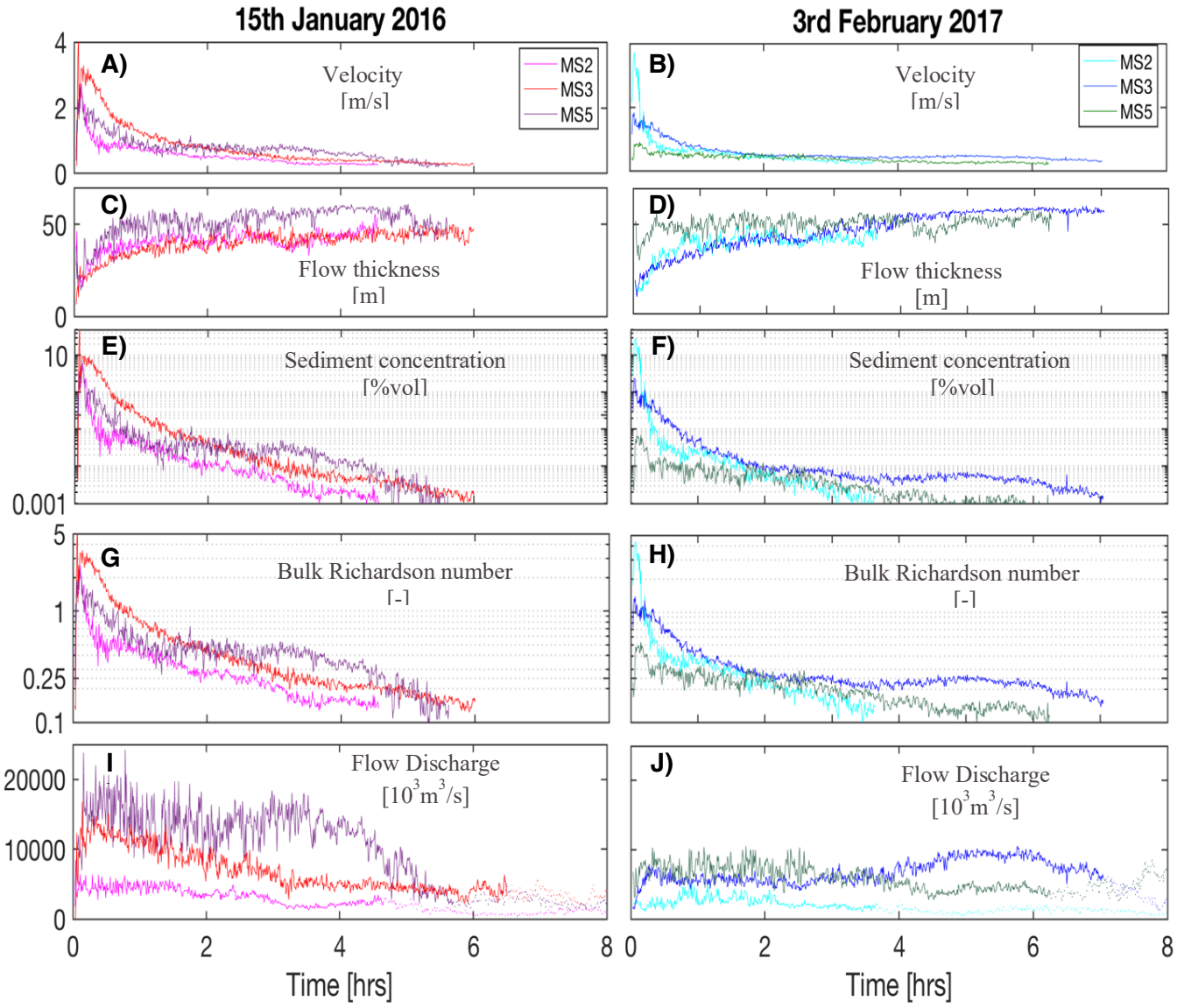

Figure 3.9. Flow properties of the 15th January 2016 and 3rd February 2017 turbidity currents, as they travelled past three different mooring sites in Monterey Canyon (MS2, MS3 and MS5; Fig. 3.1B-C). Note t=0 refers to when the flow was detected at each mooring site, which was signaled by an abrupt increase in velocity. The depth-averaged flow velocity (**A-B)** and depth-averaged flow thickness (**C-D)** were calculated using Equation 2 (discussed in Section 3.3.1). **E-F)** Depth-averaged sediment concentration derived from a modified Chezy equation (Equation 3; see Section 3.3.2.2). **G-H**) Estimates of the bulk Richardson number calculated according to Parker et al. (1987; Equation 1). **I-J)** Flow discharge (m^3/s) through the canyon cross section, at each mooring site. First, the discharge per ADCP bin was calculated using the surface area of seawater (m^2) that travelled through each ADCP bin, and multiplying these values by the average water speed (m/s) observed in each bin (as in Figure 3.4B). The total discharge is given by the sum of these results, over a total horizontal distance defined by the canyon width at each bin height, and the total height is given by the flow thickness measured per profile.

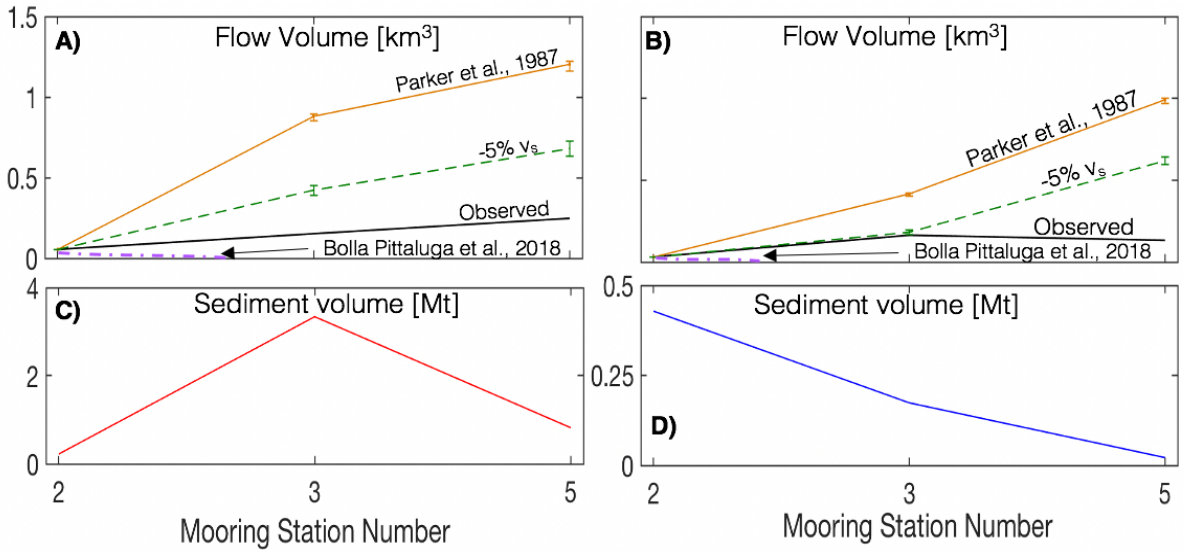

Figure 3.10. The total volume of seawater (A-B) and sediment (C-D) carried during each turbidity current at individual mooring sites, summed from the flow arrival to the end. **A-B**) The total water discharge is calculated by the integrating flow discharge over time, and finding the sum of the cumulative volume. Flow volumes were theoretically predicted without detrainment (Parker et al., 1987; yellow lines) and with detrainment (Bolla Pittaluga et al., 2018; purple dashed lines). In this study, the model of Bolla Pittaluga et al. (2018) was also modified to consider detrainment when sediment grains settled with 5% of their settling velocity (denoted by vs; green lines). Error bars show how alternative friction coefficients (Cf_b) of 0.02 and 0.05 would affect the estimated total flow volume. **C-D**) The total sediment volume is given by multiplying the individual discharge measurements with the depth averaged sediment concentration. The sum of these values is then multiplied by the time interval between measurements (30 seconds). Note the flow volume has been converted from km3 to Megatonnes (Mt), by multiplying the weight of seawater (102.5 Mt tonnes based on a density of 1025 kg/m3) with 1x108m3 (the difference in flow volume between MS2 and MS3.

3.4.2. Quantifying water entrainment and mixing parameters

Both turbidity current events entrained large amounts of ambient seawater over the first 50 km of the Monterey Canyon, as their volumes increased by a factor of 4. The January event initially tripled in volume from MS2 (0.05 km^3; Figure 3.10A) to MS3 (0.015km^3; Figure 3.10A), over a distance of ~9 km. However, despite that volume change, the first 2-3 hours of the flow are estimated to be stably stratified with bulk Richardson numbers greater than 0.25 (Figure 3.9G). Between the middle (MS3) to the distal (MS5) moorings, the current nearly doubles again in volume (0.25 km^3; Figure 3.10A), despite that most of the flow (5 hours) is characterized by stable non-mixing bulk Richardson numbers (>0.25; Figure 3.9G). The January event began at MS2 with a significantly larger total flow volume (0.05 km^3; Figure 3.10A) than the February event (0.03 km^3; Figure 3.10B). However, by the middle MS3 mooring, the flows have similar total volumes. At MS3, the January event has a total volume of 0.15 km^3, whilst the total volume of the February event was 0.16 km^3 (Figures 3.10A and

B). The initially more rapid increase in volume of the January event corresponds to a lower bulk Richardson number at moorings MS2 and MS3 (Figure 3.9G), as would be predicted by a bulk Richardson number-based mixing model. In contrast, the total flow volume of the February event increased more gradually at the distal MS5 mooring, despite that the bulk Richardson numbers are mostly low (<0.25; Figure 3.9H) in the final stage of this event. The seawater discharge of the February event remained almost stable between the middle and the distal mooring (Figure 3.9J), and the increase in total volume was mainly related to stretching of the flow. Both flows experienced a mostly steady and similar increase in water volume as they travelled down the canyon (Figure 3.10 A-B). However, it is important to note that there is a poor correlation between the bulk Richardson number and the amount of water that was entrained between moorings (Figure 3.11). For example, in the upper canyon (between MS2 and MS3) initially stable flow conditions (Ri<0.25) correspond to larger water entrainment rates, while later unstable flow conditions (Ri>0.25) correspond to lower water entrainment rates (Figures 3.11 and 3.9G-H).

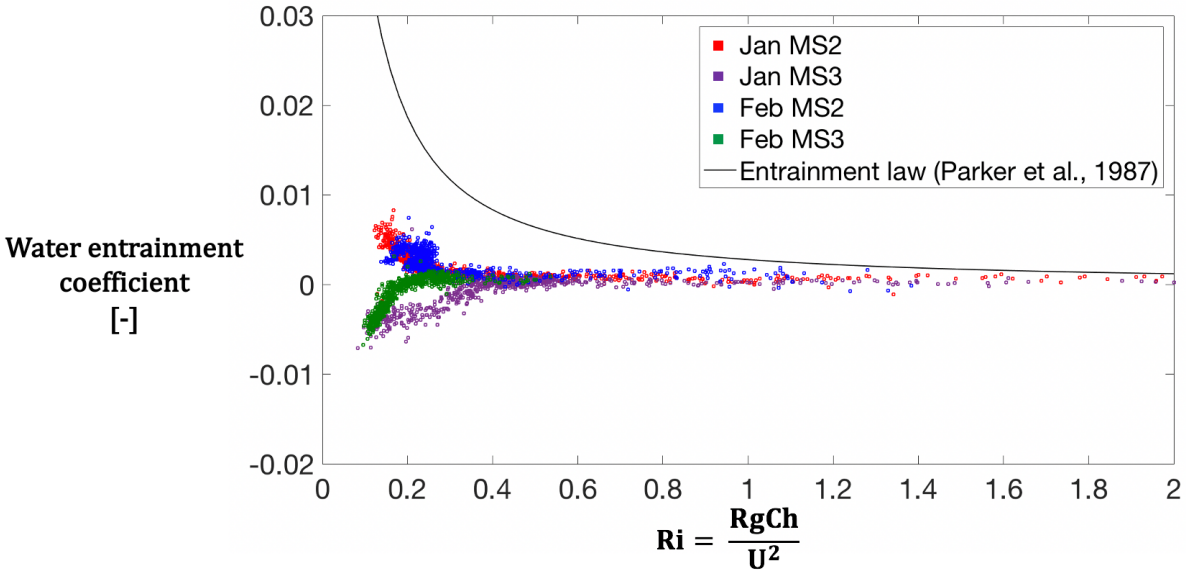

Figure 3.11. Cross plot of water entrainment (E_w; coloured squares; dimensionless) versus the Bulk Richardson number (Ri; dimensionless). Solid black line represents the water entrainment law of Parker et al., 1987 ($E_w=0.075/\sqrt{(1+718\times Ri^{2.4})}$). Data are shown for turbidity currents on 15th January 2016 (red and purple squares) and 3rd February 2017 (blue and green squares), at mooring sites MS2, MS3, and MS5. For these field-measured flows, the water entrainment coefficient is given by the ratio between the velocity with which the upper surface area of the flow expands due to water entrainment ($\frac{m^3/s}{m^2} = m/s$), divided by the average flow velocity (m/s).

3.4.3. Tracing water entrainment using temperature

Water temperature observations also provide important insights into mixing processes. Figure 3.12 shows the temperature variation over 24 hours following the start of the flow. These data were recorded at two heights above the seabed. As the turbidity currents travel into deeper and colder water, the flows themselves also rapidly become colder. Importantly, the downstream moorings consistently detected colder internal temperatures during both turbidity current events, compared to the temperatures recorded at the furthest upstream mooring (Figures 3.1B and 3.12A). This implies that all parts of the turbidity current are affected to some extent by entrainment of cold water or sediment. The warmest water (~1-2° above ambient) was consistently measured at a few hours into the flow by a sensor located below the velocity maximum. These warm temperatures suggest that the area below the velocity maximum is least affected by the entrainment of cold ambient water. In contrast, the coldest temperatures are observed consistently at the nose, and towards the top of the flow (Figure 3.12A), indicating these locations to be dominant areas of entrainment. To compare these temperature trends, flow temperatures have been normalised and plotted against the relative height of the velocity maximum, as shown in Figure 3.12B. It is apparent from this figure that the average temperature increased quickly from the top of the flow towards the velocity maximum. In between the velocity maximum and the seabed, however, the temperature remains fairly constant and well above the temperature of the ambient water.

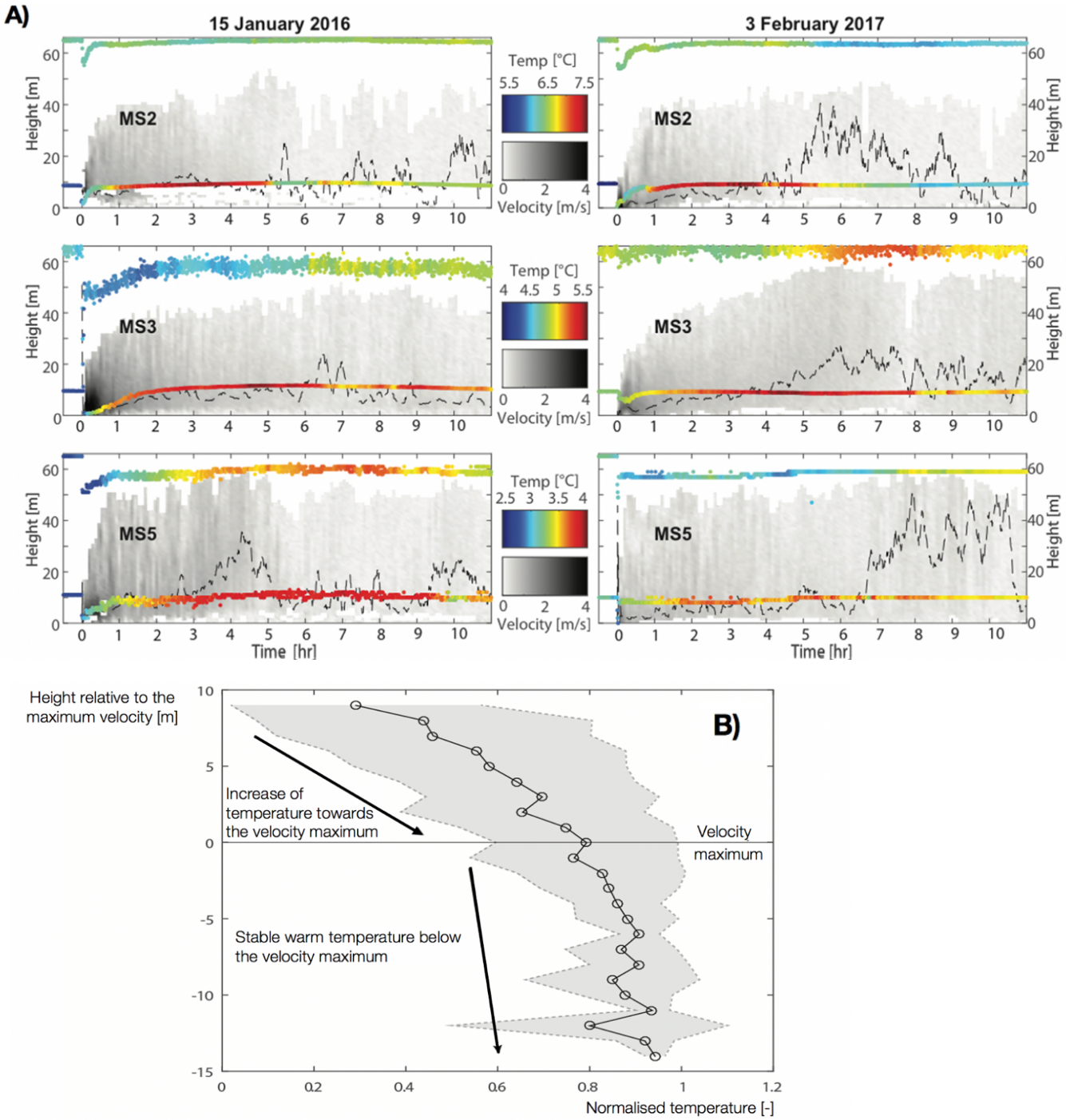

Figure 3.12. Changes in temperature and velocity measured at MS2, MS3 and MS5, during the 15th January and 3rd February 2017 events. Note that moored sensors are pulled down towards the seabed at the start of each flow. **A)** Timeseries of velocity profiles (in greyscale) from the seafloor up to the height of the ADCP (65 m), with simultaneous CTD measurements at 9 m (at MS3) or 11 m (at MS2 and MS5) above the seafloor. Measurements were recorded every 30 seconds. Warmer temperatures are shown in red, and colder temperatures decrease from yellow to green to blue. The height of the velocity maximum above the seabed is shown by the black dashed line. **B)** Graph showing how all available CTD temperature data (from time series at all three moorings) vary relative to the height of the flow's maximum velocity (i.e. 0 on y-axis). Mean temperature values (circles) are shown relative to two standard deviations (grey shading) beyond these averaged values. Temperature measurements are normalised to average ambient water temperature at that particular mooring site, such that a normalized temperature of 1° C indicates seawater that is 1° warmer than the water temperature at 24 hours before or after flow events.

Finally, these observed warmer water temperatures persisted above background conditions for over 11 hours, and this prolonged warming was detected at all mooring stations by sensors that were located at either 9 m or 11 m above the seafloor (Figures 3.1D and 3.12A). During this post-flow period, some temperature sensors detected that this warm water mass then expanded up to ~60 m above the seabed, ~ 2 hours after the flow arrival. Despite that temperature data was captured at only 2 heights above the seafloor, it is reasonable to infer that this water expanded vertically, due to evidence from backscatter data. Simultaneous backscatter measurements show that within the first 2 hours of flow arrival, the water column becomes turbid at heights >60 m (Figure 3.2G-L). This expansion of warm water typically coincides with the tail of the flow, where low bulk Richardson numbers indicate strong water entrainment (or detrainment) to be likely (Figures 3.9G-H and 3.11). Alternatively, this warm water could rise due to lofting (see Chapter 2).

3.5. Discussion

3.5.1. Entrainment through the top interface of turbidity currents

First, observations from Monterey Canyon are used to test bulk Richardson number mixing models (Equations 4 and 5), which are commonly used to predict turbidity current entrainment (Parker et al., 1987; Bolla Pittaluga et al., 2018). The results presented in this chapter show that the bulk Richardson number strongly overpredicts the volume increase for both flow events, which is consistent with earlier theoretical studies (Traer et al., 2015; Luchi et al., 2018; Bolla Pittaluga, 2018). This overprediction is thought to be caused by a lack of emphasis on detrainment processes, in particular sediment settling, as this leads to lowering the top interface of the flow (Bolla Pittaluga, 2018; Luchi et al., 2018).

Bolla Pittaluga et al. (2018) proposes to correct the entrainment model, by subtracting the terminal sediment settling velocity (v_s) from the upwards velocity generated by water entrainment (e_w; Equation 5). However, when we apply such a detrainment correction to both Monterey Canyon turbidity currents, neither flow would run-out past the second mooring, as all seawater carried within the flow becomes detrained before the flow arrives at the next mooring (Figure 3.10A-B). This entrainment model therefore predicts that turbidity currents

would travel significantly shorter distances, contrary to field-measurements and evidence from deposits (Komar, 1970; Piper et al., 1999; Talling et al., 2013).

These models raise the question of whether an intermediate scenario would work better, since a lack of detrainment results in an overprediction; while sediment settling at its terminal velocity leads to too much detrainment. Here alternative water entrainment scenarios are tested. These are based on sediment settling more slowly, and at different fractions of its terminal settling velocity (i.e. 5%, 10%, 15%, 20%) for each event. Grains that settled with 5% of their terminal settling velocity produced the closest estimates to the flow volumes observed at each mooring (Figure 3.10 A-B). However, the trend in water entrainment using these intermediate scenarios is still quite different to those observed. Overall, the results presented in this chapter suggest that models based solely on the bulk Richardson numbers and the settling velocities of the suspended sediment, are not able to explain the large-scale trend in water entrainment observed in the data.

It should be noted, however, that the bulk Richardson number represents a strong simplification of the true character of these turbidity currents (Equations 1, 3, 4, 5). In this simplification, single values of the depth averaged velocity (Figure 3.9A-B), flow thickness (Figure 3.9C-D) and sediment concentration (Figure 3.9E-F) replace the more complex and vertically varying field of velocities and sediment concentrations (Figure 3.2). Yet this simplification is necessary to provide important empirical links. In this case, between the bulk Richardson number and the upward velocity with which the top interface of turbidity currents move, due to the entrainment of ambient water (Ellison and Turner, 1959). More complicated models can be proposed to obtain a more realistic representation of the water entrainment process: 1) the flow can be divided vertically into two layers, separated by a stably stratified interface around the velocity maximum or 2) significant water entrainment can be introduced at the nose of the flow, to compensate for a potentially fully detraining top interface. First, the two-layer model is explored in more detail.

3.5.2. The role of stably stratified layers in water entrainment

Previous research has proposed that turbidity currents are capable of achieving long run-out distances because they are split into two layers: an upper driven layer where significant

water entrainment occurs, and a bottom driving layer where the sediment concentration is higher and the flow maintains its momentum (Luchi et al., 2018). Minimal mixing between these two layers has been proposed, and this is consistent with temperature data within Monterey Canyon flows (Figure 3.12). These field observations indicate that the top layer has a strong temperature gradient, while the bottom layer contains uniform higher temperatures (Figure 3.12B). This observation is therefore consistent with such a two-layer approach, as the bottom layer is only slightly affected by water entrained through the top flow. Yet, there is a further observation that seems to conflict with this two-layer model. In particular, despite that the bottom layer is the warmest, it is still cooled significantly as it travels down-canyon past consecutive mooring sites (Figures 3.10A-B and Figure 3.12A), and hence this bottom layer must also receive some of the colder ambient water.

The cooling of the bottom layer as it moves down-canyon could be caused by entrainment of cold water and/or cold sediment. First, the potential effect of cold sediment entrainment is calculated for the January turbidity current, where the temperature decreased by ~1.3 ºC between MS2 and MS3 (Figure 3.12A). Over this ~ 10 km stretch of canyon (Figure 3.1B), the flow is estimated to erode 3.1 Mt of sediment (Figure 3.10C), and also entrains ~103 Mt of ambient seawater. It is then possible to roughly quantify the extent to which the turbidity current may be cooled, if the specific heat of sediment is assumed to be 830 J/(kg*C) and 3850 J/(kg*C) in seawater. Consequently, 3.1 Mt of sediment at ~5.1 ºC (Figure 3.12A) incorporated into the initial flow volume of 51 Mt (based on a flow volume of 0.05 km^3 at MS2: Figure 3.10A) at ~7.1 ºC (Figure 3.12A), would only be able to cool the bottom layer down by ~0.02 ºC. A similar calculation is performed to determine the potential effect of ambient (cold) water entrainment for cooling the bottom layer. In detail, if 103 Mt of ~5.1 ºC ambient water (Figure 3.12A) is incorporated into the original flow volume of 51 Mt flow of ~7.1 ºC, it would lead to a temperature drop of ~1.3 ºC, which is similar to the observed temperature decrease in the canyon (from MS2 to MS3; Figure 3.12A). Based on these calculations, it is apparent that the temperature decrease between moorings is caused mainly by the entrainment of colder ambient seawater. These findings then raise the question of how cold ambient seawater becomes incorporated into the bottom flow layer. The findings in this study suggests that ambient seawater is entrained at the nose, and then travels into the lower flow layer. This conclusion is also supported by the fact that the vertical temperature gradient within the flow, shows that downward mixing of cold water from the top to the bottom layer is strongly inhibited around the velocity maximum.

3.5.3. Water entrainment at the nose

Cold temperatures measured at the very front (termed nose) and lower layer of both turbidity currents suggests that the nose region plays a key role in entraining ambient water into these flows (Figure 3.12A). Additionally, dominant water entrainment through the nose of the flow could also explain why there is a poor correlation between the estimated bulk Richardson numbers and the observed water entrainment rates (Figure 3.11). Measurements from experiments indicate that the percentage of water entrained into the nose of a turbidity current in equilibrium, can be between 60-75% of the overall volume of seawater which is displaced by the head of the turbidity current (Sher and Woods, 2017). Applying such entrainment efficiency to the flows presented herein, leads to an estimated water entrainment volume of 0.18-0.45 km^3. These estimated volumes are slightly higher, but roughly comparable, to the observed water entrainment fluxes of 0.13-0.25 km^3.

Significant entrainment of cold ambient water through the nose would explain both the strong cooling of the lower layer of the flow, and the poor correlation between bulk Richardson numbers and water entrainment volumes (Figure 3.11). Water entrainment through the nose of turbidity currents could therefore be the dominant entrainment mechanism in full-scale turbidity currents (Figure 3.13). These slightly larger theoretical estimates for water entrainment through the nose could compensate, in part, for the potential net-detrainment of water and fine-grained sediment through the top interface of the flow. A net-detraining top interface could explain the dilute stationary cloud of fine sediment observed by the acoustic instruments above the flow (Figure 3.2G-L); as the dilute fine-grained suspension may be close to neutral buoyancy once it is detrained into slightly colder ambient seawater.

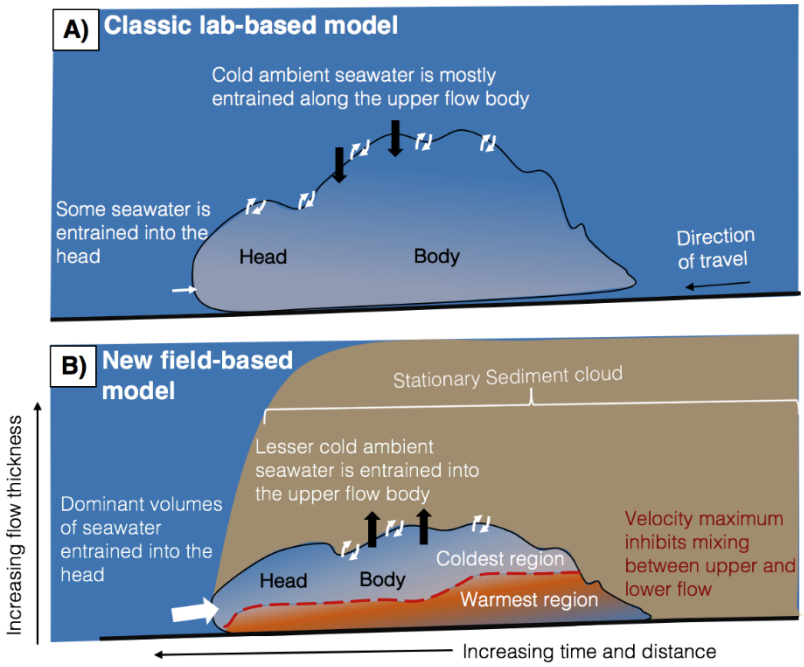

Figure 3.13. Concept illustrations (not to scale) showing how the internal temperature of a turbidity current is affected by mixing with the colder surrounding seawater. This behavior was first described by a classical model (A), however an updated model is proposed from field observations in Monterey Canyon (B). **A)** Classical model for a turbidity current in which shear mixing occurs along the flow's upper surface (paired white arrows), and a lesser amount of mixing also occurs at the flow front (single white arrow). Sediment settling can also lead to detrainment of water along the flow's upper surface (Bolla Pittaluga et al., 2018), represented by large black arrows. **B)** A new model for turbidity current mixing based on observations from Monterey Canyon. As in the classical model, shear mixing occurs along its upper surface (paired white arrows). However, the flow front also introduces significant amounts of cold surrounding seawater into the turbidity current (large white arrow). Sediment settling may then lead to water detrainment (large black arrows). But, reduced mixing at the height of the velocity maximum (red dashed line) also shields a lower region of the flow from vigorous mixing. This lower layer (labelled 'warmest region') is located below the velocity maximum, and away from the flow front. In this protected lower layer, some up-canyon water mass properties are preserved as the turbidity current travels downslope. Sediment may also be transferred from the (moving) upper part of the turbidity current into stationary surrounding seawater, creating a static (i.e. non-moving) sediment cloud that continues to linger after the turbidity current has passed.

3.5.4. What are the limitations in applying findings from Monterey Canyon turbidity currents to other submarine canyon systems?

The relevance of these results from Monterey Canyon to other submarine canyon systems, relies on whether patterns in flow behaviour exist. Within the same system turbidity currents can display broadly similar behaviour. Field data from the Monterey Canyon is one example where flows typically lasted minutes to hours, were fast (<7.1m/s; Paull et al., 2018), and

attained maximum speeds within several minutes of arrival. Over time, the depth averaged flow velocity decreased, while the flow thickness increased as seawater was entrained into the upper flow layer (Figure 3.13). This behaviour is also noted in previous studies of Monterey Canyon (Xu et al., 2004; Xu, 2010; Paull et al., 2018) and other canyons along the coast of California (Xu, 2010). However, the small number of existing field data also show that a single system can also produce two distinctly different flow types, with some flows observed to last up to 10 days in the Congo Canyon (Chapter 4; Azpiroz et al., 2017; Simmons et al., 2020). Thus, conceptual model presented in this chapter is especially relevant for sandy canyon systems. Although, it remains unclear the extent to which these results are applicable to systems with different sedimentary characteristics, and further field testing across multiple sites is needed to provide these answers (discussed in further detail in Section 5.5.1).

3.5.5. Implementing high resolution field data into theoretical studies

High-resolution field measurements provide a snapshot of a turbidity current over time and space, however the collection of such field data is often unsuccessful due to the destructive nature of turbidity currents. Thus, knowledge of turbidity currents is primarily based on laboratory experiments that are vastly smaller in scale and theoretical models that depend on simplifying assumptions (discussed in detail in Section 1.3.2; Middleton, 1966; Kneller and Buckee, 2000). Such studies generally quantify flow velocity, thickness and sediment concentration (i.e., density), and then input these parameters into dimensionless equations (i.e. Reynolds, Froude, and Richardson numbers) to estimate field-scale flow behaviour. Thus, the data presented in this chapter offers an important reference for indirect studies. For instance, field measured velocity profiles can be used to calculate the depth averaged velocity and flow thickness (See method section). ADCP data from Monterey Canyon reveals that flows had thicknesses (h) of up to <70 m thick and maximum depth averaged speeds (u) of ~0.8 to 4 m/s. Additionally, field data is also vital for validating the accuracy of existing turbidity current models. This study is a key example, comparing direct measurements of turbidity current seawater volumes against theoretical estimates of seawater entrainment into the flow, according to Parker et al., (1987). Thus, high resolution field data provides flow parameters that are essential for evaluating the accuracy of indirect studies, via the calibration and/or validation of such studies to full-scale systems.

3.6. Conclusions and wider implications

In this chapter, the most detailed observations of full-scale turbidity currents to date are used to test previous models for water entrainment (Parker et al., 1987; Bolla Pittaluga et al., 2018; Sher and Woods, 2017). First, a poor correlation is shown between the bulk Richardson number and the observed water entrainment rates, which may be due to detrainment of water across the upper boundary of the turbidity current. Water detrainment can occur due to the vertical settling of sediment, and lowering of the flow's upper boundary. A previous model of Bolla Pittaluga et al. (2018) includes a detrainment term, although this model overpredicted the net-detrainment flux as compared to field observations in Monterey Canyon (Figure 3.10A-B). Consequently, it seems likely that a combination of settling and mixing determines the net-detrainment flux. Second, temperature data shows that flows can be vertically partitioned into a driven, and a driving layer, as suggested by Luchi et al. (2018). These temperature data (Figure 3.12) also indicate that the mixing of ambient water through the nose and into the driving layer is more important than previously estimated, even for the more sustained flows studied here.

Finally, a new model is presented based on these field measurements for water entrainment into turbidity currents, which contrasts with some past models that highlight water entrainment along the top of the flow (Figure 3.13A). Instead, this study suggests that the majority of entrainment occurs through the nose of turbidity flows, and that the top interface of the flow could in fact be mainly detraining water into the surrounding ocean (Figure 3.13B). Consequently, flows are likely to entrain significant seawater volumes, growing up to a factor of 4 over their course in these examples from Monterey Canyon; and continuously shedding dilute clouds comprised of fine sediment, organics, and pollutants, that are suspended in fresher, warm and more oxygenated water. This study offers a key first step towards the framework needed to eventually develop general turbidity current models, which are capable of predicting the behaviour and transport capacity of these flows over distances beyond a few hundred meters. Insight into how these flows evolve in size as they travel from upslope to the deep ocean is also crucial to mitigating seafloor hazard risk.

Chapter 4: Can turbidity currents form different frontal structures?

Abstract

Turbidity currents move globally significant volumes of sediment through submarine canyon systems, over distances of up to several hundreds of kilometres. In addition to sediment, these flows carry significant amounts of organic carbon, nutrients, and pollutants to the deep sea, impacting deep sea ecosystems and geochemical cycles. Turbidity currents can also be powerful in nature, due to their often large transport volumes and high speeds (<19 m/s). Consequently, these flows can exert impact forces that render essential seafloor infrastructure inoperable, including seafloor cables that carry >95% of global data traffic, and oil pipelines that transport energy. Thus it is crucial to understand the structure of these flows, to better inform seafloor hazard assessments. However, to date, most understanding of turbidity currents comes from indirect (i.e. experimental and numerical) studies, rather than measuring submarine flows in action. Although a very small number of studies have measured seafloor turbidity currents in action, they have not previously analysed the nature of the flow front in detail.

This chapter presents uniquely detailed measurements from the Congo Canyon, off West Africa, where turbidity currents flowed through two mooring sites, spaced only 300 m apart. ADCP-measured timeseries of flow velocity and backscatter (a proxy for sediment concentration) profiles are inverted to distances in this study, to predict the spatial structure of the flow front. These data show that turbidity currents travelling along the same flow path developed into one of two different flow front types. Faster turbidity currents developed a distinct head, which was sometimes followed by a thinner neck, while slower flows lacked a thinner neck. This study also shows for the first time that a thin lens of seawater is pushed in front of faster turbidity flows, similar to air blasts observed during snow and rock avalanches on land.

4.1. Introduction

Turbidity currents are a mixture of seawater and sediment that are driven along the seafloor by their density excess. These flows dominate sediment transfer from the continental

shelf to the deep ocean (Middleton, 1993; Huppert, 1998; Kneller and Buckee, 2000; Sequeiros et al., 2012), since they typically originate in shallow water depths, and can travel for hundreds or sometimes thousands of kilometres (Walker, 1978; Pirmez and Imran, 2003). Consequently, turbidity currents transport globally significant volumes of sediment, which can rival or exceed that by rivers on land. Additionally, these flows carry significant amounts of organic carbon with important implications for seabed food webs and global geochemical cycles (Galy et al., 2007; Schlünz et al., 2000). In addition to their impressive volumes, turbidity currents can also reach remarkably fast speeds <19m/s (Heezen and Ewing, 1952), making them a major threat to seabed telecommunication cables that carry ~99% of global data between continents (Carter et al., 2014). The destructive nature of turbidity currents is thought to be associated with their frontal structure (Heezen and Ewing, 1952; Piper and Aksu, 1987), which is related to the type of mixing that occurs between the flow and the surrounding seawater.

4.1.1. Previous models of turbidity current fronts

Previous laboratory and theoretical modelling suggest that mixing at the front of a turbidity current can play a crucial role in the dynamics of the overall flow (Allen, 1971; Simpson and Britter, 1979; Sher and Woods, 2015; Sher and Woods, 2017). In particular, these past studies indicate that turbidity currents may have well-developed heads that mix vigorously with their surroundings. Mixing occurs at two primary locations (Figure 4.1): (1) at the top of the head where billows form when the upper flow shears with the overlying ambient seawater (Figure 4.1; Ellison and Turner, 1959); and (2) near the bottom of the head, where ambient fluid enters through a series of tunnel-like clefts (Figure 4.1; Allen, 1971; Simpson and Britter, 1979). Immediately behind the head, the flow thins to form a neck, when frontal speeds are sufficient for the head to outrun the body (Figure 4.1; Komar, 1972).

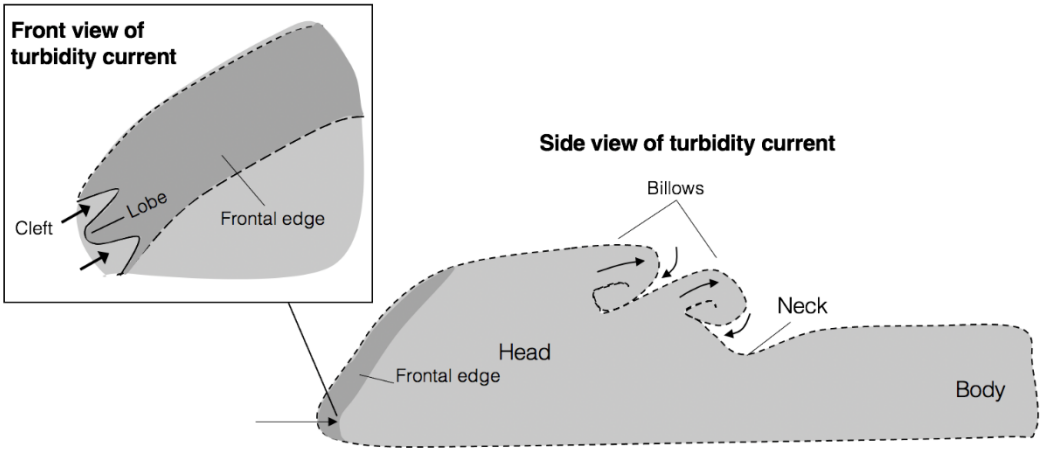

Figure 4.1. Schematic diagram (not-to-scale) of a classic laboratory turbidity current (Allen, 1971; Simpson and Britter, 1979; Simpson et al., 1997; Lowe et al., 2002). Entrainment (black arrows) of surrounding seawater into the head causes the flow to grow in volume. Previous studies have identified that mixing at the head can occur via billows along its upper surface (Simpson and Britter, 1979), or in the lower flow, via tunnel-like clefts and protruding lobes (Allen, 1971; see inset figure). This study terms the very frontal portion of the head, which first makes contact with the ambient water, the frontal edge (dark grey area).

Yet, these past models for turbidity current front structure are solely based on laboratory-scale flows that lasted between 10 seconds to a few minutes (Middleton, 1966; Hampton et al., 1972; Middleton, 1993). Consequently, important scaling issues can arise since laboratory flows are rather slow moving (<30 cm/s), when compared to typically faster seafloor events (up to 19 m/s; Heezen and Ewing, 1952) that inherently exhibit greater seafloor erosion. Additionally, laboratory flows are often created by releasing small volumes of sediment-laden fluid (Middleton, 1996; Simpson, 1982), leading to truncated (short duration) events in which the main body is faster than the head. In contrast, recent field observations suggest that the body may be left behind by a faster moving head (Azpiroz-Zabala et al., 2017).

Direct measurements of full-scale seafloor flows are now needed to test previous theoretical and lab-based models for the structure and mixing processes at turbidity current fronts (Xu, 2010; Fildani, 2017; Clare et al., 2020). However, very few direct observations from full-scale turbidity currents exist (Talling et al., 2013), as their powerful nature can irreparably damage moorings or sensors placed in their path. To-date, less than ten site studies worldwide have directly measured turbidity currents in detail, typically using moorings with Acoustic Doppler Current Profilers (ADCPs; Talling et al., 2013). However, none of these studies have analysed in detail the mixing processes or the internal structure at the flow front, which ensures fundamental questions regarding these aspects remain unanswered. This

contribution presents arguably the most detailed direct observations yet of turbidity current fronts, to understand their nature.

4.1.2. Study Area

This study is based on turbidity currents that were measured in the Congo Canyon offshore from West Africa in 2019-2020. These are the first detailed (sub-minute) ADCP-based measurements from turbidity currents at multiple sites in the deep sea (>2 km; Figure 4.2). The Congo Canyon connects directly to the Congo River, the second largest river discharge globally (Shepherd and Emery, 1973). From the river mouth, the canyon then extends for ~800 km west, terminating at ~5 km water depth and forms one of the largest submarine fans on Earth (Figure 4.2A).

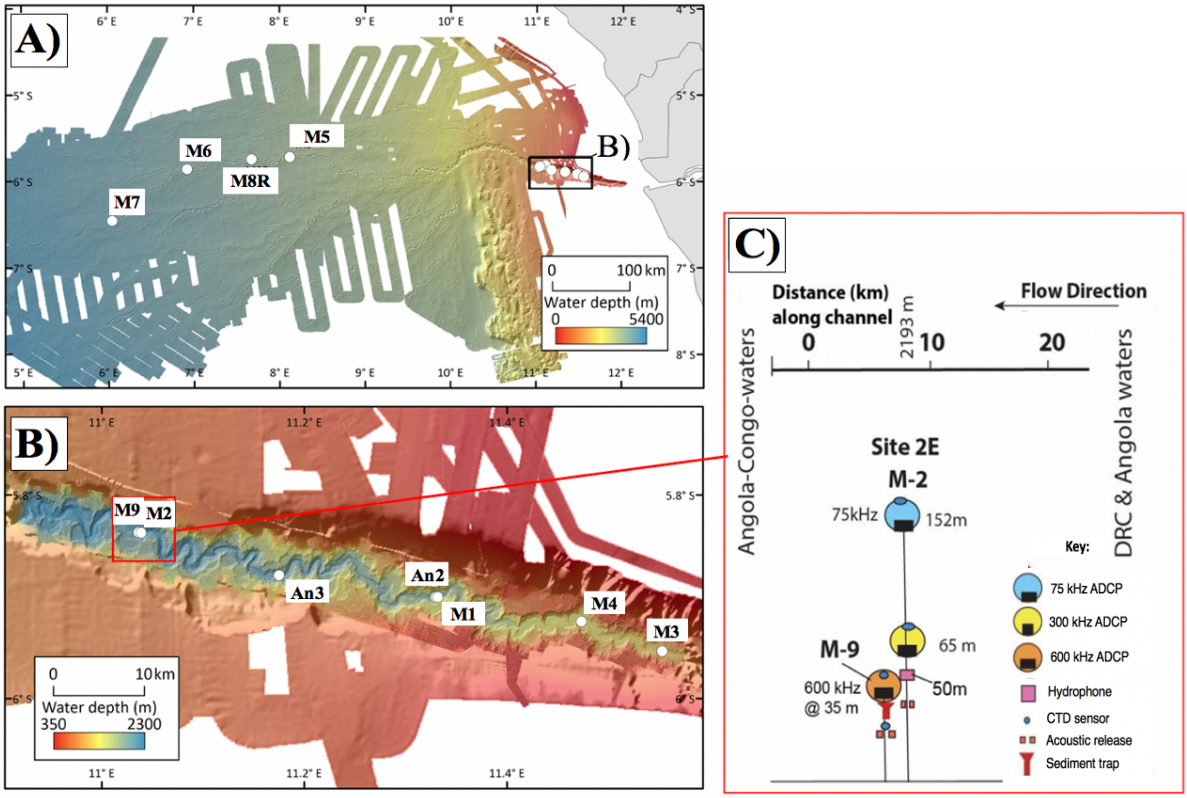

Figure 4.2. Bathymetry map showing the Congo Canyon study area. **A)** Location of all mooring stations deployed during the Congo Canyon 2019 field study (white circles). **B)** Location of upper mooring stations, with the location of moorings M9 and M2 used in this study outlined by a red box. **C)** Schematic diagram (not-to-scale) of the mooring design used in this study and the instruments fitted. The blue, yellow, and orange circles represent acoustic Doppler current profilers used to detect velocity, backscatter, roll, and pressure.

4.1.2.1. Previous Congo Canyon field work

Turbidity current activity within the Congo Canyon was first monitored using current meters that measured velocity at a single point above the seabed. These current meters were located on moorings at sites with water depths of 3.4 to 4.5 km (Khripounoff et al., 2003; Vangriesheim et al., 2009). More detailed ADCP data was collected from December 2009 to March 2010 at a water depth of ~2 km in the upper canyon (Cooper et al., 2013; Azpiroz-Zabala et al., 2017; Simmons et al., 2020), with an additional site added from January to March 2013 (Azpiroz-Zabala et al., 2017). Notably, past work has revealed that turbidity currents can persist for up to a week (Azpiroz-Zabala et al., 2017). But despite the high resolution of these more recent studies, they did not analyse the flow front in detail. This is largely because ADCPs only measure time-series of velocity and backscatter (related to sediment concentration and grain size) at a single spatial position. Thus, it is complicated to use ADCP data from a single position to understand spatial changes in flow structure, such as those occurring at the flow front.

4.1.3. Aims

The overall aim of this contribution is to provide a better understanding of the frontal structure and thus behaviour of turbidity currents. To achieve this, ADCP time series data were analysed from two mooring sites, located ~300 m apart, on the floor of the Congo Canyon (Figure 4.2). At the highest resolution mooring, time-series of ADCP data were inverted to distances, to determine how the spatial structure of the frontal part (~50 m) of turbidity currents changes with distance. These inverted field observations are then compared to results from past laboratory experiments, in order to understand how front structure affects mixing processes. This study then investigates how the head of a turbidity current affects the motion of the surrounding ambient water, to build up a more complete picture of flow front behaviour.

4.2. Method

4.2.1. Acoustic Doppler Current Profiler (ADCP) configurations

This chapter analyses ADCP data from six turbidity currents recorded in 2019, as they flowed through the Congo Canyon, offshore from West Africa (Talling et al., 2021). These

data provide an opportunity to investigate the frontal structure of turbidity currents in unprecedented detail, due to a combination of remarkably detailed spatial measurements and high temporal frequency. These flows were recorded by two moorings located ~300 m apart at a water depth of ~2200 m (Figures 4.2 and 4.3). The upstream mooring is called M2, and the downstream mooring is called M9 (Figure 4.2B). These moorings were deployed as part of an international field experiment that occurred between October 2019-January 2020 (See subsection 1.5.2 for a detailed overview; Talling et al., 2021). Both moorings used in this study were fitted with at least one downward looking ADCP (see Table 4.1 for the different configurations).

Table 4.1. Key ADCP set-up parameters and configurations used.

Mooring Station	**ADCP height above seafloor**	**Sampling rate** (time interval been measurements)	**Bin size** (vertical spacing between measurements)	**Frequency**
M2	152 m	9 s	4 m	75 kHz
M9	35 m	11 s	0.75 m	300 kHz

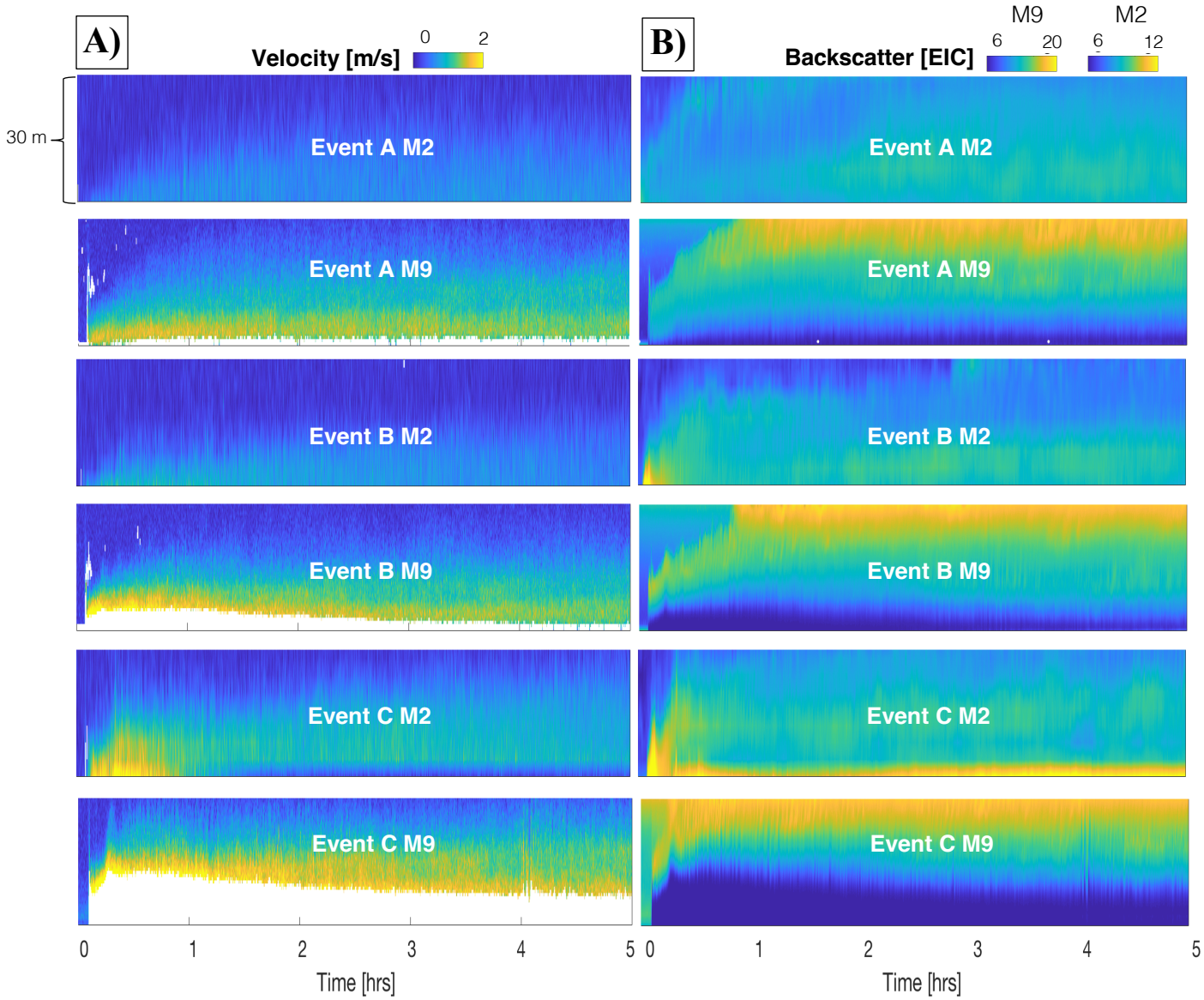

Figure 4.3. Timeseries of velocity and backscatter data for the three fastest events (A-C), these data are presented over a 30 m range above the seafloor, and were recorded by two different frequency ADCPs. Mooring M2 was fitted with a 75 kHz ADCP, whilst a 600 kHz ADCP was located on mooring M9. The time at both moorings was synchronised, providing simultaneous measurements from two moorings located ~300 m apart. **A)** Flows were first detected at the upstream 75 kHz M2 mooring, which had a lower vertical resolution (i.e. 4 m bins). The Echo Intensity Counts (EIC) ranged between 60-120 EIC, and were related to sediment concentration. **B)** Flows were then recorded at the M9 mooring, located 300 m downstream from M2. The 600 kHz ADCP at M9 collected higher resolution (i.e. 0.75 m bins) data, and backscatter ranged between 60-200 EIC.

4.2.1.2 Unresolved velocity data

ADCPs can encounter difficulty when resolving turbidity current velocities in the following circumstances: (i) regions where the flow is particularly dense so that acoustic energy

is strongly attenuated, (ii) within the first few minutes if the mooring is tilted or pulled down towards the seabed, and (iii) near to the seafloor (denoted in white; Figures 4.3A, 4.5A, 4.7, 4.8; see subsection 1.4.3 for further explanation). Velocity data are also averaged over the footprint of each ADCP beam, limiting the lateral resolution. In this study the beam footprint was either 26 m (at M9) or 110 m (at M2), which is tangent of the 20° ADCP-beam angle multiplied by a height of either 35 m (M9; Table 4.1) or 152 m (M2; Table 4.1) above the seafloor. Thus, rapid and small-scale velocity changes, which typically occur at the flow front, can go undocumented.

4.2.2. Inverting velocity and backscatter data from time-series into distance

The flow front shape of each turbidity current was predicted by inverting timeseries ADCP data collected at a single mooring location, to create a spatial snapshot of the flow front in both vertical and along-flow spatial directions. This was done by following the method of Khripounoff et al. (2012), in which ADCP data were inverted from time (in seconds) to distance (in meters), according to the following four stages (Figure 4.4):

- First, the depth-averaged flow velocity and flow height were calculated, using each vertical profile of velocity recorded by an ADCP. The calculation was made from the first time that velocities exceeded background speeds of 0.35 m/s at an upstream mooring (time = t_0), until the end of the turbidity current at the downstream mooring (M9). The depth-averaged flow height (h) and velocity (U) were then obtained by integrating the velocity (u and u^2) from the seafloor, up to the height of the ADCP (44 m; Ellison and Turner, 1959):

$$Uh = \int u \, dz$$

$$U^2h = \int u^2 \, dz$$

- The depth-averaged velocity (in m/s) for each ADCP flow profile is then multiplied by the time-period(s) between consecutive ADCP time-series measurements (i.e. 9 or 11 seconds). The product of the depth-average flow velocity and time-periods between ADCP measurements represents the lateral distance (in m) travelled between consecutive ADCP profile measurements.
- These previous steps are then repeated for each consecutive ADCP profile, such that each ADCP profile is assumed to represent a distance in the down-flow direction.

- Finally, these distances (for each consecutive ADCP profile) are summed from the time the flow arrives (t_0) until the end of the flow, in order to visualise the spatial structure of the flow front in both vertical and along-flow directions.

This method outline above essentially creates a progressive vector diagram (PVD) to estimate how these flows vary over space (Carlson et al., 2010). PVDs however implicitly assume that the velocity structure of the flow front is spatially uniform, such that the structure of the flow is not changing significantly with distance along the flow pathway. Although this assumption is likely to hold over shorter distances along the flow path, over longer distances, the flow structure may change.

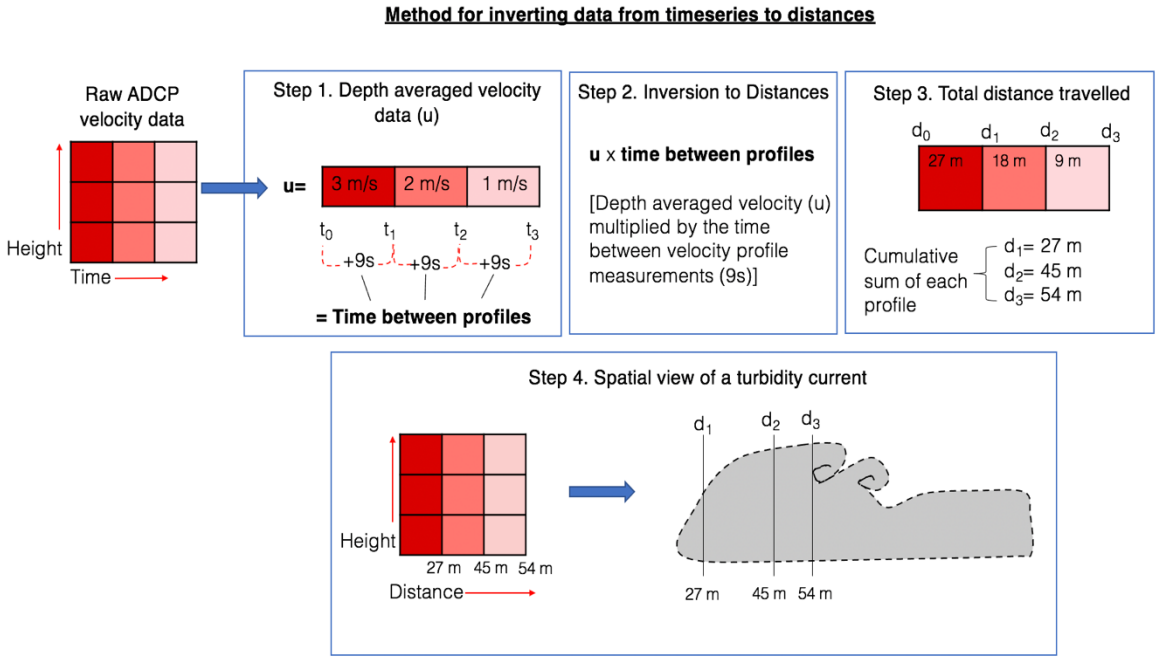

Figure 4.4. Diagram illustrating how time series velocity data obtained from an ADCP were inverted to constrain the spatial structure of the flow front. Individual velocity profiles are represented in shades of red. Flow speed data were used to calculate distance. This method is based on first finding the depth-averaged velocity for each ADCP-measured velocity profile **(Step 1)**. The depth average velocity was then multiplied by the time interval between consecutive ADCP profile measurements **(Step 2)**, giving the average distance that the flow travelled during each consecutive time interval **(Step 3)**. The cumulative sum of these distances is then used to convert the timeseries into a spatial view of the flow front **(Step 4)**.

4.3. Results

This contribution presents ADCP time-series of velocity and backscatter data, which are then inverted to distances, during three fast and three slow turbidity current events. These ADCP data were recorded as flows passed the mooring (M9) with the highest resolution

(600kHz) ADCP in the 2019 Congo Canyon deployment (Figure 4.2 C; Table 4.1). All six turbidity currents observed at mooring M9 must have already travelled at least 200 km from the mouth of the Congo River (Figure 4.2A). It is important to note that previous studies have noted the presence of internal tides in the Congo Canyon (Vangriesheim et al., 2009; Simmons et al., 2020), and similar background tidal variations were observed in this study, where these velocities were between ~0.2-0.35 m/s (Figure 4.5). For the purpose of this study, a turbidity current event is considered to have occurred only when velocities exceed 0.35 m/s.

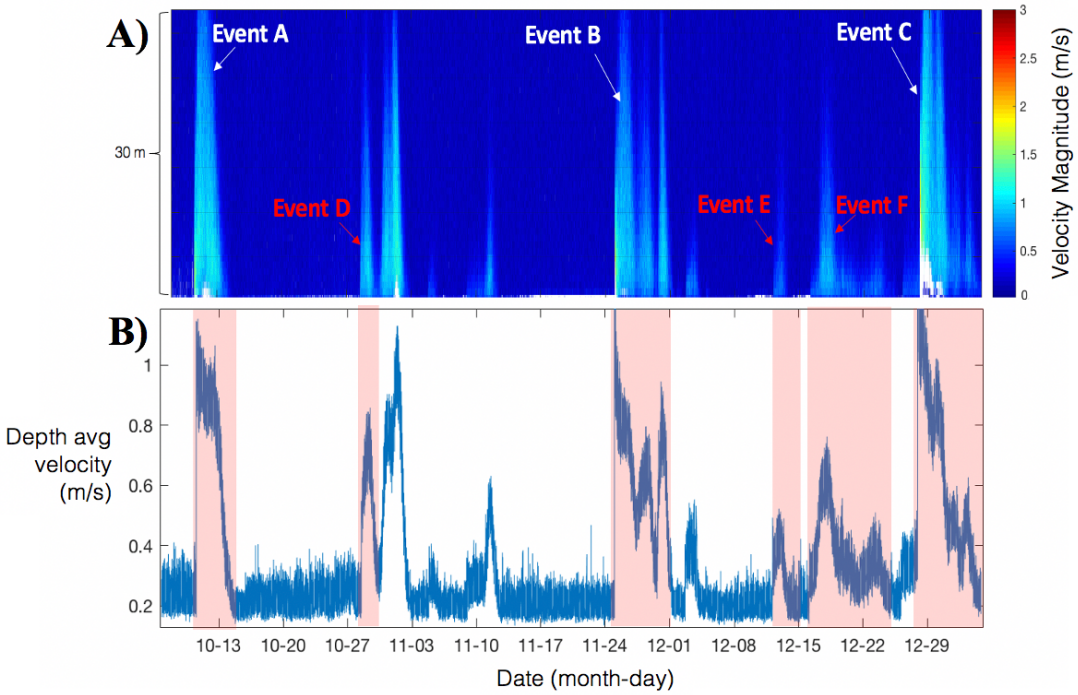

Figure 4.5. Time series of velocity data for the 600 kHz ADCP on mooring M9, showing a 30 m range above the seafloor from October to December 2019. Six turbidity current events considered in this paper are labelled A-F**. B)** Depth averaged velocities measured by the 600 kHz acoustic Doppler current profiler at mooring M9 during the same period, with the six turbidity current events indicated by pink shading. Three faster (Type 1) flows occurred on 10 October (event A), 25 November (event B), and 29 December (event C). Three slower (Type 2) flows occurred on 28 October (event D), 12 December (event E), and 16 December (event F).

In other locations, past work observed that turbidity currents can cause ADCP moorings to tilt, moving the ADCP closer to the seabed (e.g., Paull et al., 2018). For studies of flow front structure, it is thus important to determine whether the sensor depth has varied over time. This information can be verified by checking the pressure and roll sensors on the ADCP. For the 600 kHz ADCP on mooring M9, and 75 kHz ADCP on mooring M2, these pressure and roll sensors showed changes of <5 dbars and <2° respectively during all six flow events considered

here (Figure 4.6). Thus, neither of the M9 and M2 moorings was displaced vertically during the arrival of these events.

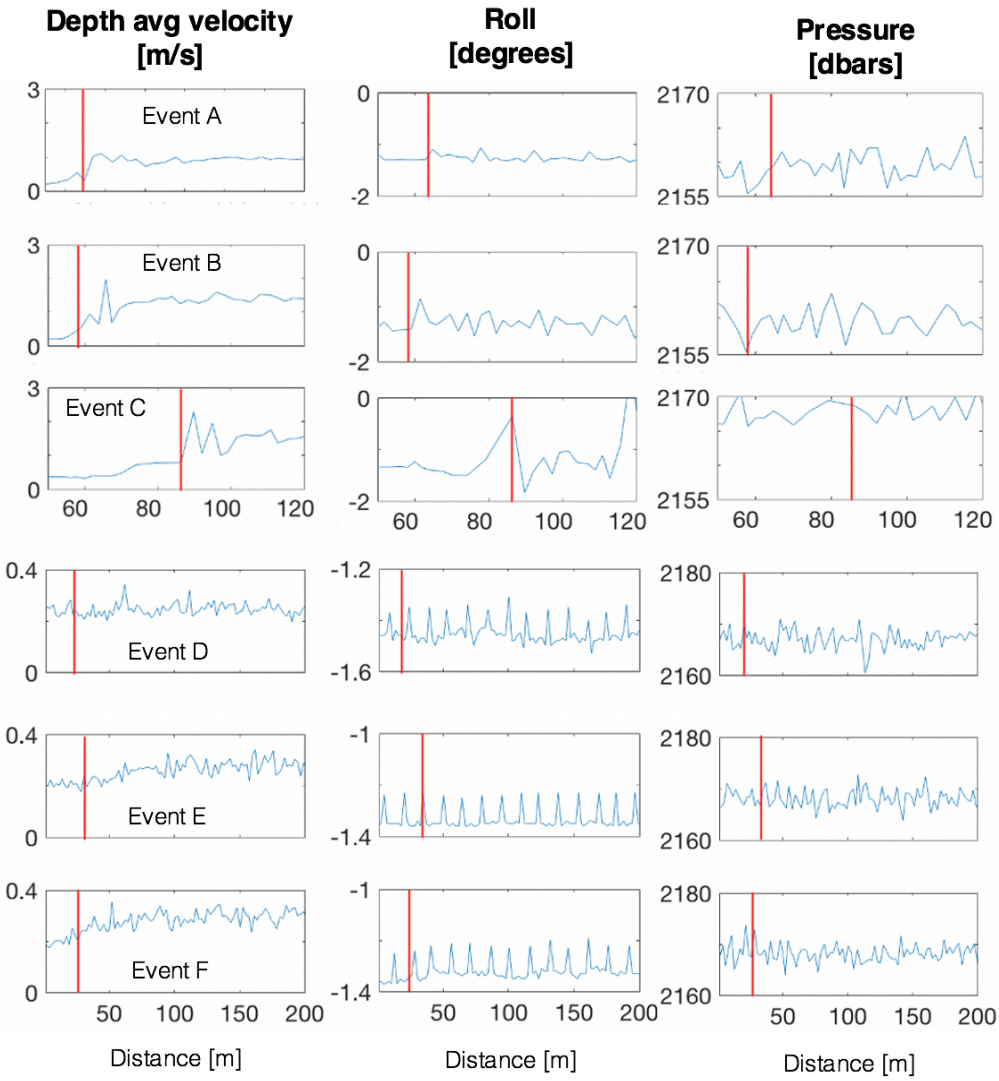

Figure 4.6. ADCP velocity (depth-averaged), roll, and pressure data from M9, which has been inverted from timeseries measurements to distances during six turbidity current events (A-C). The onset of each event is indicated by a red line.

Overall, fast (~2-4 m/s; Figure 4.7) flows had longer durations (>3 days; Figure 4.5), while the slower flows with speeds of <1.1 m/s (Figure 4.7) typically lasted ~1 day (Figure 4.5). The first faster flow occurred on 10 October 2019 (event A) and lasted for 3 days, with peak velocities of 2.1 m/s (Figure 4.7). A second faster event took place on 25 November 2019 (event B) that lasted for ~4 days (Figure 4.5), and had a peak velocity of ~3.1 m/s (Figure 4.7). Finally, the fastest flow of all was detected on 27 December (event C), and this turbidity current lasted for >5 days with maximum velocities of ~3.7 m/s (Figure 4.7). The initial slower event occurred on 28 October 2019 (event D), and lasted for 1.3 days, with peak velocities of 1.1 m/s

(Figure 4.7). Further slower flows occurred on 12 and 16 December 2019 (event E and event F, respectively; Figure 4.7), and these turbidity currents lasted for 15 hours and 1 day, respectively, with peak velocities generally <1 m/s (Figure 4.7).

4.3.1. Turbidity current frontal structure

The onset of an event was signalled by an increase in both ADCP-measured velocity and backscatter above the ambient conditions (Figure 4.7). These ambient conditions are defined by velocities that exceeded > 0.35 m/s (Figure 4.5B), and backscatter readings that typically exceeded >80 EIC (equivalent to decibels; Figure 4.7).

4.3.1.1. Faster-moving flows (Events A, B and C):

Initially, the faster-moving flow events (A and B) were associated with velocities that subtly increased (depth-averaged values of 0.4-0.8 m/s; Figure 4.6) above the speeds of the ambient tidal currents. This initial increase in velocity occurred for up to ~18 seconds before backscatter intensities exceeded their background values (Figure 4.8). This slightly faster and relatively clear seawater represented a lateral distance of ~4 to 7 m, and rapidly thickened in the vertical direction to thicknesses of between ~13-22 m (Figure 4.7). However, it is challenging to make similar observations prior to event C, as backscatter levels were anomalously high (>120 EIC; Figures 4.3 and 4.7) throughout the water column, for a significant time period before the turbidity current speeds exceeded background values.

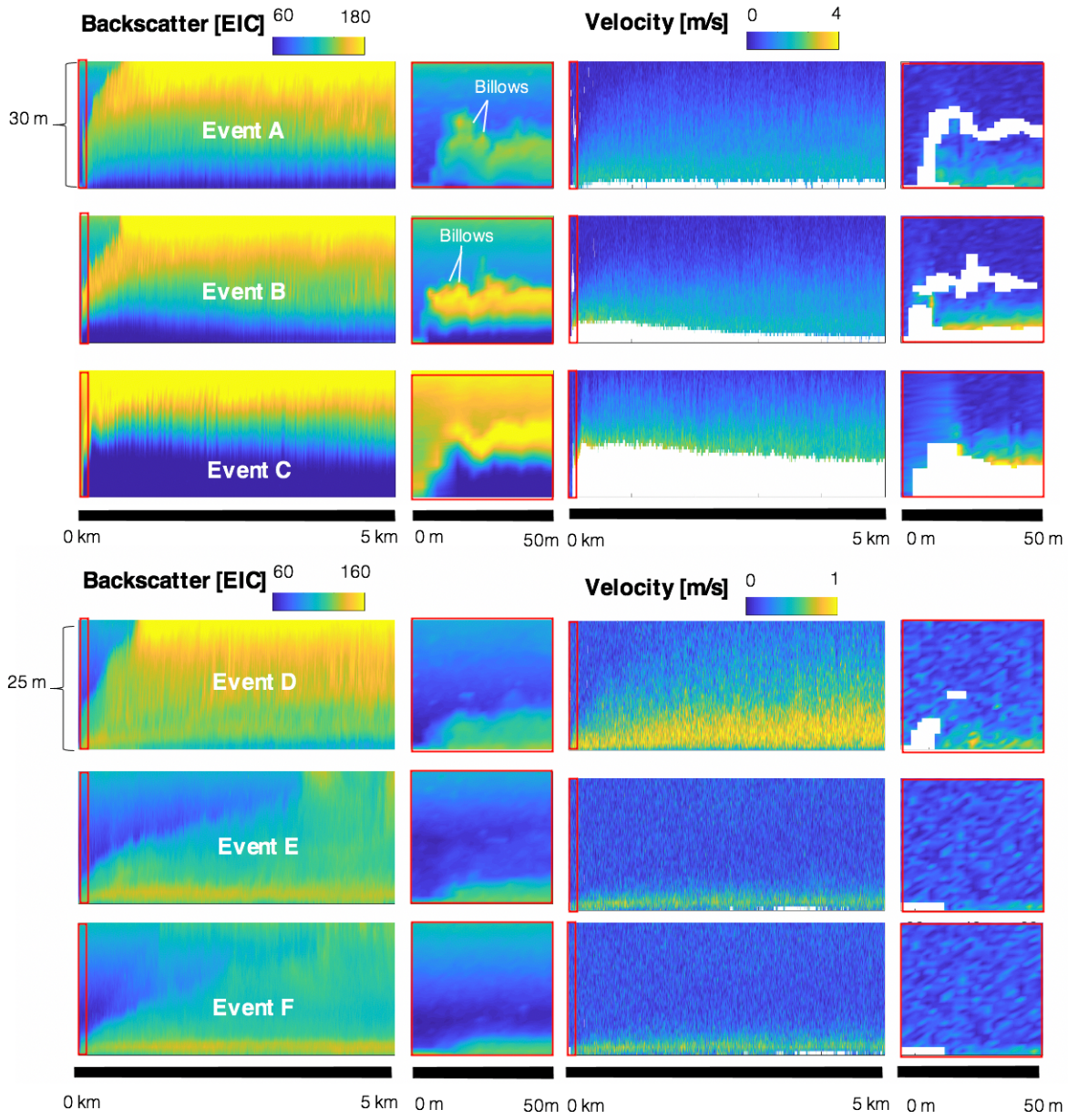

Figure 4.7. ADCP backscatter and velocity data (M9; 600 kHz) showing changes in flow thickness during the first 5 km of six individual flow events (A-C). Inset plots (in red) provide a smaller scale view of the flow front structure over a lateral distance of 50 m, and a range above the seafloor of either 30 m (events A-C) or 25 m (events D-F). Kelvin-Helmholtz billows indicate large scale mixing and can be seen during events A and B.

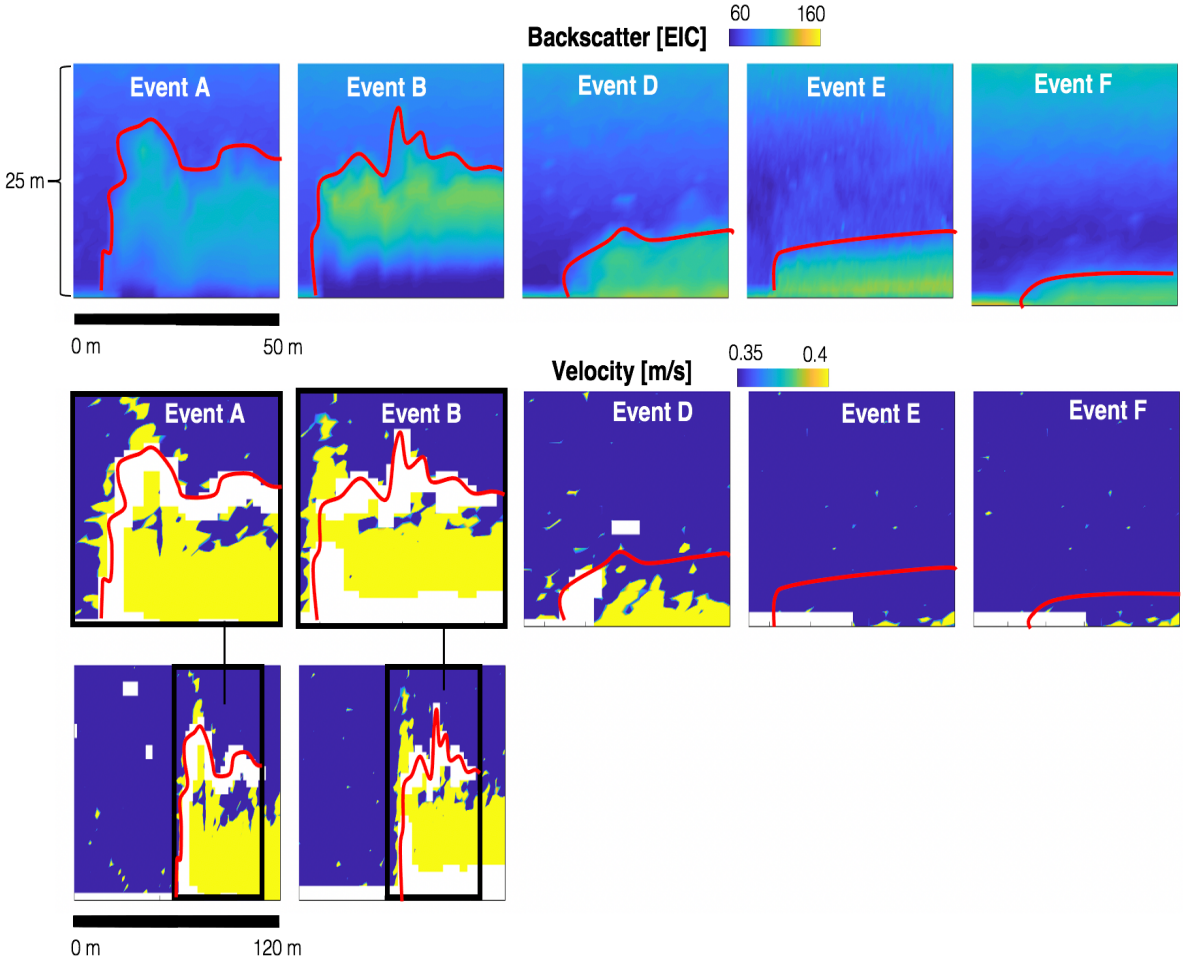

Figure 4.8. ADCP measured backscatter and velocity recorded at mooring M9 (600 kHz ADCP) during turbidity current events A, B, D, E, and F. The solid red lines represent the boundary between a turbidity current event (i.e. sediment laden water) and the surrounding seawater, interpreted from the backscatter data. Note there is an offset between the arrival times of flow fronts, defined based on velocity (red line) or backscatter. Ambient velocities range between 0.2-0.4 m/s and have now been excluded from the data (represented by dark blue shading), therefore only anomalous velocities (>0.4 m/s; in yellow) are considered turbidity current events (A, B, D, E, F). Inset plots (in black) provide a larger scale view of events A and B to show that the water column prior to a turbidity current event is generally absent of anomalously high velocities. Thus, the sediment-free water observed ahead of the turbidity current is more likely associated with the event itself.

Immediately following this slightly faster-moving clear seawater, the flow arrival (events A-C) was signalled by backscatter and velocity measurements that distinctly exceeded the ambient (Figure 4.7). In particular, the backscatter exceeded > 80 EIC for events A and B, and >120 EIC for event C. Initially, vertical flow thicknesses reached ~13-20 m, as indicated by backscatter measurements. Thus, the part of the flow that had to push aside the surrounding seawater (termed here the 'frontal edge') was ~13-20 m high in these events. The turbidity current then displayed fluctuations in its thickness, which may represent metre-scale billows;

and these spanned ~20-30 m in the along-flow direction (Figure 4.7). Following these billows, flow thicknesses decreased to resemble a neck structure, during flows A and B. After the neck, the body of the flow displayed thicknesses that remained near constant, or gradually increased over time or distance from the flow front (Figures 4.7 and 4.8). Eventually, the body of the flow became thicker than the frontal edge and head. The body may also reach a thickness greater than the height of the ADCP sensor (44 m), such that the ADCP becomes submerged within the turbidity current. Flows can also display a series of height fluctuations over hours to days (Figure 4.3). When converted from time to length scales, these relatively fast events (A-C), from start to finish, were calculated to have extended 150-250 km.

4.3.1.2. Slower-moving flows (Events D, E and F):

The slower moving events (D, E, F) were significantly thinner than the faster events (Figure 4.7). Upon arrival, these slower moving flows increased in thickness to become 3-5 m thick, over a lateral distance of ~9 m (Figures 4.7 and 4.8). The frontal edge of these flows was thus only 3-5 m thick, and there was no apparent lag in the initial increase of flow velocity and backscatter for these slower flows (Figure 4.8). The frontal edge was followed by a body with very gradual changes in thickness (billows; Figure 4.7 D,E,F) and no billows or necks formed. The body of these slower flows then gradually but steadily increased in thickness to reach values of up to 30 m (Figure 4.7). Overall, these slower flows extended for a total length of ~30 km in event E, and ~65 km in event F (Figure 4.7).

4.4. Discussion

Previous studies of turbidity currents in the Congo Canyon provide a wider view of the entire structure of turbidity currents, including their frontal part, body, and tail (Azpiroz-Zabala et al., 2017, Simmons et al., 2020). This past work is briefly summarised, to provide background for a more detailed analysis of the flow front, which is presented in the following sections. Azpiroz-Zabala et al. (2017) observed that a single flow comprised of a fast and dense frontal cell. Simmons et al. (2020) then observed the density structure of 10 individual flows, and found that flows could be grouped into two flow types. Dense long duration flows (>1 day) had either well-developed frontal zones (>2 m/s; Type 1), or weakly developed frontal zones (~1 m/s; Type 1b). Otherwise, flows were more dilute, had shorter durations (<1 day) and

lacked a frontal zone (<1 m/s; Type 2). Using ADCP data collected 2019-2020 in broadly the same location, this study now documents the first several minutes after flow arrival in detail.

4.4.1. What does the front of oceanic turbidity currents look like?

Turbidity currents in this study travelled along the same flow path, yet formed one of two different frontal structures, which seems to be linked to their overall speed (Figure 4.9). Faster moving (1.5-3 m/s) Type 1 flows rapidly thickened into a head region that was 18-30 m thick, with fluctuations in thickness representing billows (Figures 4.7 and 4.8). Subsequent flow thinning produced a neck, before the body of the flow gradually thickened again (Figures 4.7 and 4.8). In contrast, slower moving (<1 m/s) Type 2 flows were generally thinner, with a flat head only a few meters thick. These slower flows then thickened progressively over time, such that there was no distinct neck, although thickening occurred most rapidly at their very front. Type 2 flows also showed no evidence of billows, on the scale seen in the faster-moving Type 1 flows. These field observations are now compared to the turbidity current front structure seen in laboratory studies. General comparisons are made since laboratory flows can only be considered identical to field scale flows when all dimensionless numbers are the same (previously discussed in detail in Section 2.4.2).

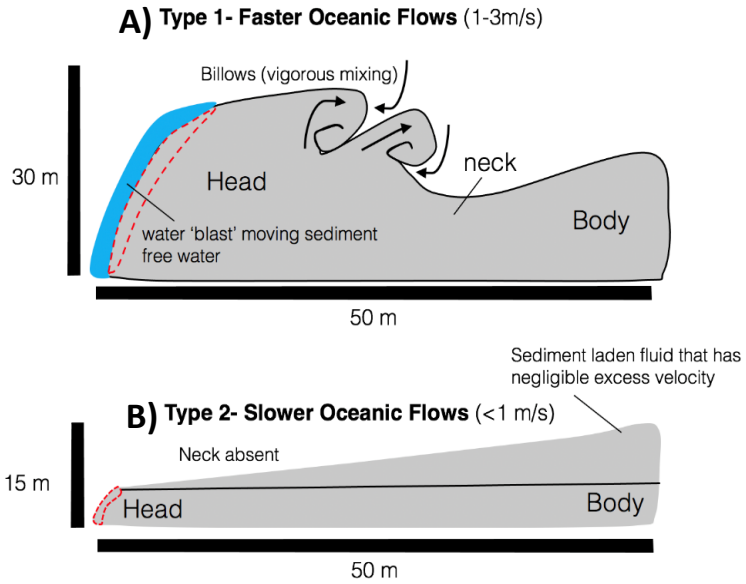

Figure 4.9. Conceptual drawing illustrating the two different flow types observed in this study. **A)** Type 1 turbidity currents were fast (>1m/s) and comprised of three separate regions (i.e. a distinct rapidly thickening head, followed by a thin neck, and a trailing body). The frontal portion of the turbidity current that first meets the ambient water is termed the frontal edge (red dashed line). The frontal edge pushes a thin wave of ambient water, which is termed a blast wave, ahead of the turbidity current (solid blue area). **B)** In contrast, Type 2 flows were slower (<1m/s) and did not show a distinct head structure. Instead this flow type thickened much more gradually over time, and the overall thickness is predominately comprised of sediment suspended above the main flow.

4.4.2. Do oceanic turbidity fronts resemble classic flow front models?

Past laboratory studies emphasised that turbidity currents can develop a distinct head structure, followed by a thinned neck, and a trailing thicker body that is initially thinner than the head (Figure 4.1; Allen, 1971; Simpson and Britter, 1979; Simpson et al., 1997; Lowe et al., 2002). This classical flow front shape most resembles Type 1 flows from the Congo Canyon. Thus, we first compare our observations of head shape to those of previous studies. We then discuss how the head shape can influence the structure of the flow that immediately follows (i.e. the neck).

4.4.2.1. Non-dimensionalised head shape

Previous work (Ippen and Harleman, 1952; Keulegan, 1957; Kulegan, 1958; Middleton, 1966) proposed that the flow speed and head shape of a turbidity current was relatively consistent over distance. In these studies, the relation between head shape and distance from the flow front was analysed by non-dimensionalising the head shape in terms of its maximum thickness (Figure 4.10). In comparison to these laboratory-scale results, our observations show that faster (>1.5 m/s) Type 1 flows in the Congo Canyon thickened more abruptly over shorter distances, and were unstable, given that billows formed at the back of the head. The faster rate at which the oceanic flows thickened is likely caused by greater mixing with the ambient fluid (Ellison and Turner, 1959; Allen, 1971; Parker et al., 1987) during oceanic flows. Therefore, we now review evidence for large scale mixing, to better understand why these two different head structures form (Figure 4.9).

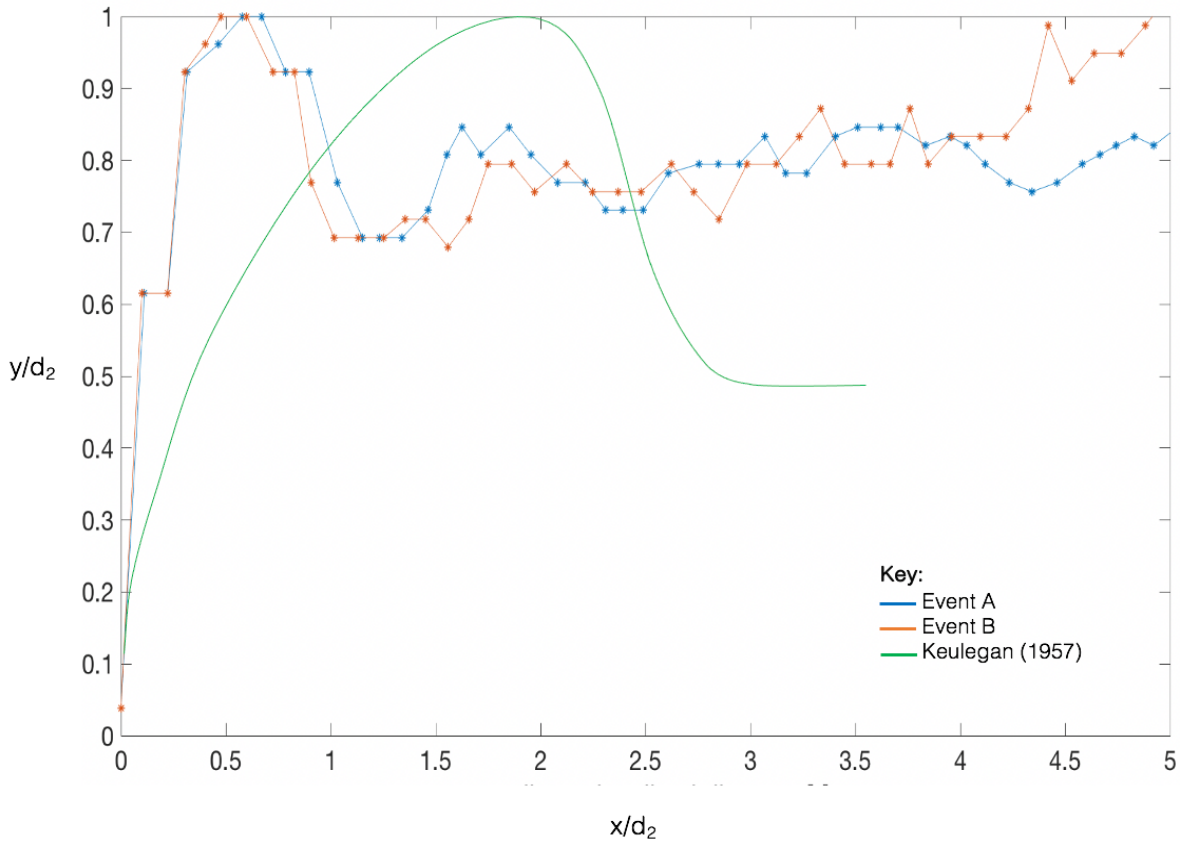

Figure 4.10. Changes in the head thickness (y) of two fast Congo Canyon turbidity currents (events A and B) over distance (x), compared with the average head shape observed during 30 laboratory flows (Kuelegen, 1957). Flows have been non-dimensionalised by dividing the observed flow thickness (y), and the distance behind the flow front (x), by the maximum head thickness (d_2). Data from the fastest event (C) has been omitted. The high velocities in event C ensured that the head of the flow moved past the sensor during the 9 second interval between measurements; therefore the head was not captured.

4.4.2.2. Evidence of billows and large-scale mixing

In the head of turbidity currents, two types of instabilities enable mixing with the ambient fluid (i.e. entrainment; Figure 4.1). First, tunnel-like clefts and protruding lobes (Allen, 1971; Simpson, 1972; Kneller et al., 1999) entrain fluid into the lower head, while simultaneously towards the back of the head, Kelvin Helmholtz billows mix fluid between the upper flow and the ambient water. However, ADCPs are typically unable to measure data within the first few meters above the seabed (see Methods section 4.2.1.2), therefore only billows are discussed in further detail. A series of Kelvin Helmholtz billows can form from turbulence generated when the upper flow shears with the overlying ambient fluid (Ellison and Turner, 1959; Britter and Simpson, 1978; Figure 4.1). Thus, faster flows generate greater turbulence and form larger billows, while slower flows generate less turbulence and billows are therefore less significant. The field observations presented in this study are consistent with

this understanding, as faster Type 1 flows had greater fluctuations in thickness ('billows') in their initial stages. In contrast, slower Type 2 flows showed less evidence of billows (Figures 4.7 and 4.8), which suggests less mixing in the head. Overall, the presence of billows has important implications for determining the flow structure that follows. The following section explores how this zone of mixing divides the head from the body, to create a neck.

4.4.2.3. Flow thinning behind the head

Laboratory experiments with saline density flows (Ippen and Harleman, 1952; Keulegan, 1957; Keulegan, 1958; Middleton, 1966; Kneller and Buckee, 2000) observed that the area immediately behind the head thinned rapidly, forming a neck (Figure 4.10). Komar (1972) first proposed that a neck structure occurs when the head outruns the body. But determining in detail how a neck forms is non-trivial, since laboratory flows may exhibit a neck as an artefact of the experimental design; for example, from the initial release of a large volume of fluid during lock-exchange studies. Additionally, few studies (Komar, 1972; Middleton, 1993; Simpson, 1997; Lowe et al., 2002) have directly addressed this topic of neck origin, and with contradicting conclusions. Yet, previous works agree that the type of mixing within a turbidity current plays an important role in determining whether the head stretches away from the body. From these studies, two main models have emerged.

4.4.2.4. Existing models for turbidity current flow thinning

From indirect studies it was first proposed that flow thinning occurs behind the head of turbidity currents, when significant amounts of seawater is lost though billow structures (Figure 4.11A; Middleton, 1993; Simpson, 1997). To compensate for this loss of volume, fluid from the body of a turbidity current travels to the flow front, and the sediment concentration in the head becomes diluted in the process (Simpson, 1997). In contrast, Lowe et al. (2002) showed that fluid in the body travels forward but does not reach the very front of the head. Billows instead draw this fluid upwards, where it mixes with the ambient fluid, leaving the head region undiluted (Figure 4.11B). Overall, these indirect studies suggest that fluid from the body must supply the head to compensate for this loss of seawater, which infers that the body travels faster than the head. But these conclusions are based on the understanding that mixing occurs predominantly along the upper flow body (Ellison and Turner, 1959) and subsequently assumes

lesser entrainment occurs in the head. More recently, it has been suggested that the head structure is capable of entraining up to ~75% of the ambient seawater that it displaces (Sher and Woods, 2017). These classic models for flow thinning likely understate the role of entrainment in the head, which may also explain why their conclusions are at odds with the fundamental idea that the head stretches away from the body (Komar, 1972). An alternative model by Mohrig et al. (1998) showed that the head can travel faster than the body when ambient seawater intrudes beneath the head (Figure 4.11C), reducing the friction between the flow and the seafloor. Thus, the flow head stretches away from the body in a process termed hydroplaning, at least for submerged debris flows with high sediment concentrations.

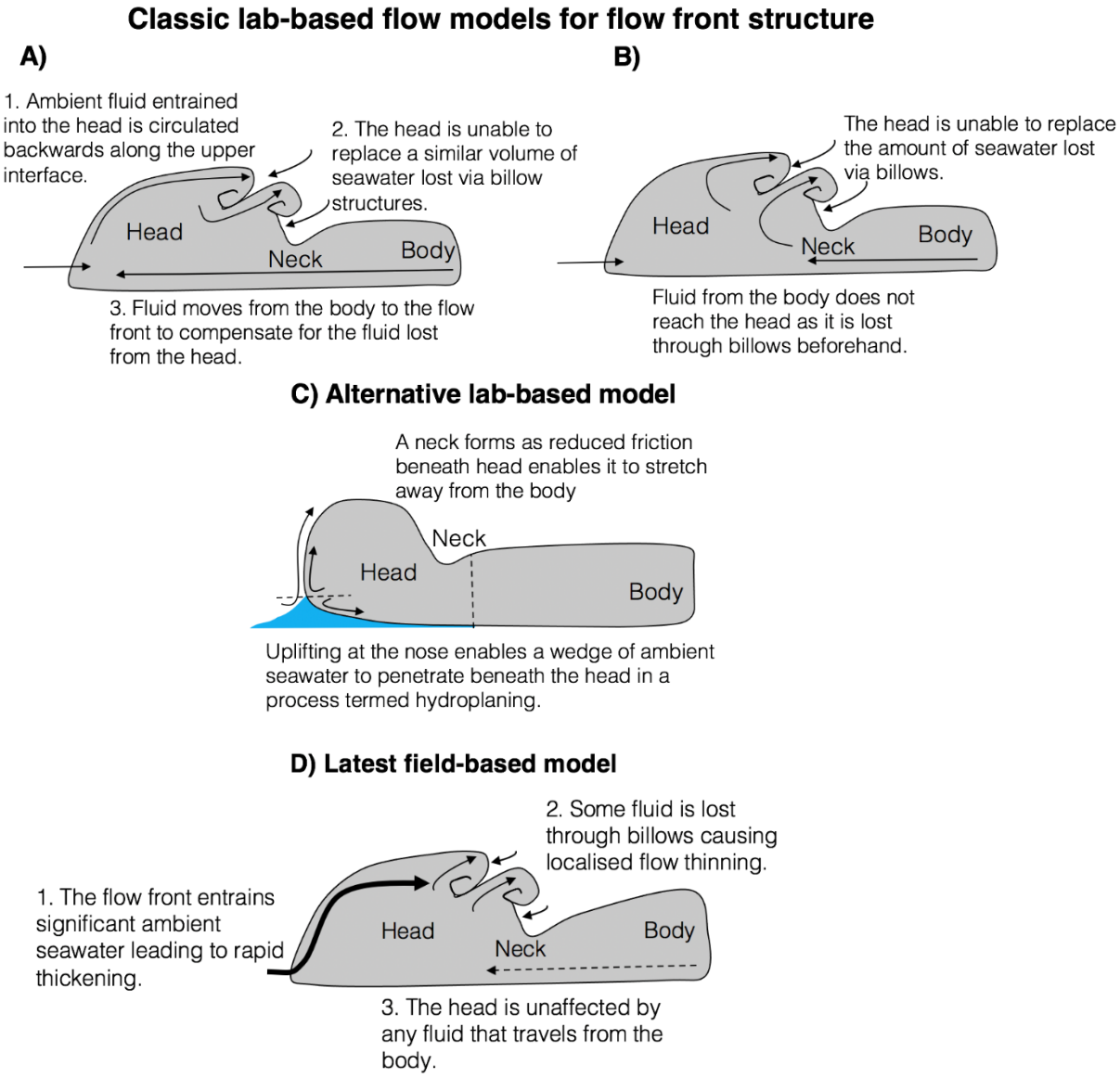

Figure 4.11. Conceptual turbidity current drawings (not to scale) showing different models for flow thinning, where loss of fluid from the head (black arrows pointing away from the flow) leads to the development of a neck structure behind the head. Conversely, entrainment of seawater into the head (arrows pointing towards the flow) enables the flow to increase in volume. The length of the black arrows indicates greater entrainment or detrainment. **A)** The earliest model for flow thinning is based on laboratory experiments (Middleton, 1993; Simpson, 1997) that suggested a neck forms when significant seawater is lost from the head via billow structures. **B)** A similar model was later proposed by Lowe et al. (2002), with the main difference that fluid from the body does not reach the head, as it is instead detrained through billows. But both of these models (A-B) suggest fluid from the body replaces the fluid volume lost from the head, and thus infer that the body outruns the head. Under these conditions, it remains unclear how a head that does not stretch away from the body would form a neck. **C)** An alternative model by Mohrig et al. (1998) suggests that the head outruns the body when ambient fluid flows underneath the head of a turbidity current (shown in blue); such that the friction between the head and the seafloor is lesser than the seafloor friction acting on the body. **D**) A new model is proposed based on the field observations presented in this Chapter, and these observations are also supplemented by the recent understanding that the head of a turbidity current is the dominant site of entrainment (Sher and Woods, 2017).

4.4.2.5. Comparison of field observations to existing models for flow thinning

This study is unable to discern whether hydroplaning occurred during flow events in the Congo Canyon, as ADCPs did not measure the lower few meters of the flows. However, these results do suggest that a flow must attain sufficiently high velocities in order to form a neck, since necks were observed only during Type 1 flows that had velocities >1.5 m/s. When compared to the classic models for flow thinning (Simpson 1997; Lowe et al., 2002), similarly large billows were observed during some of the fastest (Type 1) flows. But the velocity profile data does not show any significant contrast between the speed of the head and the body (Figure 4.7). A likely explanation is that the ADCP did not capture these faster velocities, since they typically occur in near-seafloor regions where the data cannot be resolved. Despite this lack of information, it is reasonable to infer that the fastest Congo Canyon flows may have a faster and denser head compared to the body, as previous studies from a similar location have observed this to be the case (Azpiroz-Zabala et al., 2017; Simmons et al., 2020). But decapitation of the head from the rest of the flow does not occur, likely as the flow head stretches away from the body to create a neck. The head subsequently becomes diluted due to a reduced supply of sediment brought from the body, consequently the head slows until the neck, and body are propagating at the same rate and the flow reaches a steady state (Komar, 1972).

Overall, these results suggest that oceanic turbidity currents may develop a neck when travelling sufficiently fast (>1.5 m/s). Previous work indicates that faster flows are likely to entrain more material (Ellison and Turner, 1959; Parker et al., 1987), and that the head may be the dominant site for entrainment (Sher and Woods, 2017). Thus, this contribution infers that a neck may become well-developed when material is rapidly eroded from the seafloor and entrained into the front of the head. While some seawater is lost from the back of the head via billows (Figure 4.11D). Contrary to past models, we infer that the head structure will be largely undiluted by movement of fluid from the body (Figure 4.11D).

4.4.3. How does the frontal structure affect the motion of ambient water in front of it?

To provide a complete picture of how turbidity current fronts work, it is also useful to explore how the head interacts with the surrounding sediment-free seawater. A notable observation from this study is that faster moving flows (events A and B) show anomalously high velocities, before an increase in acoustic backscatter is detected (Figure 4.8). Thus, these

high velocities occur before the arrival of sediment-laden water in the turbidity current (Figure 4.8). This lag is ~30 seconds (equivalent to a horizontal distance of ~5m), which implies that there is a zone of sediment-free water moving more quickly (0.4-0.8 m/s; Figure 4.6) than the ambient seawater (0.2-0.35 m/s; Figure 4.5B). Herein, this initial zone of moving sediment free water is termed a 'water blast' (Figure 4.8).

There are no turbidity current studies to date that have documented this water blast feature, although a similar 'air blast' feature is described in literature on terrestrial snow avalanches and landslides. Air blasts that contain negligible particles occur immediately in front of large and rapid terrestrial snow avalanches (McClung and Schaerer, 2006) and rock avalanches (Zhuang et al., 2019). These blasts develop from pressure waves commonly generated within 30 seconds after initiation of an avalanche (Zhuang et al., 2019), but arrive before the event. The air blast's velocity can reach similar speeds to a Force 12 hurricane (<35 m/s; Zafren et al., 2018). However, in the Congo Canyon, the water blast measured ahead of some turbidity currents is much weaker than the air blasts observed for snow or rock avalanches. Since submarine sediment flows are typically much slower moving (<3 m/s), the submerged blast wave moves at only 0.4-0.8 m/s (Figure 4.8). Yet, this novel observation from the Congo Canyon suggests that turbidity currents can push a few meters of clear water ahead of their front. The weaker development of these submarine blast waves is perhaps unsurprising, given the relatively slow speeds of turbidity currents when compared to snow and rock avalanches; and given that seawater is ~100-50 times more viscous and ~800 times denser than air.

4.5. Conclusions

This study analyses the most detailed direct measurements yet from turbidity currents in the deep ocean in order to understand the structure of the flow front, with these field data coming from ADCP-moorings in the Congo Canyon. This study finds that different flows at the same location can develop into one of two frontal types. These front types are determined by whether a fast (>1.5 m/s) rapidly thickening head (Type 1) develops, or a slow (<1 m/s) gradually thickening front forms without a distinct head (Type 2). Type 1 flows have broad similarities with the classic shape identified in laboratory experiments, particularly a distinct head structure that contains large-scale billows towards the back (Middleton, 1993; Simpson

et al., 1997), followed by a neck. This head structure has important implications for the flow shape that follows, as our results suggest that sufficiently high velocities (i.e. Type 1 flows; >1.5 m/s) are necessary to form a neck (Figures 4.7 and 4.8). Additional factors are also inferred to determine how a neck might eventually develop, such as whether seawater entrainment dominates within the head. Finally, for the first time, turbidity currents are shown to push a thin zone (<5 m) of sediment-free water in front of the main flow. This observation is termed a water blast, due to its similarity to air blasts associated with both powder snow avalanches and rock avalanches.

Chapter 5: Thesis Conclusions

Overall, this thesis seeks to understand the fundamental behaviour and evolution of submarine turbidity currents, using unusually high resolution field data. Previously there were very few direct measurements of oceanic turbidity currents (Talling et al., 2012), ensuring they were poorly understood (Piper and Normark, 2009; Talling et al., 2015; Paull et al., 2018). This thesis analyses arguably the two most detailed sets of direct field measurements yet collected for submarine turbidity currents. Each dataset includes measurements from multiple locations along the path of multiple turbidity currents, and these data were acquired from two field sites: the Monterey Canyon, situated offshore California (Paull et al., 2018), and the Congo Canyon, located offshore West Africa (Talling et al., 2021).

A better understanding of turbidity currents has widespread importance, because these often powerful events can occur relatively frequently at some locations (Chapter 2-4; Paull et al., 2018), and dominate sediment transfer from the continental shelf to the deep sea (Pirmez and Imran, 2003; Babonneau et al., 2010). These flows can also transport significant fluxes of sediment, heat, nutrients, and organic carbon (Milliman and Syvitski, 1992; Canals et al., 2006; Galy et al., 2007; Talling et al., 2007; Kao et al., 2010). Moreover, ancient turbidity current deposits can form valuable records of longer-term Earth history, and hydrocarbon reserves (Weimer and Link, 1991; Nilsen et al., 2007). Modern-day turbidity currents can severely damage or break seafloor cables that carry over 99% of global data (Carter et al., 2014), as well as pipelines and other critical infrastructure (Clare et al., 2017). Thus, furthering our understanding of turbidity currents will improve risk-mitigation strategies for marine construction built in their pathway.

Chapter 1 introduces the methods and field sites used within the thesis, including Acoustic Doppler Current Profilers (ADCPs), whose data are used throughout subsequent chapters. Chapters 2 and 3 analyse ADCP and other timeseries data with sub-minute resolution. These data were acquired from Monterey Canyon, where the most extensive monitoring study along a turbidity current pathway to date was conducted (Paull et al., 2018). Chapter 4 presents data from the Congo Canyon, where ADCP-data had both high temporal resolution and also high spatial resolution, since two ADCP-mooring stations were deployed only ~300 m apart. The head of the Congo Canyon lies within the mouth of the Congo River, which supplies a larger amount of much muddier sediment (Shepard and Emery, 1973; Van Weering and Van

Iperen, 1984), compared to the littoral-drift fed Monterey Canyon (Paull et al., 2005). By monitoring flows across these two field sites, this thesis is able to address the following research questions:

1. What effects(s) do turbidity currents have on ocean stratification (Chapter 2)?
2. How much mixing do turbidity currents experience over time (Chapter 3)?
3. Can turbidity currents form different frontal structures (Chapter 4)?

The main conclusions from these individual chapters are summarised briefly in the next section, which is followed by a discussion of more general research themes that link across these chapters. Finally, this chapter finishes with recommendations for future work.

5.1. What effects(s) do turbidity currents have on ocean stratification (Chapter 2)?

Turbidity currents travel along the seafloor as a mixture of sediment and seawater, which is transported from shallower water depths to the deep ocean. The density of the water carried with a turbidity current evolves over time, and depends on the initial water temperature and salinity, in addition to subsequent mixing with the ambient seawater (Hurzeler et al., 1966; Quadfasel et al., 1990). But understanding how the seawater content evolves within a turbidity current is challenging, due to the inherent difficulty in obtaining direct measurements in the field. Consequently, a limited number of turbidity current studies have analysed temperature and salinity sensor data, and nearly all these measurements were recorded at only a single point above the seafloor. Thus, our understanding of how these properties evolve within a turbidity current is formed almost exclusively from laboratory experiments and theory (Hurzeler et al., 1966; Sparks et al., 1993; Gladstone and Pritchard, 2010). Additionally, analogies have been made between behaviours observed in turbidity currents and terrestrial gravity currents (Sparks et al., 1986, 1977; Calder et al., 1997; Pritchard and Gladstone, 2009).

Based on previous studies (Hurzeler et al., 1966; Sparks et al., 1993) it has been proposed that once sufficient sediment has settled and/or been deposited from a turbidity current, the remaining seawater within the flow can rise vertically from the seafloor upwards. This vertical movement occurs because a turbidity current can carry seawater that has retained some of its upslope water-mass properties (i.e. warmer and fresher). A turbidity current that reverses its buoyancy in this way is considered to have lofted (Sparks et al., 1993). A similar

lofting phenomenon is observed on land, when buoyant co-ignimbrite clouds rise due to their high internal flow temperatures (Sparks et al., 1986). Chapter 2 provides the first opportunity to observe whether oceanic turbidity currents loft, using vertical profiles of temperature, salinity, and turbidity (a proxy for sediment concentration) that were collected in Monterey Canyon. These data were measured during two turbidity currents that passed through a single distal mooring site. Both events were fast moving (maximum speeds of ~4 m/s). However, only the fastest flow strongly lofted, with a portion of its water mass rising for up to ~300 m above the seafloor. These results suggest that a greater amount of warmer water may have been entrained into the fastest flow during its initiation. Interestingly, these data show that a significant amount of time passed before the water column recovered to pre-event conditions. Overall, the seawater temperature remained anomalously warm for 0.75 days, whilst excess static sediment lingered for two days at the mooring site, an observation that is absent from previous lab-based models (Hurzeler et al., 1966; Sparks et al., 1993; Hog et al., 1999). The implications of such lofting and related behaviour could profoundly influence both deposit structure (Gladstone and Pritchard, 2010), and the transport of oxygen and nutrients to the deep sea (Kao et al., 2010).

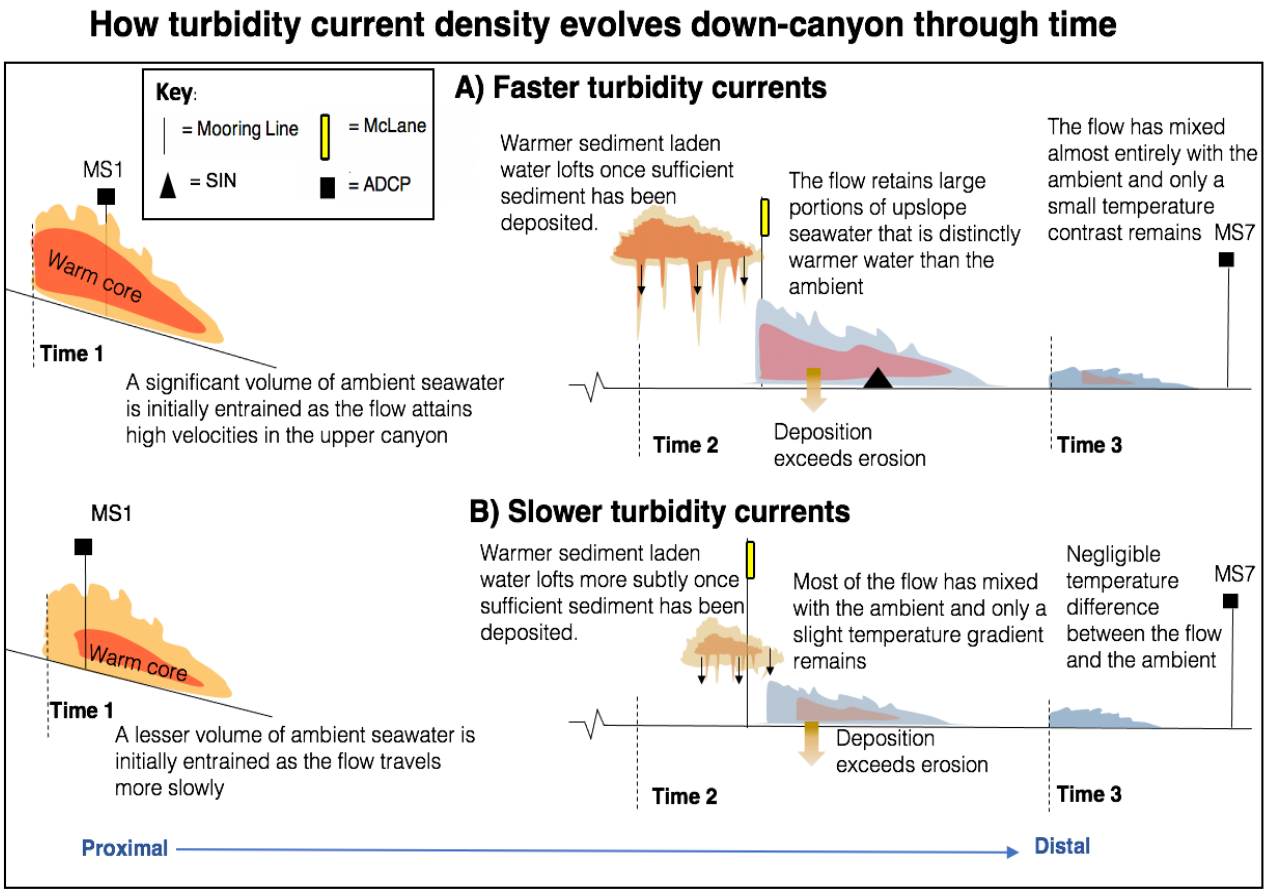

Figure 5.1. **A)** Concept illustrations (not to scale) based on field observations from Monterey Canyon, where temperature differences between a faster (A) and slower (B) turbidity current led to rather different lofting events. A turbidity flow travels through various locations over time, losing heat (red/orange–light blue–dark blue) and eventually enough sediment for lofting to occur. A) Faster flows were thicker, indicating more up-canyon seawater was entrained (warm core; Time 1). A strong temperature contrast developed as the flow moved into the deeper ocean (Time 2), which enabled lofting to occur high into the water column. By the most distal location, only a slight temperature contrast remained between the flow and the ambient (Time 3). In comparison **B)** slower flows were thinner, suggesting less up-canyon seawater was entrained (Time 1). Once the flow moves into the deeper ocean (Time 2) only a weak density contrast remained, and lofting was less pronounced (Time 2). Eventually, all seawater within the flow became mixed (and/or detrained) with the ambient seawater, and all remnants of the warm core dissipated (Time 3).

5.2. How much mixing do turbidity currents experience over time (Chapter 3)?

How turbidity current behaviour evolves is strongly controlled by mixing, a process in which sediment and seawater are exchanged between a turbidity current and its surroundings. Specifically, the upper flow boundary can mix with the ambient seawater, due to shear generated with the overlying ambient seawater (Ellison and Turner, 1959; Middleton, 1966). Additionally, friction between the basal flow layer and the seafloor can lead to the incorporation of seafloor sediment, providing the density that drives flows forward (Pantin, 1979; Sequeiros et al., 2009).

A better understanding of mixing is important, as this process determines the volume of material (i.e. seawater, sediment, heat, salt, nutrients, organic carbon and pollutants) transported by these flows, the geometry of their deposits, and also how likely flows are to devastate seafloor infrastructure. The depth-averaged water entrainment model of Parker et al. (1987) is one of the most widely used, but it is well known to overpredict the thickness of full-scale turbidity currents (Traer et al., 2012), as water detrainment (lowering of the upper flow boundary) is neglected yet important (Bolla Pitaluga et al., 2018). Thus, numerical models need to include new entrainment relationships, which are better calibrated using field observations. Previously, a lack of direct measurements has ensured that such models are rarely tested using observations from oceanic turbidity currents. This new study based on field data collected at three locations in Monterey Canyon provides a valuable opportunity to test past mixing models.

Chapter 3 presents changes in water temperature, velocity, and backscatter (a proxy for sediment concentration) within two separate turbidity currents in Monterey Canyon, which are some of one of the most detailed monitoring data to date. Each turbidity current steadily increased in volume, as it travelled for over 44 km through three mooring stations. Changes in flow volume between pairs of moorings were compared to the volume increase predicted by Parker et al.'s (1987) entrainment model, and the volume of both flows is significantly overpredicted at each mooring. This overprediction is likely due to a lack of a detrainment parameter. Chapter 3 then shows that when sediment grains are modelled to settle out of suspension with their terminal velocity (i.e. detrainment occurs; Bolla Pitaluga et al., 2018), flows drastically decrease in volume. Flows that detrain water in this way are predicted to have completely dissipated before running out past the second mooring, which is unrealistic, as the flows ran out much further in the field. Detrainment is then modelled with grains settling at only 5% of their terminal settling velocity in still water, yet flow thickness remains strongly overestimated compared to field data. This may suggest that detrainment is rather suppressed, via protection of a near-bed zone from mixing (Luchi et al., 2018; Dorrell et al., 2019). These results underline the need for models that consider vertically varied flow behaviour, in particular, the distribution of sediment. The data presented in Chapter 3 also suggests that some of the links between turbidity current entrainment and flow structure diverge from classic models (as discussed in detail in the Section 5.4). In particular, Chapter 3 finds that the thickness of the near-bed flow layer that is protected from mixing is determined by the height of the velocity maximum; which initially lies close to the seabed, before gradually rising. This

near-bed layer that is protected from mixing was inferred by Luchi et al. (2018), and they suggest this explains how turbidity flows are capable of running out over great distances, even when the entraining flow layers are thinner than classically thought. It has been proposed that the head of a turbidity current may be responsible for the most entrainment. Previous work suggests that the head can incorporate between 60-75% of the ambient seawater it encounters (Sher and Woods, 2017). This conclusion is in keeping with field data from Monterey Canyon, which show that flows have a colder frontal region (Figure 5.3).

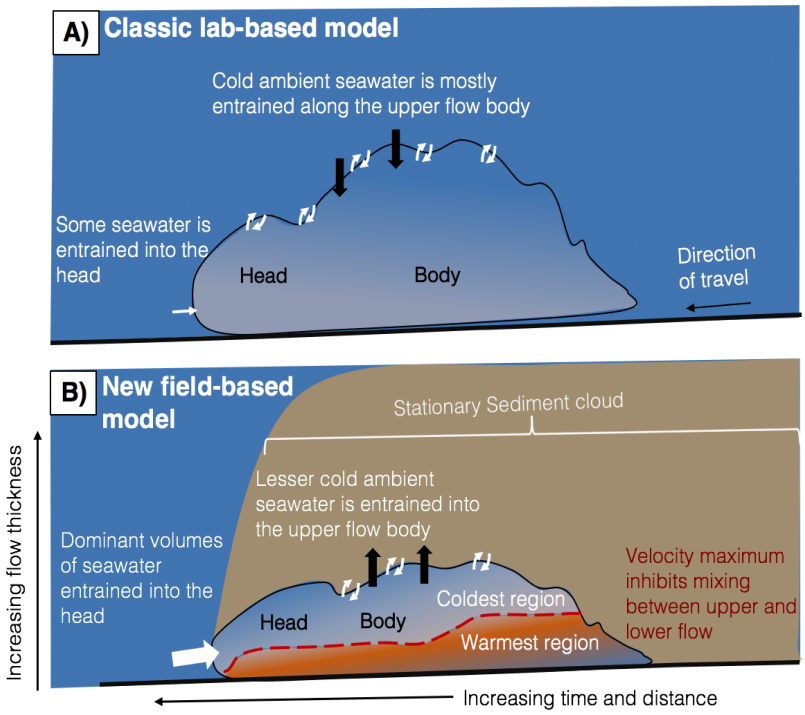

Figure 5.2. Concept cartoons (not to scale) showing a general model of how a turbidity current mixes with the colder surrounding seawater, and how the flow's internal temperature structure is affected by this mixing. **A)** Classical model for a turbidity current in which shear mixing occurs along the flow's upper surface (paired white arrows), and a lesser amount of mixing also occurs at the flow front (single white arrow). Sediment settling can also lead to detrainment of water along the flow's upper surface (Bolla Pittaluga et al., 2018), represented by large black arrows. **B)** A new model for turbidity current mixing based on observations from Monterey Canyon. As in the classical model, shear mixing occurs along its upper surface (paired white arrows). However, the flow front also introduces significant amounts of cold surrounding seawater into the turbidity current (large white arrow). Sediment settling may then lead to water detrainment (large black arrows). However, reduced mixing at the height of the velocity maximum (red dashed line) also shields a lower region of the flow from vigorous mixing. This lower layer (labelled 'warmest region') is located below the velocity maximum, and away from the flow front. In this protected lower layer, some up-canyon water mass properties are preserved as the turbidity current travels downslope. Sediment may also be transferred from the (moving) upper part of the turbidity current into stationary surrounding seawater, creating a static (i.e. non-moving) sediment cloud that continues to linger after the turbidity current has passed.

5.3. Can turbidity currents form different frontal structures (Chapter 4)?

The frontal structure of a turbidity current is thought to be of importance for three main reasons. First it is a dominant site for entrainment (Chapter 3; Allen, 1971; Sher and Woods, 2017). Second, the flow front may be fast and dense, and thus drive flows (Azpiroz-Zabala et al., 2017). Third, the front is the most violent part of the flow, which is primarily responsible for damaging seafloor cables (Heezen and Ewing, 1952). But despite recent advances in field monitoring, detailed spatial observations of turbidity current fronts are extremely rare. Instead, laboratory experiments (Middleton, 1966; Allen, 1971; Simpson, 1979; Sher and Woods, 2017) form the majority of our understanding of frontal flow structure. However, lab-based results are limited by well-known scaling issues (Talling et al., 2015), which leads to uncertainty surrounding how accurately these results represent full-scale flow structure.

To better understand turbidity current fronts, Chapter 4 presents the first detailed analysis of field observations from the frontal parts of turbidity currents, which occurred in the Congo Canyon in 2019-20. Time-series of velocity and backscatter data from ADCPs recorded six flows, as they passed in between two moorings, located only ~ 300 m apart. At the highest resolution ADCP-mooring, these timeseries data were inverted to distance data, according to the method of Khripounoff et al. (2012). Overall, Chapter 4 finds that turbidity currents travelling along the same path can develop one of two frontal types, depending on the flow speed. Flows were either fast and developed a distinctly thicker head structure relative to the body, or were slower and did not develop a distinct neck. The difference in the development of a head structure suggests that different mixing processes occurred in these two flow types. For example, large-scale billow structures were observed only behind the head of faster flows. Billows develop due to shearing between the upper flow and the overlying ambient fluid (Ellison and Turner, 1959), and can modify the flow structure behind the head due to localised mixing (Middleton, 1993; Simpson, 1997). For the first time, Chapter 4 also shows that powerful turbidity flows can push a small amount of sediment-free seawater ahead of a turbidity current. This ‘water blast’ is broadly similar to ‘air blasts’ that travel ahead of some subaerial snow and rock avalanches (McClung and Schaerer, 2006).

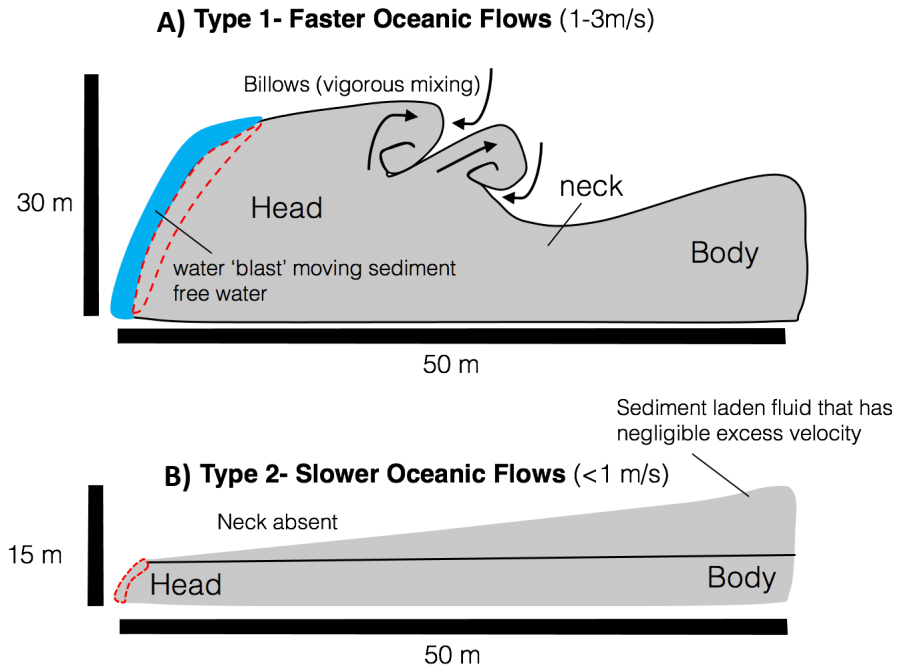

Figure 5.3. Conceptual drawing illustrating the two different flow types observed in this study. **A)** Type 1 turbidity currents comprise three separate regions (i.e. a distinct rapidly thickening head, followed by a thin neck, and a trailing body). The frontal portion of the turbidity current that first meets the ambient water is termed the frontal edge (red dashed line). The frontal edge pushes a thin wave of ambient water, which is termed a blast wave, ahead of the turbidity current (solid blue area). **B)** In contrast, Type 2 flows do not show a distinct head structure as they gradually thicken over time, and the overall thickness is predominately comprised of sediment suspended above the main flow.

5.4. Key research themes that emerge from this thesis:

The findings presented in this thesis can also be synthesised into two wider research themes. The first theme is appropriate modelling of water detrainment processes during turbidity current evolution. The second theme focuses on the classical flow structure of a turbidity current from past works, and a recent shift towards more detailed structural models based on the latest observations.

5.4.1. Appropriate modelling of detrainment processes during turbidity current evolution

In Chapter 3, turbidity currents are shown to travel over long distances despite their ability to mix vigorously with the surrounding seawater. It is classically understood that this mixing process is largely controlled by flow speed and sediment concentration, and thus bulk or gradient Richardson number (Ellison and Turner, 1959). But, Chapters 2-3 highlight that both turbidity current sediment distributions and accompanying sedimentation rates remain poorly understood. From previous studies, it is known that the sediment distribution within a

turbidity current is closely linked to the amount of turbulence generated (Felix et al., 2001; Lowe et al., 2000; Baas et al., 2005; Cantero et al., 2011). For example, grain sizes laterally grade from coarse sediment in the nose to fine sediment in the tail (Baas et al., 2005). Consequently, the head contains mostly coarser and well-mixed grains, as the upwards turbulence is insufficient to remobilise and mix this heavier sediment (Figure 5.4). In contrast, the body is characterised by a stratified grain size distribution, so that smaller sediment grains can be remobilised upwards due to turbulence, before settling out. However, the majority of classic models that are designed to predict turbidity current behaviour, do not account for such complex sediment dynamics. For example, Richardson number-based entrainment models, as shown in Chapter 3, typically neglect detrainment and require depth-averaged parameters that over-simplify sediment behaviour, leading to unrealistic results. Thus, realistic models of flow behaviour require a flow water detrainment term(s) in addition to mixing.

Chapters 2 and 3 also highlight that some of the most important detrainment terms are those that define the relationship between vertical changes in sediment distribution and turbulence, over time (Figure 5.4). The importance of this issue has also been acknowledged in a number of key works (Cantero et al., 2009; Yeh et al., 2013; Cantero et al., 2012; Sequeiros et al., 2012; Baas et al., 2015). Crucially, past works have shown that flow turbulence can be dampened by sediment stratification (Cantero et al., 2012), and also by relatively small increases in the concentration of fine sediment (<0.1%; Baas et al., 2015). Thus, realistic models of turbidity current evolution are likely to be ones that appropriately define the sensitivity between sediment distribution and turbulence, in addition to entrainment. Such models would represent a step change in our understanding of turbidity currents; and would provide the knowledge needed to predict turbidity current transport capacity, as well as their deposit structure. In addition, the risk that these flows pose to critical seafloor infrastructure could be more accurately predetermined, and thus better mitigated.

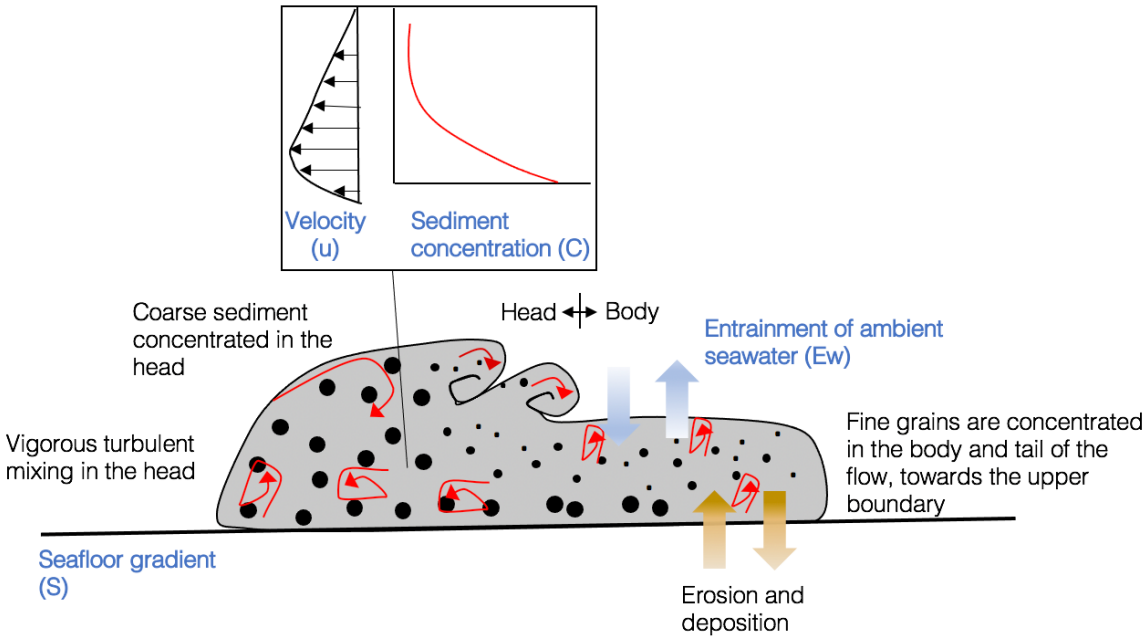

Figure 5.4. Concept model (not to scale) of a turbidity current travelling downslope (S), where flow evolution is influenced by sediment dynamics, mixing and turbulence (red arrows). The velocity and suspended sediment gradients (inset) determine the amount of turbulence (red arrows) at the base of the flow and at the upper interface of the current. Turbidity flows become diluted by incorporating ambient seawater along the upper interface (blue arrows) or by deposition (brown arrows), causing the flow to decelerate. If there is sufficient shear between the flow and the seafloor then basal erosion increases the flow density, and the flow accelerates. Modelling studies used to predict flow behaviour typically include the following field-measured or derived parameters: flow velocity, sediment concentration, seafloor gradient, and water entrainment (blue text). However, better characterisation of detrainment and sediment exchange with the seafloor is needed to produce step changes in our understanding.

5.4.2. Progressing beyond the classical structure of a turbidity current

Over the past decade, there has been a significant shift in our understanding of turbidity current structure; which has been brought about by the emergence of new high-resolution field data (Cooper et al., 2013; Hughes-Clarke et al., 2016; Paull et al., 2018; Talling et al., 2021). Classical turbidity current studies proposed that the flow is vertically divided into a seawater entraining upper layer, and a sediment entraining near-bed layer. However, the ADCP data presented in this thesis, along with more recent existing work, highlights that flow structure can differ in the vertical and along-flow direction from classical models (Figure 5.5). Chapter 3 indicates that vertical partitioning of sediment and seawater is linked to the height of the velocity maximum, a conclusion that was first proposed by Luchi et al. (2018). Chapter 2 shows

that a dissipating flow can transform a portion of its upper layer into a rising sediment cloud (i.e. loft), similar to rising ash clouds from volcanic eruptions. Thus, via these Chapters and past work (Khripounoff et al., 2012; Cooper et al., 2013; Xu et al., 2013; Hughes-Clarke, 2016; Azpiroz-Zabala et al., 2017; Paull et al., 2018; Talling et al., 2021), the vertical structure of a turbidity current is becoming understood in greater detail, due to the vertical profiling capabilities of ADCPs. However, insights into the along-flow structure of turbidity currents may not be able to keep pace, unless future monitoring studies obtain measurements with greater spatial resolution. This can be achieved by deploying a greater number of ADCPs in closer proximity to one another, or adopting new measurement techniques (discussed in further in the following section).

Currently, the classic model for along-flow structure consists of a distinct head, body and sometimes a tail (Ellison and Turner, Simpson and Britter, 1979; Allen, 1971; Middleton, 1993). Although in Chapter 4, it is shown that the frontal structure of a turbidity current can be divided into one of two types; depending on whether a distinct head is present. Recent work (Azpiroz et al., 2017; Simmons et al., 2020) has similarly found that the front of turbidity currents is not necessarily characterised by the prominent head structure observed in laboratory flows. Moreover, Chapter 4 also highlights that ADCP monitoring can create bias towards both slower-moving flow fronts, and towards the spatially longer body and tail regions. Thus, highly erosive and faster moving flow fronts are inherently under-represented because these types of flows are less frequent. Additionally because when fast erosive flows do occur, they tend to cause significant damage and/or tilting of moorings, which leads to losing some or all of the data (Talling et al., 2013; Clare et al., 2020). Yet, capturing the entire flow front is of importance as this region is thought to entrain up to 75% of the ambient seawater it encounters (Sher and Woods, 2017). Chapter 4 also suggests that the front may be influential in determining the structure of the flow that follows. Although, obtaining increasingly detailed flow front data requires the deployment of more ADCPs (Clare et al., 2020), and requires that they are capable of recording more measurements during the same deployment period. But such an approach would require further battery and memory capacity beyond what is currently feasible. Thus, new deployment methods and measurement techniques are needed, and these will be discussed further in the following section.

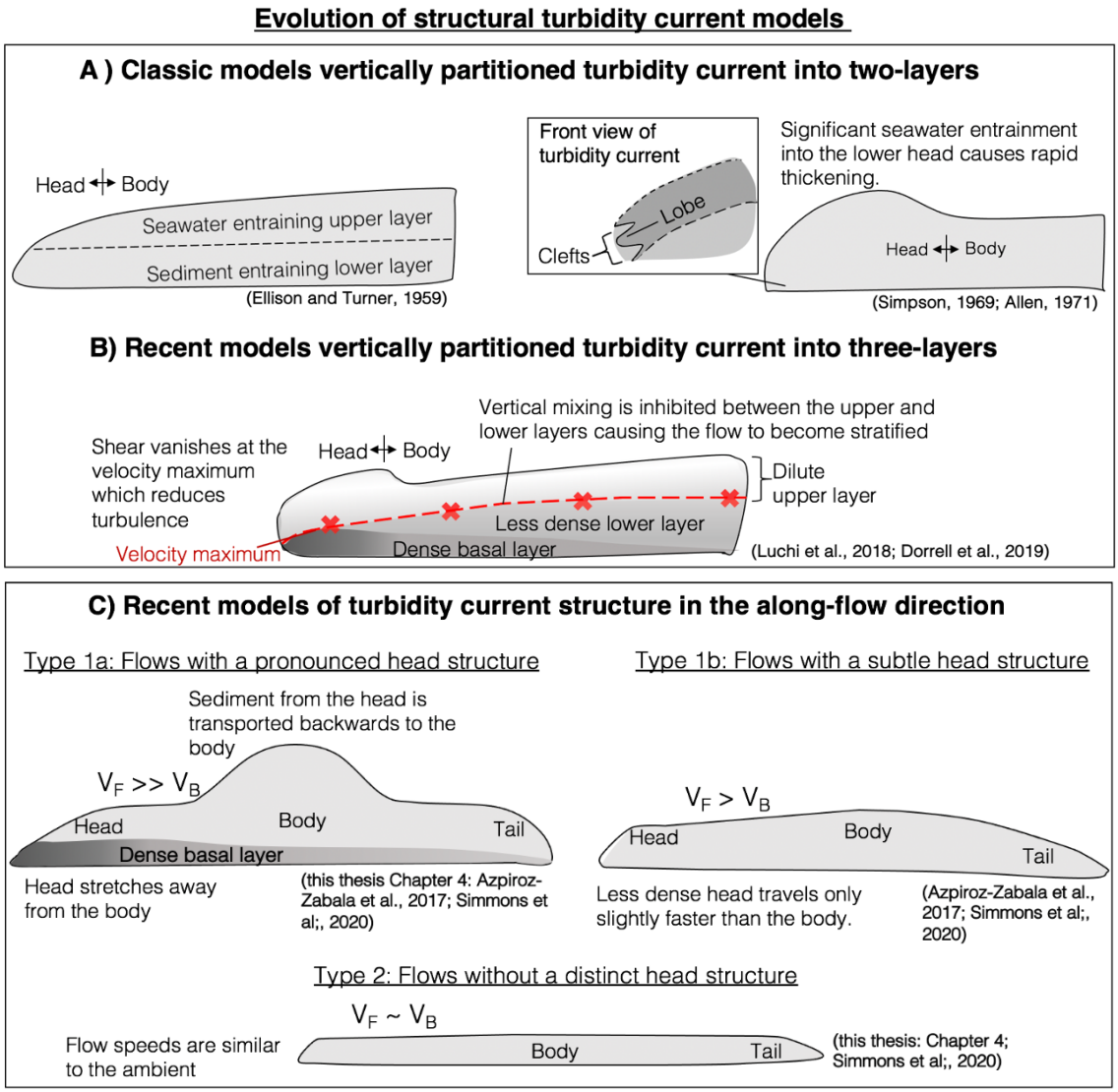

Figure 5.5. A brief overview of the changes in general models (not to scale) used to describe turbidity current structure. These structural models have become increasingly detailed using observations from: indirect flows that typically lasted minutes (A), and recent field observations with flows that lasted several hours (B) to days (C). **A)** Early laboratory studies led to pioneering models for turbidity current structure. First, it was proposed (Ellison and Turner, 1959; Parker et. al., 1986) that turbidity currents mostly entrain surrounding seawater along their upper flow boundary, while the lower layer erodes sediment from the seafloor. Later works (Simpson, 1969; Allen, 1971) suggested that turbidity currents can also entrain significant volumes of seawater into the lower head via cleft and lobe structures. Thus, flows can develop heads that are distinctly thicker than their body. More recent observations **(B-C)** suggest that the dense basal layer of turbidity currents is much thinner (Paull et al., 2018), than proposed in previous models. The separation of the upper (i.e. more dilute) flow layer from the lower (i.e. denser) flow layer is thought to occur at the velocity maximum (Luchi et al., 2018; Dorell et al., 2019), where shear vanishes, and reduced turbulence enables the flow to become stratified. C) Flows that lasted up to several days displayed different structures, although they travelled along similar paths in the Congo Canyon (Chapter 4; Azpiroz-Zabala et al., 2017; Simmons et al., 2020). The development of these different flow structures is thought to depend on the gradient between the frontal velocity (VF) and the body velocity (VB), in addition to the sediment concentration within the flow.

5.5. Future work

Turbidity current research as a whole is still in its relatively early stages, thus the future outlook largely involves solving fundamental questions about flow behaviour. The following section discusses two important knowledge gaps in this field, and outlines possible field-based strategies that can be used to narrow these gaps.

5.5.1. Identifying patterns in flow behaviour

One of the most important knowledge gaps in this field concerns whether there are consistent patterns in flow behaviour across different sites. Some examples of patterns include how flows are triggered (Sumner et al., 2014; Clare et al., 2015; Hage et al., 2019; Sequeiros et al., 2019), and whether they are structurally similar (Chapter 4; Azpiroz- Zabala et al., 2017, Paull et al., 2018). But the identification of such patterns requires a longer term and more detailed picture of flow behaviour. Arguably, direct monitoring is one of the best approaches to obtain this information: by monitoring existing field sites, and exploring new sites altogether.

First, it is advantageous to capture observations at existing field sites, as improved mooring design and placement can be learned through previous observations. Monterey Canyon is a key example, where the deployment of multiple temperature sensors at different heights (see Chapters 2 and 3) successfully captured changes in flow temperature, which can be used as a proxy for mixing. However, moorings in deep-water further down the canyon were only fitted with a temperature sensor at ~65 m above the seafloor, and long run-out flows had always decreased to a thickness that no longer reached the height of the sensor by these moorings. Thus, event temperature data during the waning flow stages was not captured. Despite that the most powerful events had waned by the final mooring, a distinct velocity signature was still detected at the final downstream mooring. This supports the deployment of even more distal moorings in future (> 2 km water depth). Data acquired from the Congo Canyon, as shown in Chapter 4, demonstrate that a sampling rate of around <10 seconds is needed to capture the frontal structure of turbidity currents in sufficient detail. Findings from Chapter 4 highlight the need for targeted studies, where multiple moorings are fitted with ADCPs that are distributed over a much greater extent of the canyon, to capture spatially detailed data.

Second, the monitoring of flows in new locations will help to determine how flow behaviours might vary, within the same system, or between entirely different systems. Chapters 2-4 show that different submarine canyon systems can generate very different flows. In Monterey Canyon, flows persisted for up to several hours, while numerous Congo Canyon events were observed to often last for days at a time (Chapter 4). In addition, different flow events in Monterey Canyon exhibited similar structures (Chapters 2-3; Paull et al., 2018), while flows in the Congo Canyon produced two different flow structures (Chapter 4; Azpiroz et al., 2017; Simmons et al., 2020). To identify patterns in flow behaviour, it is therefore important to be able to distinguish whether hydrodynamic processes influence flow evolution, or whether flow behaviour is pre-determined by the system they flow within. Thus, the monitoring of new canyon sites will provide crucial context for answering this essential question. To build up a complete picture of turbidity currents, information must then come from a range of systems. But to date, only Canadian fjord systems (Prior et al., 1987; Hughes-Clarke et al., 2016; Stacey et al., 2019) and lake settings (Hsu and Kelts, 1985; Normark, 1989) have been directly monitored in similar detail to Monterey Canyon and Congo Canyon. Thus, future priorities should include increasing both the number of field sites and the representation of different marine settings.

5.5.2. Understanding how the near-seafloor layer of a turbidity current works

Currently, ADCPs are one of the most important and commonly-deployed field instruments used to obtain direct measurements of turbidity currents. Yet, a significant limitation is their inability to record measurements over the entire flow thickness, in particular, the dense near seafloor layer (Paull et al., 2018; Wang et al., 2020). A lack of data in this near-bed region occurs as the acoustic energy of an ADCP is often absorbed by high particle loads, which characterise the base of turbidity currents (Thorne et al., 1993; Shen and Lemmin, 1996; Simmons et al., 2020). Thus, the best approach to capturing this data involves the development of novel measurement techniques. For example, hydrophones can record acoustic noise generated by sediment grain collisions (Thorne 1985, 1986). By detecting acoustic (sound) signals emitted from a turbidity current, these devices effectively listen to the high sediment loads, as an event travels downslope (Caplan-Auerbach et al., 2014; Hughes-Clarke, 2016; Lintern et al., 2019; Hay et al., 2021). Additionally, the passive listening method of hydrophones represent a lower cost and lower energy alternative to ADCPs, which consume larger battery and memory capacity to capture measurements. Overall, the lower-energy

approach of hydrophones ensures monitoring of a much wider spatial extent of the water column than current techniques. Implementing new equipment such as hydrophones will therefore be key to capturing near seafloor data. Capturing such data is essential for quantifying the sediment flux of the dense basal region of the flow, which is of importance as this layer is thought to be predominantly responsible for driving the flows downslope (Chapter 3; Dorrell et al., 2018).

5.6. Summary

Future progress in turbidity current research can be brought about (but is not limited to) using the direct monitoring strategies previously outlined in this thesis, to increase both the quality and quantity of available data. Thus, direct observations can be used to test existing hypotheses for how flows work, while other studies (i.e. lab-based, theoretical, and numerical) will also be important for interpreting field observations (see subsection 1.3.2 for a detailed discussion). Such integrated approaches will be crucial to develop models capable of quantifying fluxes of sediment and nutrients that are delivered to the deep ocean. Additionally, estimating both how the overall size of a flow might evolve, and estimating the maximum speeds that will be reached, is essential for predicting whether a flow will damage seafloor infrastructure (i.e. telecommunications cables and energy pipelines). Thus, furthering our understanding of turbidity flows in this manner is timely, given that the construction of seafloor cables and energy pipelines is predicted to increase between 50-70% by 2028 (Bugnot et al., 2021).

References

Akiyama, J. and Stefan, H., 1985. Turbidity Current with Erosion and Deposition. *Journal of Hydraulic Engineering*, 111(12), pp.1473-1496.

Allen, J., 1971. Mixing at Turbidity Current Heads, and Its Geological Implications. *SEPM Journal of Sedimentary Research*, Vol. 41.

Altinakar, S., Graf, W. and Hopfinger, E., 1990. Weakly depositing turbidity current on a small slope. *Journal of Hydraulic Research*, 28(1), pp.55-80.

Amy, L., Peakall, J. and Talling, P., 2005. Density- and viscosity-stratified gravity currents: Insight from laboratory experiments and implications for submarine flow deposits. *Sedimentary Geology*, 179(1-2), pp.5-29.

Anderson, R., 1977. Short term sedimentation response in lakes in western United States as measured by automated sampling1. *Limnology and Oceanography*, 22(3), pp.423-433.

Azpiroz-Zabala, M., Cartigny, M., Talling, P., Parsons, D., Sumner, E., Clare, M., Simmons, S., Cooper, C. and Pope, E., 2017. Newly recognized turbidity current structure can explain prolonged flushing of submarine canyons. *Science Advances*, 3(10).

Baas, J., McCaffrey, W., Haughton, P. and Choux, C., 2005. Coupling between suspended sediment distribution and turbulence structure in a laboratory turbidity current. *Journal of Geophysical Research*, 110(C11).

Babonneau, N., Savoye, B., Cremer, M. and Bez, M., 2010. Sedimentary Architecture in Meanders of a Submarine Channel: Detailed Study of the Present Congo Turbidite Channel (Zaiango Project). *Journal of Sedimentary Research*, 80(10), pp.852-866.

Bagnold, R., 1962. Auto-suspension of transported sediment; turbidity currents. *Proceedings of the Royal Society of London. Series A. Mathematical and Physical Sciences*, 265(1322), pp.315-319.

Black, K. and Rosenberg, M., 1994. Suspended sand measurements in a turbulent environment: field comparison of optical and pump sampling techniques. *Coastal Engineering*, 24(1-2), pp.137-150.

Bolla Pittaluga, M., Frascati, A. and Falivene, O., 2018. A Gradually Varied Approach to Model Turbidity Currents in Submarine Channels. *Journal of Geophysical Research: Earth Surface*, 123(1), pp.80-96.

Bouma, A., 1962. *Sedimentology of some flysch deposits: a graphic approach to facies interpretation*. Amsterdam: Elsevier, p.168.

Bouma, A., Normark, W. and Barnes, N., 2012. *Submarine Fans and Related Turbidite Systems*. Springer Science & Business Media.

Britter, R. and Simpson, J., 1978. Experiments on the dynamics of a gravity current head. *Journal of Fluid Mechanics*, 88(2), pp.223-240.

Buckee, C., Kneller, B. and Peakall, J., 2001. Turbulence structure in steady, solute-driven gravity currents. In: Particulate Gravity Currents (Eds W.D. McCaffrey, B.C. Knellerand J. Peakall), *International Association of Sedimentologists*, 31,173–187. Blackwell Science Ltd, Oxford.

Bugnot, A.B., Mayer-Pinto, M., Airoldi, L., Heery, E.C., Johnston, E.L., Critchley, L.P., Strain, E.M.A., Morris, R.L., Loke, L.H.L., Bishop, M.J. and Sheehan, E.V., 2021. Current and projected global extent of marine built structures. *Nature Sustainability*, *4*(1), pp.33-41.

Calder, E., Sparks, R. and Woods, A., 1997. Dynamics of co-ignimbrite plumes generated from pyroclastic flows of Mount St. Helens (7 August 1980). *Bulletin of Volcanology*, 58(6), pp.432-440.

Canals, M., Puig, P., de Madron, X., Heussner, S., Palanques, A. and Fabres, J., 2006. Flushing submarine canyons. *Nature*, 444(7117), pp.354-357.

Cantero, M., Balachandar, S., Cantelli, A., Pirmez, C. and Parker, G., 2009. Turbidity current with a roof: Direct numerical simulation of self-stratified turbulent channel flow driven by suspended sediment. *Journal of Geophysical Research*, 114(C3).

Cantero, M., Cantelli, A., Pirmez, C., Balachandar, S., Mohrig, D., Hickson, T., Yeh, T., Naruse, H. and Parker, G., 2012. Emplacement of massive turbidites linked to extinction of turbulence in turbidity currents. *Nature Geoscience*, 5(1), pp.42-45.

Caplan-Auerbach, J., Dziak, R., Bohnenstiehl, D., Chadwick, W. and Lau, T., 2014. Hydroacoustic investigation of submarine landslides at West Mata volcano, Lau Basin. *Geophysical Research Letters*, 41(16), pp.5927-5934.

Carter, L., Gavey, R., Talling, P. and Liu, J., 2014. Insights into Submarine Geohazards from Breaks in Subsea Telecommunication Cables. *Oceanography*, 27(2), pp.58-67.

Clare, M., Vardy, M., Cartigny, M., Talling, P., Himsworth, M., Dix, J., Harris, J., Whitehouse, R. and Belal, M., 2017. Direct monitoring of active geohazards: emerging geophysical tools for deep-water assessments. *Near Surface Geophysics*, 15(4), pp.427-444.

Clare, M., Lintern, D., Rosenberger, K., Hughes Clarke, J., Paull, C., Gwiazda, R., Cartigny, M., Talling, P., Perara, D., Xu, J., Parsons, D., Jacinto, R. and Apprioual, R., 2020. Lessons learned from the monitoring of turbidity currents and guidance for future platform designs. *Geological Society, London, Special Publications*, 500(1), pp.605-634.

Cooper, C., Andrieux, O. and Wood, J., 2013. *Turbidity Current Measurements in the Congo Canyon*. [online] OnePetro. Available at: <https://onepetro.org/OTCONF/proceedings-abstract/13OTC/All-13OTC/OTC-23992-MS/37550> [Accessed 3 September 2021].

Cooper, C., Wood, J., Imran, J., Islam, A., Wright, P., Faria, R., Tati, A., Casey, Z. and Casey, R., 2022. Designing for Turbidity Currents in the Congo Canyon. *Offshore Technology Conference*, [online] OTC-26919-MS. Available at: <https://onepetro.org/OTCONF/proceedings-abstract/16OTC/2-16OTC/D021S027R005/85617> [Accessed 16 January 2022].

Davarpanah Jazi, S. and Wells, M., 2020. Dynamics of settling-driven convection beneath a sediment-laden buoyant overflow: Implications for the length-scale of deposition in lakes and the coastal ocean. *Sedimentology*, 67(1), pp.699-720.

De Rooij, F. and Dalziel, S., 2001. *Particulate Gravity Currents Time- and Space-Resolved Measurements of Deposition under Turbidity Currents*. Wiley.

Dorrell, R., Peakall, J., Darby, S., Parsons, D., Johnson, J., Sumner, E., Wynn, R., Özsoy, E. and Tezcan, D., 2019. Self-sharpening induces jet-like structure in seafloor gravity currents. *Nature Communications*, 10(1).

Ellison, T. and Turner, J., 1959. Turbulent entrainment in stratified flows. *Journal of Fluid Mechanics*, 6(03), p.423.

Fildani, A., 2017. Submarine Canyons: A brief review looking forward. *Geology*, 45(4), pp.383-384.

Galy, V., France-Lanord, C., Beyssac, O., Faure, P., Kudrass, H. and Palhol, F., 2007. Efficient organic carbon burial in the Bengal fan sustained by the Himalayan erosional system. *Nature*, 450(7168), pp.407-410.

García, M., 1993. Hydraulic Jumps in Sediment-Driven Bottom Currents. *Journal of Hydraulic Engineering*, 119(10), pp.1094-1117.

Garcia, M., 1994. Depositional Turbidity Currents Laden with Poorly Sorted Sediment. *Journal of Hydraulic Engineering*, 120(11), pp.1240-1263.

Garcia, M., 2008. Sedimentation engineering: processes, measurements, modelling, and practice. *American Society of Civil Engineers*.

Gartner, J., 2004. Estimating suspended solids concentrations from backscatter intensity measured by acoustic Doppler current profiler in San Francisco Bay, California. *Marine Geology*, 211(3-4), pp.169-187.

Gladstone, C. and Pritchard, D., 2010. Patterns of deposition from experimental turbidity currents with reversing buoyancy. *Sedimentology*, 57(1), pp.53-84.

Gwiazda, R., Paull, C., Kieft, B., Klimov, D., Herlien, R., Lundsten, E., McCann, M., Cartigny, M., Hamilton, A., Xu, J., Maier, K., Parsons, D. and Talling, P., 2022. Near-Bed Structure of Sediment Gravity Flows Measured by Motion-Sensing "Boulder-Like" Benthic Event Detectors (BEDs) in Monterey Canyon. *Journal of Geophysical Research: Earth Surface*, 127(2).

Ha, H., Maa, J., Park, K. and Kim, Y., 2011. Estimation of high-resolution sediment concentration profiles in bottom boundary layer using pulse-coherent acoustic Doppler current profilers. *Marine Geology*, 279(1-4), pp.199-209.

Hage, S., Cartigny, M., Sumner, E., Clare, M., Hughes Clarke, J., Talling, P., Lintern, D., Simmons, S., Silva Jacinto, R., Vellinga, A., Allin, J., Azpiroz-Zabala, M., Gales, J., Hizzett, J., Hunt, J., Mozzato, A., Parsons, D., Pope, E., Stacey, C., Symons, W., Vardy, M. and Watts, C., 2019. Direct Monitoring Reveals Initiation of Turbidity Currents From Extremely Dilute River Plumes. *Geophysical Research Letters*, 46(20), pp.11310-11320.

Hampton, M., 1972. The Role of Subaqueous Debris Flow in Generating Turbidity Currents. *SEPM Journal of Sedimentary Research*, Vol. 42.

Härtel, C., Meiburg, E. and Necker, F., 2000. Analysis and direct numerical simulation of the flow at a gravity-current head. Part 1. Flow topology and front speed for slip and no-slip boundaries. *Journal of Fluid Mechanics*, 418, pp.189-212.

Hay, A., Hatcher, M. and Hughes Clarke, J., 2021. Underwater noise from submarine turbidity currents. *JASA Express Letters*, 1(7), p.070801.

Heezen, B. and Drake, C., 1964. Grand Banks Slump: GEOLOGICAL NOTES. *AAPG Bulletin*, 48.

Heezen, B. and Ewing, W., 1952. Turbidity currents and submarine slumps, and the 1929 Grand Banks [Newfoundland] earthquake. *American Journal of Science*, 250(12), pp.849-873.

Heezen, B., Ericson, D. and Ewing, M., 1954. Further evidence for a turbidity current following the 1929 Grand banks earthquake. *Deep Sea Research (1953)*, 1(4), pp.193-202.

Hesse, R. and Khodabakhsh, S., 2006. Significance of fine-grained sediment lofting from melt-water generated turbidity currents for the timing of glaciomarine sediment transport into the deep sea. *Sedimentary Geology*, 186(1-2), pp.1-11.

Hogg, A., Huppert, H. and Hallworth, M., 1999. Reversing buoyancy of particle-driven gravity currents. *Physics of Fluids*, 11(10), pp.2891-2900.

Hughes Clarke, J., 2016. First wide-angle view of channelized turbidity currents links migrating cyclic steps to flow characteristics. *Nature Communications*, 7(1).

Hughes Clarke, J., Brucker, S., Muggah, J., Church, I., Cartwright, D., Kuus, P., Hamilton, T., Pratomo, D. and Eisen, B., 2012. *Canadian Hydrographic Conference*, Proceedings, p.15.

Hughes Clarke, J., Marques, C. and Pratomo, D., 2014. Imaging active mass-wasting and sediment flows on a fjord delta, Squamish, British Columbia. *Submarine Mass Movements and Their Consequences*, Springer Cham, pp.249-260.

Huppert, H., 1998. Quantitative modelling of granular suspension flows. *Philosophical Transactions of the Royal Society of London. Series A: Mathematical, Physical and Engineering Sciences*, 356(1747), pp.2471-2496.

Huppert, H., Turner, J. and Hallworth, M., 1995. Sedimentation and entrainment in dense layers of suspended particles stirred by an oscillating grid. *Journal of Fluid Mechanics*, 289, pp.263-293.

Huppert, H. and Simpson, J., 1980. The slumping of gravity currents. *Journal of Fluid Mechanics*, 99(4), pp.785-799.

Hürzeler, B., Ivey, G. and Imberger, J., 1995. Spreading model for a turbidity current with reversing buoyancy from a constant-volume release. *Marine and Freshwater Research*, 46(1), p.393.

Hürzeler, B., Imberger, J. and Ivey, G., 1996. Dynamics of Turbidity Current with Reversing Buoyancy. *Journal of Hydraulic Engineering*, 122(5), pp.230-236.

Inman, D., Nordstrom, C. and Flick, R., 1976. Currents in Submarine Canyons: An Air-Sea-Land Interaction. *Annual Review of Fluid Mechanics*, 8(1), pp.275-310.

Ippen, A. and Harleman, D., 1952. Steady state characteristics of sub-surface flow. *National Bureau of Standards*. 521, 79-93.

Kao, S., Dai, M., Selvaraj, K., Zhai, W., Cai, P., Chen, S., Yang, J., Liu, J., Liu, C. and Syvitski, J., 2010. Cyclone-driven deep sea injection of freshwater and heat by hyperpycnal flow in the subtropics. *Geophysical Research Letters*, 37(21), p.n/a-n/a.

Keulegan, G., 1957. *Thirteenth progress report on model laws for density currents*. [Washington]: U.S. Dept. of Commerce, National Bureau of Standards.

Keulegan, G., 1958. *Twelfth progress report on model laws for density currents*. [Washington]: U.S. Dept. of Commerce, National Bureau of Standards.

Khripounoff, A., Crassous, P., Lo Bue, N., Dennielou, B. and Silva Jacinto, R., 2012. Different types of sediment gravity flows detected in the Var submarine canyon (northwestern Mediterranean Sea). *Progress in Oceanography*, 106, pp.138-153.

Khripounoff, A., Vangriesheim, A., Babonneau, N., Crassous, P., Dennielou, B. and Savoye, B., 2003. Direct observation of intense turbidity current activity in the Zaire submarine valley at 4000 m water depth. *Marine Geology*, 194(3-4), pp.151-158.

Khripounoff, A., Vangriesheim, A., Crassous, P. and Etoubleau, J., 2009. High frequency of sediment gravity flow events in the Var submarine canyon (Mediterranean Sea). *Marine Geology*, 263(1-4), pp.1-6.

Kneller, B. and Branney, M., 1995. Sustained high-density turbidity currents and the deposition of thick massive sands. *Sedimentology*, 42(4), pp.607-616.

Kneller, B. and Buckee, C., 2000. The structure and fluid mechanics of turbidity currents: a review of some recent studies and their geological implications. *Sedimentology*, 47, pp.62-94.

Kneller, B. and McCaffrey, W., 1999. Depositional Effects of Flow Nonuniformity and Stratification Within Turbidity Currents Approaching a Bounding Slope: Deflection, Reflection, and Facies Variation. *Journal of Sedimentary Research*, Vol. 69 (1999).

Kneller, B. and McCaffrey, W., 2003. The Interpretation of Vertical Sequences in Turbidite Beds: The Influence of Longitudinal Flow Structure. *Journal of Sedimentary Research*, 73(5), pp.706-713.

Komar, P., 1969. The channelized flow of turbidity currents with application to Monterey Deep-Sea Fan Channel. *Journal of Geophysical Research*, 74(18), pp.4544-4558.

Komar, P., 1970. The Competence of Turbidity Current Flow. *Geological Society of America Bulletin*, 81(5), p.1555.

Kuenen, P. and Migliorini, C., 1950. Turbidity Currents as a Cause of Graded Bedding. *The Journal of Geology*, 58(2), pp.91-127.

Kuenen, P., 1937. Density Currents in connection with the problem of Submarine Canyons. *Geological Magazine*, 75(6), pp.241-249.

Lee, T. and Hanes, D., 1996. Comparison of field observations of the vertical distribution of suspended sand and its prediction by models. *Journal of Geophysical Research: Oceans*, 101(C2), pp.3561-3572.

Lintern, D., Hill, P. and Stacey, C., 2016. Powerful unconfined turbidity current captured by cabled observatory on the Fraser River delta slope, British Columbia, Canada. *Sedimentology*, 63(5), pp.1041-1064.

Lintern, D., Mosher, D. and Scherwath, M., 2019. Advancing from subaqueous mass movement case studies to providing advice and mitigation. *Geological Society, London, Special Publications*, 477(1), pp.1-14.

Liu, J., Hsu, R., Hung, J., Chang, Y., Wang, Y., Rendle-Bühring, R., Lee, C., Huh, C. and Yang, R., 2016. From the highest to the deepest: The Gaoping River–Gaoping Submarine Canyon dispersal system. *Earth-Science Reviews*, 153, pp.274-300.

Liu, J., Wang, Y., Yang, R., Hsu, R., Kao, S., Lin, H. and Kuo, F., 2012. Cyclone-induced hyperpycnal turbidity currents in a submarine canyon. *Journal of Geophysical Research: Oceans*, 117(C4), p.n/a-n/a.

Lowe, R., Linden, P. and Rottman, J., 2002. A laboratory study of the velocity structure in an intrusive gravity current. *Journal of Fluid Mechanics*, 456, pp.33-48.

Luchi, R., Balachandar, S., Seminara, G. and Parker, G., 2018. Turbidity Currents With Equilibrium Basal Driving Layers: A Mechanism for Long Runout. *Geophysical Research Letters*, 45(3), pp.1518-1526.

Maier, K., Gales, J., Paull, C., Rosenberger, K., Talling, P., Simmons, S., Gwiazda, R., McGann, M., Cartigny, M., Lundsten, E., Anderson, K., Clare, M., Xu, J., Parsons, D., Barry, J., Wolfson-Schwehr, M., Nieminski, N. and Sumner, E., 2019. Linking Direct Measurements of Turbidity Currents to Submarine Canyon-Floor Deposits. *Frontiers in Earth Science*, 7.

Marino, B., Thomas, L. and Linden, P., 2005. The front condition for gravity currents. *Journal of Fluid Mechanics*, 536, pp.49-78.

Martín, J., Puig, P., Palanques, A. and Ribó, M., 2014. Trawling-induced daily sediment resuspension in the flank of a Mediterranean submarine canyon. *Deep Sea Research Part II: Topical Studies in Oceanography*, 104, pp.174-183.

McClung, D. and Schaerer, P., 2006. *The avalanche handbook*. Seattle, WA: Mountaineers Books.

Meiburg, E. and Kneller, B., 2010. Turbidity Currents and Their Deposits. *Annual Review of Fluid Mechanics*, 42(1), pp.135-156.

Meiburg, E., Radhakrishnan, S. and Nasr-Azadani, M., 2015. Modeling Gravity and Turbidity Currents: Computational Approaches and Challenges. *Applied Mechanics Reviews*, 67(4).

Meneveau, C. and Katz, J., 2000. Scale-Invariance and Turbulence Models for Large-Eddy Simulation. *Annual Review of Fluid Mechanics*, 32(1), pp.1-32.

Middleton, G. and Hampton, M., 1973. *Part I. Sediment Gravity Flows: Mechanics of Flow and Deposition*. [online] Archives.datapages.com. Available at: <https://archives.datapages.com/data/pac_sepm/015/015001/pdfs/1.htm> [Accessed 22 September 2021].

Middleton, G. and Neal, W., 1989. Experiments on the Thickness of Beds Deposited by Turbidity Currents. *Journal of Sedimentary Research*, Vol. 59.

Middleton, G., 1966. EXPERIMENTS ON DENSITY AND TURBIDITY CURRENTS: I. MOTION OF THE HEAD. *Canadian Journal of Earth Sciences*, 3(4), pp.523-546.

Middleton, G., 1966. EXPERIMENTS ON DENSITY AND TURBIDITY CURRENTS: II. UNIFORM FLOW OF DENSITY CURRENTS. *Canadian Journal of Earth Sciences*, 3(5), pp.627-637.

Middleton, G., 1966. Small-Scale Models of Turbidity Currents and the Criterion for Auto-Suspension. *SEPM Journal of Sedimentary Research*, Vol. 36.

Millero, F. and Poisson, A., 1981. International one-atmosphere equation of state of seawater. Deep Sea Research Part A. Oceanographic Research Papers, 28(6), pp.625-629.

Mohrig, D. and Marr, J., 2003. Constraining the efficiency of turbidity current generation from submarine debris flows and slides using laboratory experiments. *Marine and Petroleum Geology*, 20(6-8), pp.883-899.

Mulder, T. and Alexander, J., 2001. The physical character of subaqueous sedimentary density flows and their deposits. *Sedimentology*, 48(2), pp.269-299.

Mulder, T., Syvitski, J. and Skene, K., 1998. Modeling of erosion and deposition by turbidity currents generated at river mouths. *Journal of Sedimentary Research*, 68(1), pp.124-137.

Nilsen, T., 2007. *Atlas of deep-water outcrops*. Tulsa, Okla.: American Association of Petroleum Geologists.

Ochiai, S. and Kashiwaya, K., 2010. Measurement of suspended sediment for model experiments using general-purpose optical sensors. *CATENA*, 83(1), pp.1-6.

Pantin, H., 1979. Interaction between velocity and effective density in turbidity flow: Phase-plane analysis, with criteria for autosuspension. *Marine Geology*, 31(1-2), pp.59-99.

Parker, G., 1982. Conditions for the ignition of catastrophically erosive turbidity currents. *Marine Geology*, 46(3-4), pp.307-327.

Parker, G., Fukushima, Y. and Pantin, H., 1986. Self-accelerating turbidity currents. *Journal of Fluid Mechanics*, 171(-1), p.145.

Parker, G., Garcia, M., Fukushima, Y. and Yu, W., 1987. Experiments on turbidity currents over an erodible bed. *Journal of Hydraulic Research*, 25(1), pp.123-147.

Parsons, J., Bush, J. and Syvitski, J., 2001. Hyperpycnal plume formation from riverine outflows with small sediment concentrations. *Sedimentology*, 48(2), pp.465-478.

Paull, C., Mitts, P., Ussler, W., Keaten, R. and Greene, H., 2005. Trail of sand in upper Monterey Canyon: Offshore California. *Geological Society of America Bulletin*, 117(9), p.1134.

Paull, C., Talling, P., Maier, K., Parsons, D., Xu, J., Caress, D., Gwiazda, R., Lundsten, E., Anderson, K., Barry, J., Chaffey, M., O'Reilly, T., Rosenberger, K., Gales, J., Kieft, B., McGann, M., Simmons, S., McCann, M., Sumner, E., Clare, M. and Cartigny, M., 2018. Powerful turbidity currents driven by dense basal layers. *Nature Communications*, 9(1).

Paull, C., Ussler III, W., Caress, D., Lundsten, E., Covault, J., Maier, K., Xu, J. and Augenstein, S., 2010. Origins of large crescent-shaped bedforms within the axial channel of Monterey Canyon, offshore California. *Geosphere*, 6(6), pp.755-774.

Paull, C., Ussler, W., Greene, H., Keaten, R., Mitts, P. and Barry, J., 2002. Caught in the act: the 20 December 2001 gravity flow event in Monterey Canyon. *Geo-Marine Letters*, 22(4), pp.227-232.

Petersen, F., Kopp, H., Lange, D., Hannemann, K. and Urlaub, M., 2019. Measuring tectonic seafloor deformation and strain-build up with acoustic direct-path ranging. *Journal of Geodynamics*, 124, pp.14-24.

Piomelli, U. and Balaras, E., 2002. WALL-LAYER MODELS FOR LARGE-EDDY SIMULATIONS. *Annual Review of Fluid Mechanics*, 34(1), pp.349-374.

Piper, D. and Aksu, A., 1987. The source and origin of the 1929 grand banks turbidity current inferred from sediment budgets. *Geo-Marine Letters*, 7(4), pp.177-182.

Piper, D. and Normark, W., 2009. Processes That Initiate Turbidity Currents and Their Influence on Turbidites: A Marine Geology Perspective. *Journal of Sedimentary Research*, 79(6), pp.347-362.

Piper, D., Cochonat, P. and Morrison, M., 1999. The sequence of events around the epicentre of the 1929 Grand Banks earthquake: initiation of debris flows and turbidity current inferred from sidescan sonar. *Sedimentology*, 46(1), pp.79-97.

Pirmez, C. and Imran, J., 2003. Reconstruction of turbidity currents in Amazon Channel. *Marine and Petroleum Geology*, 20(6-8), pp.823-849.

Polster, A., Fabian, M. and Villinger, H., 2009. Effective resolution and drift of Paroscientific pressure sensors derived from long-term seafloor measurements. *Geochemistry, Geophysics, Geosystems*, 10(8), p.n/a-n/a.

Pritchard, D. and Gladstone, C., 2009. Reversing buoyancy in turbidity currents: developing a hypothesis for flow transformation and for deposit facies and architecture. *Marine and Petroleum Geology*, 26(10), pp.1997-2010.

Puig, P., Canals, M., Company, J., Martín, J., Amblas, D., Lastras, G., Palanques, A. and Calafat, A., 2012. Ploughing the deep sea floor. *Nature*, 489(7415), pp.286-289.

Puig, P., Palanques, A. and Martín, J., 2014. Contemporary Sediment-Transport Processes in Submarine Canyons. *Annual Review of Marine Science*, 6(1), pp.53-77.

Quadfasel, D., Kudrass, H. and Frische, A., 1990. Deep-water renewal by turbidity currents in the Sulu Sea. *Nature*, 348(6299), pp.320-322.

Ribó, M., Puig, P. and van Haren, H., 2015. Hydrodynamics over the Gulf of Valencia continental slope and their role in sediment transport. *Deep Sea Research Part I: Oceanographic Research Papers*, 95, pp.54-66.

Ryan, W. and Heezen, B., 1965. Ionian Sea Submarine Canyons and the 1908 Messina Turbidity Current. *Geological Society of America Bulletin*, 76(8), p.915.

Schlünz, B. and Schneider, R., 2000. Transport of terrestrial organic carbon to the oceans by rivers: re-estimating flux- and burial rates. *International Journal of Earth Sciences*, 88(4), pp.599-606.

Sequeiros, O., Naruse, H., Endo, N., Garcia, M. and Parker, G., 2009. Experimental study on self-accelerating turbidity currents. *Journal of Geophysical Research*, 114(C5).

Sequeiros, O., Spinewine, B., Beaubouef, R., Sun, T., García, M. and Parker, G., 2010. Characteristics of Velocity and Excess Density Profiles of Saline Underflows and Turbidity Currents Flowing over a Mobile Bed. *Journal of Hydraulic Engineering*, 136(7), pp.412-433.

Sequeiros, O., Mosquera, R. and Pedocchi, F., 2018. Internal Structure of a Self-Accelerating Turbidity Current. *Journal of Geophysical Research: Oceans*, 123(9), pp.6260-6276.

Sequeiros, O., 2012. Estimating turbidity current conditions from channel morphology: A Froude number approach. *Journal of Geophysical Research: Oceans*, 117(C4).

Shen, C. and Lemmin, U., 1996. Ultrasonic measurements of suspended sediments: a concentration profiling system with attenuation compensation. *Measurement Science and Technology*, 7(9), pp.1191-1194.

Shepard, F. and Emery, K., 1973. Congo Submarine Canyon and Fan Valley. *AAPG Bulletin*, 57.

Shepard, F., McLoughlin, P., Marshall, N. and Sullivan, G., 1977. Current-meter recordings of low-speed turbidity currents. *Geology*, 5(5), p.297.

Shepard, F., 1954. High-velocity turbidity currents, a discussion. *Proceedings of the Royal Society of London. Series A. Mathematical and Physical Sciences*, 222(1150), pp.323-326.

Sher, D. and Woods, A., 2015. Gravity currents: entrainment, stratification and self-similarity. *Journal of Fluid Mechanics*, 784, pp.130-162.

Sher, D. and Woods, A., 2017. Mixing in continuous gravity currents. *Journal of Fluid Mechanics*, 818.

Simmons, S., Azpiroz-Zabala, M., Cartigny, M., Clare, M., Cooper, C., Parsons, D., Pope, E., Sumner, E. and Talling, P., 2020. Novel Acoustic Method Provides First Detailed Measurements of Sediment Concentration Structure Within Submarine Turbidity Currents. *Journal of Geophysical Research: Oceans*, 125(5).

Simmons, S., Parsons, D., Best, J., Oberg, K., Czuba, J. and Keevil, G., 2017. An evaluation of the use of a multibeam echo-sounder for observations of suspended sediment. *Applied Acoustics*, 126, pp.81-90.

Simpson, J. and Britter, R., 1979. The dynamics of the head of a gravity current advancing over a horizontal surface. *Journal of Fluid Mechanics*, 94(3), pp.477-495.

Simpson, J., 1982. Gravity Currents in the Laboratory, Atmosphere, and Ocean. *Annual Review of Fluid Mechanics*, 14(1), pp.213-234.

Simpson, J., 1997. *Gravity currents: in the environment and the laboratory.* 2nd ed. New York: Cambridge University Press.

Sparks, R., Moore, J. and Rice, C., 1986. The initial giant umbrella cloud of the May 18th, 1980, explosive eruption of Mount St. Helens. *Journal of Volcanology and Geothermal Research*, 28(3-4), pp.257-274.

Sparks, R., Bonnecaze, R., Huppert, H., Lister, J., Hallworth, M., Mader, H. and Phillips, J., 1993. Sediment-laden gravity currents with reversing buoyancy. *Earth and Planetary Science Letters*, 114(2-3), pp.243-257.

Sparks, R., 1997. *Volcanic plumes*. Chichester: J. Wiley Sons.

Spiess, F., 1985. Suboceanic Geodetic Measurements. *IEEE Transactions on Geoscience and Remote Sensing*, GE-23(4), pp.502-510.

Stevenson, C., Talling, P., Sumner, E., Masson, D., Frenz, M. and Wynn, R., 2014. On how thin submarine flows transported large volumes of sand for hundreds of kilometres across a flat basin plain without eroding the sea floor. *Sedimentology*, 61(7), pp.1982-2019.

Sumner, E. and Paull, C., 2014. Swept away by a turbidity current in Mendocino submarine canyon, California. *Geophysical Research Letters*, 41(21), pp.7611-7618.

Talling, P., Allin, J., Armitage, D., Arnott, R., Cartigny, M., Clare, M., Felletti, F., Covault, J., Girardclos, S., Hansen, E., Hill, P., Hiscott, R., Hogg, A., Clarke, J., Jobe, Z., Malgesini, G., Mozzato, A., Naruse, H., Parkinson, S., Peel, F., Piper, D., Pope, E., Postma, G., Rowley, P., Sguazzini, A., Stevenson, C., Sumner, E., Sylvester, Z., Watts, C. and Xu, J., 2015. Key Future Directions For

Research On Turbidity Currents and Their Deposits. *Journal of Sedimentary Research*, 85(2), pp.153-169.

Talling, P., Amy, L. and Wynn, R., 2007. New insight into the evolution of large-volume turbidity currents: comparison of turbidite shape and previous modelling results. *Sedimentology*, 54(4), pp.737-769.

Talling, P., Masson, D., Sumner, E. and Malgesini, G., 2012. Subaqueous sediment density flows: Depositional processes and deposit types. *Sedimentology*, 59(7), pp.1937-2003.

Talling, P., Paull, C. and Piper, D., 2013. How are subaqueous sediment density flows triggered, what is their internal structure and how does it evolve? Direct observations from monitoring of active flows. *Earth-Science Reviews*, 125, pp.244-287.

Talling, P., Baker, M., Pope, E., Cula, C., Cartigny, M., Faria, R., Clare, M., Simmons, S., Jacinto, R., Heijnen, M., Hage, S., Heerema, C., Ruffell, S., McGee, C., Hasenhündl, M., Apprioual, R., Gaillot, A., Wallace, D., Griffiths, A., Tshimanga, R., Bola, G., Trigg, M., Robertson, R., Urlaub, M., Parsons, D., Nambala, L. and Nunny, R., 2021. *Novel sensor array helps to understand submarine cable faults off West Africa*. [online] Eartharxiv.org. Available at: <https://eartharxiv.org/repository/view/2405/> [Accessed 15 November 2021].

Teledyne RD Instruments, 2011. *Acoustic Doppler Current Profiler Principles of Operation A Practical Primer*. [online] Teledyne RD Instruments. Available at: <https://www.comm-tec.com/Docs/Manuali/RDI/BBPRIME.pdf> [Accessed 5 January 2018].

Teledyne RD Instruments, 2018. *WORKHORSE MONITOR / SENTINEL DEPLOYMENT GUIDE*. [online] Teledyne RD Instruments. Available at: <http://www.teledynemarine.com/Documents/Brand%20Support/RD%20INSTRUMENTS/Technical%20Resources/Manuals%20and%20Guides/Workhorse/Monitor_Sentinel%20Deployment%20Guide_Jun18.pdf> [Accessed 16 December 2021].

Thorne, P. and Hanes, D., 2002. A review of acoustic measurement of small-scale sediment processes. *Continental Shelf Research*, 22(4), pp.603-632.

Thorne, P., 1985. The measurement of acoustic noise generated by moving artificial sediments. *The Journal of the Acoustical Society of America*, 78(3), pp.1013-1023.

Thorne, P., 1986. Laboratory and marine measurements on the acoustic detection of sediment transport. *The Journal of the Acoustical Society of America*, 80(3), pp.899-910.

Thorne, P., Hardcastle, P. and Soulsby, R., 1993. Analysis of acoustic measurements of suspended sediments. *Journal of Geophysical Research: Oceans*, 98(C1), pp.899-910.

Traer, M., Fildani, A., McHargue, T. and Hilley, G., 2015. Simulating depth-averaged, one-dimensional turbidity current dynamics using natural topographies. *Journal of Geophysical Research: Earth Surface*, 120(8), pp.1485-1500.

Traer, M., Hilley, G., Fildani, A. and McHargue, T., 2012. *Simulating Turbidity Current Dynamics Using Natural Topographies With and Without Clear-Water Entrainment*. [online] NASA/ADS. Available at: <https://ui.adsabs.harvard.edu/abs/2012AGUFMEP41B0778T/abstract> [Accessed 1 January 2021].

Turner, J. and Benton, E., 1974. Buoyancy Effects in Fluids. *Physics Today*, 27(3), pp.52-53.

van Weering, T. and van Iperen, J., 1984. Fine-grained sediments of the Zaire deep-sea fan, southern Atlantic Ocean. *Geological Society, London, Special Publications*, 15(1), pp.95-113.

Vangriesheim, A., Khripounoff, A. and Crassous, P., 2009. Turbidity events observed in situ along the Congo submarine channel. *Deep Sea Research Part II: Topical Studies in Oceanography*, 56(23), pp.2208-2222.

Walker, R., 1978. Deep-Water Sandstone Facies and Ancient Submarine Fans: Models for Exploration for Stratigraphic Traps. *AAPG Bulletin*, 62.

Wang, Z., Xu, J., Talling, P., Cartigny, M., Simmons, S., Gwiazda, R., Paull, C., Maier, K. and Parsons, D., 2020. Direct evidence of a high-concentration basal layer in a submarine turbidity current. *Deep Sea Research Part I: Oceanographic Research Papers*, 161, p.103300.

Weimer, P. and Link, M., 1991. *Seismic Facies and Sedimentary Processes of Submarine Fans and Turbidite Systems*. New York: Springer, pp.9-67.

Wren, D., Barkdoll, B., Kuhnle, R. and Derrow, R., 2000. Field Techniques for Suspended-Sediment Measurement. *Journal of Hydraulic Engineering*, 126(2), pp.97-104.

Xu, J., 2010. Normalized velocity profiles of field-measured turbidity currents. *Geology*, 38(6), pp.563-566.

Xu, J., 2011. Measuring currents in submarine canyons: Technological and scientific progress in the past 30 years. *Geosphere*, 7(4), pp.868-876.

Xu, J., Barry, J. and Paull, C., 2013. Small-scale turbidity currents in a big submarine canyon. *Geology*, 41(2), pp.143-146.

Xu, J., Noble, M. and Rosenfeld, L., 2004. In-situ measurements of velocity structure within turbidity currents. *Geophysical Research Letters*, 31(9), p.n/a-n/a.

Xu, J., Wong, F., Kvitek, R., Smith, D. and Paull, C., 2008. Sandwave migration in Monterey Submarine Canyon, Central California. *Marine Geology*, 248(3-4), pp.193-212.

Yeh, T., Cantero, M., Cantelli, A., Pirmez, C. and Parker, G., 2013. Turbidity current with a roof: Success and failure of RANS modeling for turbidity currents under strongly stratified conditions. *Journal of Geophysical Research: Earth Surface*, 118(3), pp.1975-1998.

Zafren, K., Brants, A., Tabner, K., Nyberg, A., Pun, M., Basnyat, B. and Brodmann Maeder, M., 2018. Wilderness Mass Casualty Incident (MCI): Rescue Chain After Avalanche at Everest Base Camp (EBC) In 2015. *Wilderness & Environmental Medicine*, 29(3), pp.401-410.

Zhang, Y., Liu, Z., Zhao, Y., Colin, C., Zhang, X., Wang, M., Zhao, S. and Kneller, B., 2018. Long-term in situ observations on typhoon-triggered turbidity currents in the deep sea. *Geology*, 46(8), pp.675-678.

Zhuang, Y., Xu, Q. and Xing, A., 2019. Numerical investigation of the air blast generated by the Wenjia valley rock avalanche in Mianzhu, Sichuan, China. *Landslides*, 16(12), pp.2499-2508.